

AD-779 949

HIGH TEMPERATURE OXIDATION OF GRAPHITE
BY A DISSOCIATED OXYGEN BEAM

George Nung-Keung Liu

Massachusetts Institute of Technology

Prepared for:

Air Force Office of Scientific Research

August 1973

DISTRIBUTED BY:

NTIS

National Technical Information Service
U. S. DEPARTMENT OF COMMERCE
5285 Port Royal Road, Springfield Va. 22151

UNCLASSIFIED

SECURITY CLASSIFICATION OF THIS PAGE (When Data Entered)

1. AD 779 949

REPORT DOCUMENTATION PAGE		READ INSTRUCTIONS BEFORE COMPLETING FORM
1. REPORT NUMBER AFOSR - TR - 74 - 0872	2. GOVT ACCESSION NO.	3. RECIPIENT'S CATALOG NUMBER
4. TITLE (and Subtitle) HIGH TEMPERATURE OXIDATION OF GRAPHITE BY A DISSOCIATED OXYGEN BEAM		5. TYPE OF REPORT & PERIOD COVERED INTERIM
		6. PERFORMING ORG. REPORT NUMBER
7. AUTHOR(s) GEORGE NUNG-KEUNG LIU		8. CONTRACT OR GRANT NUMBER(s) F44620-71-C-0009
9. PERFORMING ORGANIZATION NAME AND ADDRESS MASSACHUSETTS INSTITUTE OF TECHNOLOGY DEPT OF AERONAUTICS & ASTRONAUTICS CAMBRIDGE, MASSACHUSETTS 02139		10. PROGRAM ELEMENT, PROJECT, TASK AREA & WORK UNIT NUMBERS 681307 9781-03 61102F
11. CONTROLLING OFFICE NAME AND ADDRESS AIR FORCE OFFICE OF SCIENTIFIC RESEARCH/NA 1400 WILSON BOULEVARD ARLINGTON, VIRGINIA 22209		12. REPORT DATE AUG 1973
		13. NUMBER OF PAGES 25 221
14. MONITORING AGENCY NAME & ADDRESS (if different from Controlling Office)		15. SECURITY CLASS. (of this report) UNCLASSIFIED
		15a. DECLASSIFICATION/DOWNGRADING SCHEDULE
16. DISTRIBUTION STATEMENT (of this Report) Approved for public release; distribution unlimited.		
17. DISTRIBUTION STATEMENT (of the abstract entered in Block 20, if different from Report)		
18. SUPPLEMENTARY NOTES		
19. KEY WORDS (Continue on reverse side if necessary and identify by block number) GAS-SURFACE INTERACTION GRAPHITE OXIDATION KINETICS HETEROGENEOUS REACTION DISSOCIATED OXYGEN BEAM		
Reproduced by NATIONAL TECHNICAL INFORMATION SERVICE U. S. Department of Commerce Springfield VA 22151		
20. ABSTRACT (Continue on reverse side if necessary and identify by block number) Graphite oxidation by dissociated oxygen has been studied by molecular beam-mass spectrometry techniques. A high temperature atomic oxygen beam source (capable of generating an atom-to-molecule flux ratio of 0.5) and a modulated, pulse-counting detection scheme have been developed for the study. The target (isotropic graphite) temperature was varied from 1000° to 1700°K with a beam temperature of 300° to 2200°K and an equivalent beam pressure of about 10 ⁻⁸ to 10 ⁻⁹ atm. Measurements were carried out in the principal plane, and both beam incident and detector angles, measured from the target normal, were varied independently.		

DD 1 JAN 73 14/3 EDITION OF 1 NOV 65 IS OBSOLETE

UNCLASSIFIED

SECURITY CLASSIFICATION OF THIS PAGE (When Data Entered)

The major findings of the experiment can be summarized as follows: 1. CO is the dominant reaction product (for the stated range of pressure and temperature) for both atomic and molecular oxygen. 2. The reaction probability, ξ , of O exhibits an order of magnitude increase over that of O₂ at comparable conditions. ξ is defined as the ratio of the flux of carbon atoms (regardless of their chemical state of aggregation) away from the surface to the collision flux of O or O₂ with the surface. 3. Neither O nor O₂ reaction probabilities display simple Arrhenius behavior, and each exhibits a maximum in the target temperature range investigated. 4. While the reaction probability of O₂ shows a "hysteresis" like behavior apparently due to surface annealing effects, that of O is much less pronounced. 5. The reaction probability appears to be a function of only the target temperature and depends on neither beam temperature nor angle of incidence. 6. CO desorbs in a lobular fashion towards the target normal and the flux can be described quite well by a cosine square distribution. 7. The re-emitted O₂ comes off the target in a diffuse pattern, i.e., the flux follows a cosine distribution. Non-Arrhenius behavior of the reaction probabilities of O and O₂ can be explained qualitatively by the two-site model of Nagle and Strickland-Constable. A Rideal-type mechanism is suggested for the O-oxidation process as compared to the surface migration and dissociation-limited processes for the O₂-oxidation.

3

Massachusetts Institute of Technology
Department of Aeronautics and Astronautics
Aerophysics Laboratory

Technical Report 186

High Temperature Oxidation of Graphite
By a Dissociated Oxygen Beam

by

George Nung-Keung Liu

August 1973

Air Force Office of Scientific Research
Contract No. F44620-71-C-0009
MIT DSR No. 72803

FORWARD

This investigation was sponsored by the United States Air Force, Office of Scientific Research, under Contract No. F44620-1-C-0009. Mr. Paul A. Thurston, Mechanics Division, OSR, served as Project Monitor. The work was carried out under the direction of Professor Judson R. Baron.

TABLE OF CONTENTS

	<u>Page Number</u>
List of Symbols and Abbreviations	9
List of Figures	13
Chapter I. INTRODUCTION	15
A. General Statement of the Problem	15
B. Summary of Past Carbon and Graphite Oxidation Investigations	19
C. Molecular Beam-Mass Spectrometry Technique	38
D. Thesis Objective	41
Chapter II. SYSTEM DESIGN AND SOME PERTINENT CONSIDERATIONS	43
A. Generation of an Atomic Oxygen Beam	43
B. Detection Scheme	51
C. Signal Output and Signal-to-Noise Considerations	58
D. Data Reduction Scheme	70
E. Statistical Treatment of Experi- mental Data	76
Chapter III. EXPERIMENTAL DETAILS	81
A. Description of Apparatus	81
1. General Features	81
2. Vacuum System	82
3. Target and Its Support	88
4. Chopper and Its Collimator	90
5. Mass Spectrometer	94
6. Amplifier/Discriminator	98
7. Digital Synchronous Computer	100
8. Beam Source	103
9. Gas Inlet System	104
10. Optical Pyrometer	106
B. Beam Properties and Source Performance	107

TABLE OF CONTENTS (Continued)

	<u>Page Number</u>
C. Experimental Program and Procedure	118
1. Experimental Program	118
2. Mechanical Alignment	119
3. Typical Operating Procedure	121
4. Data Processing	123
Chapter IV. RESULTS AND DISCUSSIONS	125
A. Introduction	125
B. O ₂ Scattering from Graphite	125
C. Reaction Product and Its Angular Distribution	129
D. C-O ₂ Reaction	136
E. C-O Reaction	148
1. Reaction Probability	148
2. Hysteresis Behavior	154
3. Reaction Mechanism	157
Chapter V. CONCLUSIONS AND SUGGESTED FUTURE WORK	163
A. Conclusions	163
B. Suggested Future Work	166
Appendices	
A. Target-Detector Geometry	169
B. Pumping Speed Measurements	173
C. Ion Gauge and Mass Spectrometer Calibrations	175
References	179
Figures	189

LIST OF SYMBOLS AND ABBREVIATIONS

A	area
A_D	detector area
A_T	target surface area
B	magnetic field strength
c	velocity of light
c_j	number of carbon atoms in the jth reaction product
\bar{c}	average gas speed, $(8kT/\pi m)^{1/2}$
D	source orifice diameter
E_A	activation energy
E_{em}	ion detection efficiency of electron multiplier, detected ions/incident ion
e^-	electron
F	total particle flux; particles/sec
F_{ion}	ion flux at mass spectrometer ionizer, ions/sec
F_{ms}	pulse frequency output of the mass spectrometer, pulses/sec
f_c	chopper frequency, Hertz
G_{em}	total gain of electron multiplier
I	intensity, particles/sec-cm ²
i_e	electron emission current
i_{ms}	electron current output of the mass spectrometer
K	Clausing correction factor for channel source
Kn	Knudsen number
$K(T)$	equilibrium constant
k	Boltzmann constant

LIST OF SYMBOLS AND ABBREVIATIONS (Continued)

k_e	effective collision frequency
L	source wall thickness
l_{CD}	chopper-to-detector distance
l_{SD}	source-to-detector distance
l_{ST}	source-to-target distance
l_{TD}	target-to-detector distance
l_e	effective electron path length of the mass spectrometer ionizer
m	particle mass
\dot{m}	mass loss rate
N	number of counts
n	order of reaction; number density
n_{ion}	number density at ionizer
P_j	the probability of formation and desorption of a j th reaction product species for every incident particle
p	pressure
Q	partition function
q	electronic charge, 1.6×10^{-19} coulomb
R	gas constant; counting rate
r	radius of curvature of the particle path in the magnetic field of the mass spectrometer
S/N	signal-to-noise ratio
$(S/N)_{int}$	signal-to-noise ratio after integration
S_{ms}	mass spectrometer sensitivity, torr^{-1}
S_{ms}^i	mass spectrometer sensitivity, pulses/sec-amp-torr

LIST OF SYMBOLS AND ABBREVIATIONS (Continued)

S^*	conversion factor from number density to pulses per sec for the mass spectrometer
T	temperature, °K
t_{ms}	mass spectrometer transmission factor
V_{acc}	ion accelerating potential
V_{mp}	most probable speed of a Maxwellian gas, $(2kT/m)^{1/2}$
\dot{V}_t	test chamber pumping speed
\bar{V}	average speed of a Maxwellian beam, $(9\pi kT/8m)^{1/2}$
v	ion velocity
\dot{w}	specific surface oxidation rate, gm/cm ² -sec
X	dimensionless parameter defined by $2\pi f_c^l CD/V_{mp}$
α	degree of dissociation at equilibrium
β	pressure ratio of O and O ₂ , p_O/p_{O_2}
δ	effective hard sphere molecular diameter
ϵ	reaction probability, carbon atoms removal rate/incident particle flux
θ_D	detector angle relative to target normal
θ_d	characteristic dissociation temperature of oxygen (59,500°K)
θ_i	beam incident angle relative to target normal
λ	mean-free-path, $1/(\sqrt{2}n\pi\delta^2)$
σ	standard deviation
σ_{ion}	ionization cross-section
τ	pulse-pair resolution time
ϕ	phase lag, degrees

LIST OF SYMBOLS AND ABBREVIATIONS (Continued)

SUBSCRIPTS

a	ambient or background
B	beam
D	detector or mass spectrometer ionizer
i	incident beam
O	atomic oxygen
O ₂	molecular oxygen
S	source
T	target or surface

LIST OF FIGURES

<u>Figure Number</u>		<u>Page Number</u>
1	Degree of Dissociation of Oxygen at Thermal Equilibrium	189
2	Pressure Ratio of O to O ₂ at Thermal Equilibrium	190
3	Timing Diagram for Chopper Mode Operation of DSC	191
4	Flow Chart for Signal Processing	192
5	Amplitude Attenuation and Phase Shift for Square Modulated Maxwellian Beam (Ref. 29)	193
6	Overall View of Experimental Setup	194
7	Vacuum System	195
8	Interior View of Test Chamber	196
9	Source Housing and Target-Detector Assembly	197
10	Schematic Diagram of Test Chamber Interior Arrangement: Top View	198
11	Source Chamber	199
12	Interior View of Source Chamber	200
13	Target Holder	201
14	Tuning Fork Chopper	202
15a	Upper Trace: Reference Signal (Chopper Driver Voltage) Lower Trace: Measured Shutter Function Time Scale: 500 μ sec/cm	203
15b	Measured Shutter Function by Light-Photocell Scheme Time Scale: 200 μ sec/cm	203
16	Mass Spectrometer	204
17	Instrument Panels	205
18	Timing Diagram for the Phase Adjusting Scheme	206
19	Cross-Section Diagram of Beam Source	207
20a	Source Orifice and Radiation Shield	208
20b	Source Support Assembly	208
21	Schematic Diagram of Gas Inlet System	209

LIST OF FIGURES (Continued)

<u>Figure Number</u>		<u>Page Number</u>
22	Room Temperature Beam Centerline Signal Versus Source Pressure	210
23	Source Pressure Versus Source Temperature for Constant Leak Rate	211
24	Source Flux Angular Distribution	212
25	Incident Beam Phase Lag	213
26	Angular Distribution of Scattered Room Temperature O_2 at $\theta_i = 45^\circ$	214
27	Angular Distribution of Scattered Room Temperature O_2 at $\theta_i = 60^\circ$	215
28	Angular Distribution of Scattered High Temperature O_2	216
29	Angular Distribution of Desorbed CO for Room Temperature Incident Beam	217
30	Angular Distribution of Desorbed CO for High Temperature Incident Beam	218
31	Reaction Probability of O_2 Versus Target Temperature	219
32	Reaction Probabilities of O and O_2 Versus Target Temperature	220
33	Reaction Probabilities of O and O_2 Versus Target Temperature	221
34	Normalized CO Flux for O and O_2 Versus Target Temperature	222
35	Schematic Diagram of the Target-Detector Geometry	223

CHAPTER I

INTRODUCTIONA. General Statement of the Problem

Carbon, in its elemental or allotropic forms, plays a very important part in our everyday existence. In the form of coal, it is still one of the major energy sources in the world. Its uses range from being a moderator (in the form of graphite) in a nuclear reactor to that of printer's ink (in the form of lampblack).¹ Its study as a chemical element forms the basis of organic chemistry and its ever widespread use in industrial applications continually demands a better understanding of its properties.

One related study of considerable interest is that of graphite oxidation and erosion. Graphite's remarkable resistance to chemical attack under severe conditions has always made it an indispensable material in the electrolytic, smelting and foundry industries. In the aerospace industry, the search for highly refractory materials for aerospace and interplanetary travel applications, such as re-entry heat shields on nose cones, nozzle liners for rocket engines and thermal protection space suit clothing, has also cast graphite and its various forms as an attractive material due to its high temperature capabilities--large heat capacity in sublimation, inertness and high strength-to-mass ratio.²

In most cases, of interest is a prediction of the mass loss rate of the surface material for a given external atmosphere in order to estimate, for example, electrode wear or a heat shield requirement. A precise knowledge of gas-surface reaction kinetics would then be ideal.

Typically the atmosphere of interest is that of air, and the primary reactions involve oxygen and nitrogen. For a re-entry spacecraft, the dominant mass loss of a graphite heat shield is caused by chemical reactions with the hot shocked gas flowing around the vehicle for surface temperatures between 600°C and 2500°C and pressures in the 10^{-2} to 10^2 atmospheres range.³ Sublimation proves to be the primary mass loss mechanism for surface temperatures above 2500°C. For the chemical reaction dominated temperature range, which does cover a fairly wide range of interest, reaction with oxygen is dominant as compared with nitrogen.⁴ Furthermore, such reactions may involve dissociated oxygen generated downstream of the shock wave preceding the re-entry vehicle, even though dissociation levels in the undisturbed air are negligible below altitudes of, say, 200,000 ft. Alternatively, a vehicle may pass through atmospheric regions in which dissociation has been induced by solar radiation.⁵ Thus, a study of graphite oxidation should desirably include the combined but separable effects of atomic and molecular oxygen, i.e., in a dissociated atmosphere, in view of its prevalence in many situations.

Examination of the present available experimental data on graphite oxidation in the reaction rate controlled regime shows that the oxidation process always is assumed to follow a rate law in the Arrhenius form:⁶

$$\dot{m} = k_e (p_T)^n e^{-E_A/RT_T} \quad (1.1)$$

(Explanation of all symbols, unless otherwise noted, is given in the List of Symbols and Abbreviations Section.) Depending upon the investigator, the type of graphite studied, and the test conditions, the order of the reaction, n , has been reported in the range zero to unity; the activation energy, E_A , falls within the limits 9 to 60 Kcal/mole; and the effective collision frequency, k_e , varies over several orders of magnitude.

Several explanations can be offered for the huge scatter in the experimental data. One concerns the validity of the Arrhenius rate law itself. The rate expression is a carryover from homogeneous reactions and some questions can be raised about its applicability to heterogeneous reactions. Though the exponential component of the equation may be justified by concepts from kinetic theory as applied to two reacting gases⁶ (treating the surface as an array of atoms, for example), no distinction is then made between gas and surface temperatures, which often is not the case. Constant activation energy was usually assumed for macroscopic

applications in the temperature range of interest⁷ but, in fact, experimental values do show a dependence on temperature. For example, both Blyholder and Eyring⁸ and Horton,⁹ in their respective experiments, show that logarithmic plots of \dot{m} versus $1/T_r$ (so-called Arrhenius plots) are nonlinear, implying a "varying" activation energy. Furthermore, the reaction order was observed to be temperature dependent. Rosner and Allendorf,¹⁰ in their experiments on graphite oxidation, have also shown that oxidation probability (a measure of \dot{m}) in an Arrhenius plot is non-linear. The effective collision frequency, k_e , is essentially an empirical steric factor and, of course, does not offer insight into the interaction details.

A second major reason for extensive scatter of collected data is related to the experimental techniques. A survey of the literature on graphite oxidation rate studies, a brief summary of which is presented in Section I-B, reveals that a majority of the experiments were carried out in the continuum regime (small Knudsen number based on the mean-free-path of the reacting gas and a characteristic dimension of the macroscopic surface) in which diffusion effects may be important. Multiple gas-surface collisions as well as gas-gas collisions are then common, the implication being that the species detected were not necessarily the primary products of the surface reaction but rather a near equilibrium or possibly equilibrium distribution of

the products. Very reactive free radical intermediates of the reaction were always masked and never detected. Since the primary goal of all kinetic studies is the delineation of a reaction mechanism consistent with kinetic data, a somewhat more accurate and controllable experimental technique is in order. It was the purpose of the present work to devise such an experiment so as to permit study of the graphite oxidation process in a dissociated atmosphere.

B. Summary of Past Carbon and Graphite Oxidation Investigations

The continuous interest in carbon and graphite oxidation over many decades had generated a voluminous amount of literature on the subject. A literature survey reveals that almost every common form of carbon has been the subject of oxidation studies. Such work naturally included both scientifically oriented studies in which the reaction mechanisms were of primary interest and engineering design type studies in which measurements of erosion of devices fabricated from particular forms of carbon were aimed at. Only the former, more fundamental, work will be reviewed here and even so, an exhaustive review will not be attempted. Instead, what follows will be a presentation of representative work and of major contributions. Readers interested in more discussions are referred to articles by Blackwood¹¹ and Walker et al¹² for work done prior to 1959 and by Thomas¹³ for more recent investigations.

The crystallography of graphite is referred to any standard handbook, such as Ref. 1.

Smith,¹⁴ in 1863, was probably the first to suggest that when oxygen is adsorbed on a carbon surface it undergoes a chemical change. He found that adsorption of oxygen on charcoal did not cease even after a month; and that while nitrogen and other gases adsorbed on charcoal could be easily removed as such, oxygen could be removed only on strong heating, and then only as carbon dioxide. Rhead and Wheeler¹⁵ concluded that oxygen combines with a mass of carbon directly to form a physicochemical complex, C_xO_y , of variable composition, which decomposes over a wide range of temperature, giving a mixture of carbon monoxide CO and carbon dioxide CO_2 . These observations were confirmed by Lowry and Hulett,¹⁶ who, while attempting to determine the content of the moisture and gas in charcoal, noticed that the gases evolved up to $900^\circ C$ consisted almost entirely of CO_2 and CO, the former predominating at lower temperatures and the latter at higher temperatures.

Further evidence for chemisorption or fixation of oxygen on carbons were furnished by the work of Langmuir¹⁷ and others.^{18,19} Langmuir, in his work on the interaction of oxygen with carbon filaments, noticed that the gas was held so firmly on the carbon surface that it came off when heated only as oxides of carbon. He also found that the adsorption rate of oxygen on the carbon filament was quite

irreproducible and depended on the previous history of the filament. Nevertheless, he proposed that on the surface of the filament one adsorbable atom or molecule of the gas would be bound for each carbon atom. Combination at the surface then produced CO and CO₂, which were desorbed when heated. Shah,²⁰ using charcoal as a source of carbon, proposed the chemisorption of oxygen on the surface and suggested that the mechanism was similar to that put forward by Langmuir.

By then, it was quite well established that when carbon was exposed to oxygen three products could form: gaseous carbon monoxide, gaseous carbon dioxide, and a carbon-oxygen surface complex. Also, the amount of gaseous products formed relative to the amount of surface complex formed was shown to depend strongly upon temperature. Though the exact nature or composition of the surface complex was not known, the concept as such was an important step in understanding the reaction mechanisms.

Studying the oxidation of thin layers of activated charcoal, Chukhanov and Karzhavina²¹ concluded that oxidation of the carbon could take place at a temperature as low as 300°C and that it proceeded through the formation of a surface oxide, C₃O₄, which formed very rapidly and then decomposed in the presence of carbon and oxygen, giving CO and CO₂ in equal amounts. At temperatures above 1100°C the reaction favored the formation of CO. Increasing the

velocity of the gases flowing over the carbon suppressed the formation of CO_2 . The fact that the ratio of CO to CO_2 was not constant and could be varied by a change in the conditions was confirmed by Tsukhanova.²²

Realizing that the oxidation of a carbon surface had been shown to be a complicated process and the possibility that primary steps could be masked by secondary processes in previous experiments, Meyer²³ studied the oxidation of graphite in the form of electrically heated elements at low pressures. He found that the pressure in the reaction cell had to be low enough for gas molecules leaving the hot surface to reach the cold walls of the cell without collision with other molecules and the subsequent formation of secondary reaction products. He also found that the gas velocity through the apparatus had to be great enough to prevent the reaction products returning to the filament and that the graphite surface had to be smooth to avoid such occurrences. CO and CO_2 were observed in equal proportions independent of temperature and pressure at temperatures below 1200°C . The rate of reaction, however, was proportional to the oxygen pressure. The reaction was explained by supposing that the oxygen penetrated deeply into the graphite lattice by solution and at the same time passed into a reactive state and disintegrated the lattice, preferentially at the basal planes. As the temperature was raised above 1200°C , the reaction rapidly slowed down and

the CO_2/CO ratio fell to approximately 0.5 at about 1500°C , the reaction then being of the zeroth order. This change was attributed to the diminution of the solubility of the oxygen in the carbon until ultimately the surface oxidation mechanism became solely responsible for the reaction rate.

The suggestion by Mayers²⁴ that the rate of oxidation of carbon under many conditions was determined not by the speed of chemical reaction but by the rate at which oxygen could diffuse onto the surface helped to explain discrepancies in several observed rates. Kuchta et al,²⁵ using high velocity air streams passing over spectroscopic-grade carbon between 900°C and 1200°C , were able to demonstrate the change of the reaction rate from diffusion-limited to chemically-controlled as the air velocity was varied. The reaction of carbon and oxygen was diffusion-limited at low air velocities, but at high air velocities the rate of reaction approached that predicted on the basis of the Arrhenius equation.

Strickland-Constable's earlier work²⁶ in 1944 showed substantial agreement with recent results obtained in the study of graphite oxidation. Using filaments of fully out-gassed graphite resistively heated to 900 - 2000°C and burned in an oxygen background of 20 - 500 millitorr, he found that CO was the principal reaction product. There was always a trace of CO_2 but the CO/CO_2 ratio was invariably greater than 7 and varied inversely with temperature. He could not

determine an origin for the CO_2 as the small amounts could have resulted from secondary oxidation of CO. The reaction was observed to obey first order pressure dependence with a maximum rate occurring at about 1200°C . The rate of the reaction was also found to exhibit a hysteresis behavior, the extent of which depended on the past temperature history of the filament. On proceeding from a lower to a higher temperature a new rate lower than the steady state value was obtained. Conversely, on reducing temperature, the initial rate was found to be higher than the steady state rate. Such hysteresis was explained by the existence of an inhibiting surface layer which was removable at high temperatures. Similar results were obtained by Duval,²⁷ again using a hot filament technique, but a reverse hysteresis was noted. This reverse hysteresis from that of Strickland-Constable was confirmed by recent results of Olander et al²⁸ and Shih²⁹ using completely different experimental techniques. Strickland-Constable, in addition, noticed that the amount of oxygen adsorbed was somewhat less than previously suggested.

A study by van Loon and Smeets³⁰ of burning carbon particles in a vortex chamber had tended to confirm the view that CO was the primary product but the controversy was by no means over. Meyer³¹ showed that the results of Strickland-Constable should not be taken without reservation

mainly because that the latter was unable to prevent multiple collisions with the hot filament due to the lack of a flow technique. In contrast to Strickland-Constable, he found the carbon-oxygen reaction to be of first order from 700-1200°C while from 1500-2200°C a zeroth order was observed. No maximum in the reaction rate was observed. Instead, the two regions of first and zeroth order pressure dependence were characterized by constant activation energies of 25 and 90 kcal/mole respectively. The CO/CO₂ ratio was nearly unity and was independent of temperature and pressure. He attributed the zeroth order dependence at high temperatures to evaporation of reaction product as being the rate limiting step.

Oxidation of pyrolytic graphite was studied by Horton⁹ in a flowing system at atmospheric pressure. By measuring dimensional changes, the reaction rates were obtained for the basal and edge planes. Neither gas velocity nor diffusion greatly affected the observed rates, which were of one-half order with an activation energy of 37 kcal/mole at temperatures between 600-1550°C. A mechanism consisting of rapid adsorption of oxygen with rate limiting desorption of CO or CO₂ was suggested. Also, the reaction rate of spectroscopic graphite was found to be two orders of magnitude faster than that of the basal plane of pyrolytic graphite.

Many attempts^{32,33} had been made to study the kinetics of the reaction by determining the order of the reaction and the energy of activation. The reaction appeared to be of the first order up to temperatures of approximately 1300°C, but above this was zeroth order. Energies of activation varied between 14 and 36 kcal/mole. The difficulties involved in preventing secondary reactions and the dependence of the reaction order on the surface coverage by the carbon-oxygen complex, which in turn was a function of the absolute pressure level, called for some reservation in accepting the results of those investigations. The study of the reaction order, however, did provide a means for estimating the percentage of surface area covered by stable surface complex.

Loebenstein and Deitz,³⁴ in their study of the chemisorption of oxygen on amorphous carbon at 270°K, indicated that less than 6% of the total carbon surface proved active for adsorption. Bonnetain, Duval and Letort,³⁵ by subjecting carbon to oxidation and successive degassing at temperatures between 450 and 700°C, found that the relative production rates of CO and CO₂ depended on pressure levels as well as temperatures. They concluded that the simplest model accounting for these effects would be based on a surface complex state and estimated that the surface complexes covered about 5% of the total surface area at a pressure level of 10^{-4} torr.

Laine et al,³⁶ monitoring the course of the oxygen-graphitized carbon (Spheron 6) reaction mass spectrometrically, determined that CO was the principal product of the surface complex. Their outgassing experiments also yielded the total active surface area which at 300°C was about 2.3% of the total area. Due to the change in the available area with coverage, the reaction was found to deviate from first order. The surface complex was found to be stable at the reaction temperature but decomposed and desorbed as the surface temperature was increased with nearly all of it desorbed by 950°C.

Strickland-Constable et al^{37,28} studied the oxidation rate of pyrolytic graphite between 1000-2400°C by means of a directed oxygen jet at a heated carbon bar and measured the rates from photographed erosion profiles. They were able to correlate their results empirically with modifications of the theory proposed earlier by Blyholder, Binford and Eyring.³⁹ The modified theory assumes that surface reaction sites can be classified into two groups: a more reactive A-site and a less reactive B-site. At low temperature the oxidation rate is dominated by the more reactive A-sites, which represent a fraction of the surface. At higher temperatures the A-sites rearrange thermally to form less reactive B-sites. A-sites are also created when B-sites are oxidized and desorb CO. It is the competition between the generation of active A-sites by oxidation of

B-sites and their deactivation by thermal annealing that resulted in the observed maximum in the reaction rate with varying graphite temperatures. At still higher temperatures the oxidation rate increases with an increase in the B-site reactivity. Though the explicit nature of the two different sites was not stated, it was encouraging to see that experimental results over a wide range of pressures and temperatures fitted quite well to this two-site model.

In order to determine the nature of the active sites on which surface complexes could form, topographical studies by means of optical and electron microscopy have been made for the carbon-oxygen reaction. Perhaps best known in this area is the work of Hennig.^{40,41,42} Using naturally occurring graphite single crystals as well characterized specimens, he found that the edge planes oxidized at least twenty times faster than the basal planes. The etch pits on the basal planes were hexagonal in shape bounded by vertical $(11\bar{2}0, 1\bar{2}10, 2\bar{1}\bar{1}0)$ faces, suggesting that the more active sites were lattice defect points, such as vacancies and dislocations, and grain boundaries. Thomas et al.^{43,44,45} drew similar conclusions using optical microscopy. In addition, Thomas⁴⁵ found that atomic oxygen, generated by microwave discharge of oxygen, formed uniformly spaced pits over the entire basal plane surface with no preferred sites. No quantitative measure of the reaction rate was made, however.

The suggestion of different types of adsorption sites led to the adsorption experiments by Hart, Vastola and Walker.⁵⁰ They found two levels of adsorption in the temperature range from 25-400°C. Dissociative immobile adsorption was assumed and suggestions were made that different types of adsorption sites might be associated with the various carbon-carbon distances in graphite.

Lussow et al.⁵¹ studied the chemisorption of oxygen on graphon in the temperature range from 300-680°C. Oxygen chemisorption was found to increase rapidly above 400°C, indicating two types of active sites. A suggestion was made that an oxygen molecule first formed a mobile adsorption complex which later dissociated to form two mobile atomic surface complexes, seemingly in contrast to the assumption of Hart et al.⁵⁰ The conclusion, however, was that different type of active sites, dominating in various temperature ranges, might have different fundamental behaviors.

Bansal et al.,⁵² using preoxidized graphon, studied the desorption rate of surface oxides from 500-1000°C. Graphs of cumulative CO desorption vs. temperature revealed several distinctive slopes of the curve, implying that CO desorbed from different types of sites. Also, oxides formed at higher temperatures were found to be less stable than those formed at lower temperatures.

Walker et al.⁵³ investigated the effects of previously adsorbed surface complexes on later adsorption patterns and subsequent desorption products. Their approach made use of heavy oxygen (O_2^{18-18}) as a tracer. A graphon sample at 280°C was first exposed to ordinary oxygen and then subsequent adsorption was made using O_2^{18-18} . Upon desorbing the surface complex formed, the fraction of O^{18} in each product was found to be invariant with desorption temperature, indicating that the time of formation of surface complexes had little effect on the reaction process.

The thermal annealing or deactivation of active sites as proposed in the two-site model of Strickland-Constable et al may be attributed to the reduction of crystal imperfections by heat treatment. Bowman,⁵⁴ in his study of the imperfections in graphite structure using X-ray diffraction, noticed that most strains in the crystal structure were eliminated by heating in the temperature range of 2000-3000°C. Nightingale and Snyder,⁵⁵ in addition to X-ray diffraction technique, monitored the dimensional changes of the bulk graphite after exposing it to neutron radiation, which resulted in lattice defects such as vacancies and interstices. It was found that higher temperatures or longer time of annealing had a parallel effect in the rate of restoring the bulk graphite to its original, preradiation dimension and structure. Similar

conclusions were drawn by Price and Bokros⁵⁶ for neutron irradiated pyrocarbons, primarily based on measurements of physical properties such as density, resistivity and microhardness. Specifically, restoration took place after one hour at about 1400°C with a rapid increase in recovery rate at over 2000°C.

Oxidation on carbon surface was known to cause lattice imperfections which tend to accelerate the reaction rate. In fact, this process was responsible for the generation of A-sites from B-sites as proposed in the two-site model of Strickland-Constable et al. Antonowicz⁵⁷ discovered electron spin centers on carbon surface after oxidation. This was attributed to the removal of carbon atoms leaving neighboring atoms with unpaired spins. As expected, the spin centers were eliminated upon thermal annealing.

The effects of impurities in the carbon on the reactivity with oxygen had also been investigated. Harker⁴⁶ noticed an increase in reactivity of coconut charcoal and oxygen with the presence of alkali metals but attributed the result to the attack of the surface by free metal. Amariglio and Duval⁴⁷ found that metal oxides of high vapor pressures were generally catalysts in accelerating the graphite oxidation reaction and proposed that the metal oxide furnished a "reactive" oxygen to the graphite. Roscoe⁴⁸ studied the catalytic effects of boron and molybdenum on oxidation of natural graphite crystals and

concluded that the catalyst acted on existing active sites.

To prevent the impurities, which existed in most forms of carbon, from masking the true kinetics, Evans and Phaal⁴⁹ employed diamond as a clean, well-defined, non-porous surface in studying the carbon-oxygen reaction. Unfortunately, at temperatures over 850°C a stable, black carbon film formed on the surface, drastically changing the surface characteristics and destroying the original idea of a well-characterized surface.

Recently, a totally different approach from previous experimental techniques has been made in studying graphite oxidation. Olander et al,²⁸ using modulated molecular beam-mass spectrometry, investigated the reaction kinetics of oxidation of pyrolytic graphite in both the basal and prism planes. Suggestion of reaction mechanisms was based on comparison of model calculations and experimental results of a reaction product vector. The experiment covered an effective oxygen beam pressure range at the target between 5×10^{-6} and 2×10^{-4} torr together with a surface temperature range of 1000 to 1800°K. CO was found to be the dominant reactant product and a first order dependence of pressure was observed for surface temperatures above 1200°K. The reaction probability exhibited a maximum around 1450°K and a hysteresis behavior similar to that observed by Duval²⁷ was confirmed. A two-branch, two-site mechanism, similar to the model used by Strickland-

Constable,^{37,38} was proposed for the basal plane reaction in which the molecular oxygen first dissociated on the surface forming one bound CO and one mobile adsorbed O atom. The adsorbed atomic oxygen was said to then migrate about the surface until it reacted with a suitable carbon atom and subsequently both bound CO were desorbed. Oxidation of the prism plane was found to be affected by the diffusion of the surface species into the bulk graphite. While the work represented an elegant, self-contained theory and experiment, the interpretation of data depended heavily on the modelling phase. Nevertheless, it signifies an important step in unraveling the carbon-oxygen reaction.

Shih²⁹ carried out a similar molecular beam experiment in which the re-emitted particles from the target surface were modulated instead of the incident beam. The phase shift measurements were avoided but so were their subjective interpretations. General agreement of results existed between Shih and Olander et al and in particular, Shih showed that, depending on the temperature range, several minutes to many hours were required to reach steady state reaction rates with regard to surface annealing and site generation. While the empirical parameters chosen by Nagle and Strickland-Constable³⁷ in their two-site model appeared to correlate quite well for results of incident O₂ pressure greater than 10⁻⁵ atm.,⁵⁸ the same parameters, extended to the lower pressure range of Shih (order of

10^{-8} atm.), seemed to predict a lower reaction probability than was measured. It was suggested that the discrepancy arose due to the relative insensitivity of the chosen parameters to the detailed dynamics on the surface at high pressures (above 10^{-5} atm.) as implied by the short adjustment times while this was not true for the case of low pressures (10^{-8} atm. or lower) where a somewhat more accurate description of the surface processes was necessary. CO was also observed to desorb in a lobular fashion towards the surface normal and the flux could be described quite well by a cosine square distribution.

While numerous investigations have been carried out for graphite oxidation by molecular oxygen, investigations of the effects of atomic oxygen on the rate of oxidation have been relatively rare, primarily due to the difficulty in generating atomic oxygen.

In 1959 Streznewski and Turkevich⁵⁹ studied the reaction of carbon with oxygen atoms. Evaporated carbon films and carbon particles obtained by burning benzene in air were reacted with atomic oxygen produced by D.C. discharge at 5000 volts. Optical transparency of the carbon films was monitored for the rate of erosion and O concentration was determined by the rise of temperature of a platinum filament introduced in the gas stream. The oxidation rate of the carbon black samples was inferred by noting the change in size using electron microscopy. The

rate of erosion of carbon was found to be independent of the specimen temperature in the range from 20 to 100°C and to depend directly on O concentration.

Vastola et al⁶⁰ reacted spectroscopically pure graphite rods at room temperature with O from a microwave discharge and analyzed the products of reaction mass spectrometrically. CO was found to be the major product. However, no quantitative results were attempted at all.

Rosner and Allendorf^{3,10} have made comparative studies of the attack of pyrolytic and isotropic graphite by atomic and molecular oxygen. Atomic oxygen was generated by a microwave discharge in a gas flow system and the ablation rate of the electrically heated graphite filament was monitored optically. Typical oxygen pressure level was 10^{-2} torr and the target temperature varied from 1100 to 2000°K. Their principal findings were: (1) O was an order of magnitude more reactive than O₂ for both pyrolytic and isotropic graphite at equivalent surface temperatures; (2) the oxidation rates of pyrolytic and isotropic graphite by O were comparable while pyrolytic graphite was more oxidation-resistant than isotropic graphite in O₂; (3) all oxidation probabilities exhibited a maximum in the temperature range covered; (4) the surface temperature dependence of the oxidation probabilities by O were much less pronounced than that by O₂. These results implied that O and O₂ oxidation may very well proceed along different mechanisms. The

surface structure of graphite, which proved to be important for the O_2 oxidation rate, had a minor effect on the O oxidation rate. It was suggested that while the O_2 oxidation rate was limited by dissociative, activated adsorption of oxygen molecules on the surface, the O oxidation followed a Rideal-type mechanism in which the impact of a gaseous O upon an adsorbed O led to the formation and desorption of CO_2 .

Marsh et al,^{61,62,63} in a series of investigations, had made careful studies on the surface conditions of graphite after exposing it to a stream of atomic oxygen. Again microwave discharge was used to generate O and its concentration measured by calorimetric method using a catalytic probe of freshly prepared silver-coated platinum wire which limited the maximum gas temperature to be measured at about $100^\circ C$. The total weight loss of the specimen was measured by a vacuum microbalance and the surface structure was examined by an electron microscope. For a surface temperature range of 0 to $400^\circ C$, it was found that, unlike molecular oxygen which attacked preferred regions of the cleavage surface such as defect points, atomic oxygen produced etch pits over almost the entire basal surface. The pits were conically shaped, smaller in size but greater in number than the well-defined, though somewhat shallow, hexagonal pits produced by molecular oxygen. Additionally, the atomic oxygen tended to display preferential attack of the

basal planes along twin bands. A zero or very small activation energy was observed for the C-O reaction and the formation of surface oxide complexes was established as both CO and CO₂ were desorbed when the target was heated up to high temperatures subsequent to oxidation. Judging from the shape of the etch pits observed after oxidation, it was concluded that O and O₂ oxidation must involve different mechanisms and the O oxidation rate should be relatively insensitive to the forms of graphite. These conclusions indirectly substantiated the results obtained by Rosner and Allendorf though the two groups worked in distinctively different surface temperature regimes.

Recently, McCarroll and McKee⁶⁴ studied qualitatively the effects of dissociated oxygen on natural graphite crystals at temperatures below 1000°C. Topographical changes of the surface were monitored by electron microscopy after the specimen was exposed to a stream of dissociated oxygen from microwave discharge. Specifically, it was found that for surface temperatures below 700°C, no reaction took place for O₂ whereas O produced unoriented pits over the whole basal surface. It was concluded that O₂ oxidation took place at sites of lattice defect points such as vacancies, non-basal screw and edge dislocations. No such sites were necessary for initiation of O oxidation.

A common criticism for all O oxidation studies is that there is in general no precise knowledge of the composition and state of the gas generated. Electrode contamination,

carrier gas in discharge cavity, ionization and electronic excitation of oxygen may all have significant effects on the surface phenomena. Perhaps, this is why very few quantitative investigations have been attempted. There is no doubt that a better way of generating oxygen atoms would aid the study of the C-O reaction in a more definitive way.

C. Molecular Beam-Mass Spectrometry Technique

Molecular beam techniques have been used in different areas of research for a number of years. Much of our present knowledge of interatomic and intermolecular interactions comes from atomic and molecular beam scattering studies. Measurements of the elastic differential cross section now yield very accurate potential curves for systems characterized by a single potential; Pauly's work on alkali-rare gas systems is a notable example.⁶⁵ For non-reactive gas-solid scattering studies, sophisticated techniques such as time-of-flight measurements were used to characterize accurately the state of the gas before and after surface scattering. Moran's work⁶⁶ involving argon on platinum is an example of results that can be used to assess the assumptions made in a scattering theory such as that of Logan and Stickney.⁶⁷ In chemical research, molecular beam techniques have been used for a number of years, particularly in the study of gas phase reactions, surface ionization and chemical resonance effects. However, heterogeneous chemical kinetic studies have been made possible only within the past decade by the development of several

important experimental tools: high sensitivity, compact mass spectrometers; clean, high speed vacuum pumps; and phase-sensitive detectors or lock-in amplifiers. Recently, Merrill⁶⁸ reviewed the applications of molecular beam techniques to catalysis and reaction studies and predicted considerable sophistication in future experimental systems.

Typically, a molecular beam-mass spectrometry system consists of two vacuum chambers separated by an orifice or slit. A beam generating source is housed in one chamber while the target and detector assembly is located in the other. The reactant gas from the source interacts with the surface as a collimated beam of particles in parallel flight and the products of reaction are monitored by the mass spectrometer. The pressure level in the reaction chamber is such that there is virtual absence of gas-gas collisions (typically $p \leq 10^{-7}$ torr).

A major advantage of this method in studying heterogeneous reaction is that very reactive intermediates of the reaction can be analyzed as readily as stable products. Detection in high vacuum insures that the observed species represent primary products of reaction rather than those resulting from wall or gas phase collisions prior to analysis. Important experimental parameters, such as intensity of the molecular beam (the pressure of the gaseous reactant), temperatures of the beam and target surface, incident beam and detector angles with respect to the surface, and composition of the beam are all reasonably

controllable. Again, due to low pressure levels, gas diffusion limited reactions are eliminated and the test surface is less prone to contamination.

The molecular beam-mass spectrometry technique has, however, one great disadvantage: the reaction product signal is usually small and buried in a relatively large noise background, thereby limiting the resulting signal-to-noise S/N ratio. Thus, any study of chemical reactions using a molecular beam is predicated upon the attainment of a satisfactory S/N ratio. This problem can be overcome in part by use of a "lock-in" detection technique. By modulating or mechanically chopping the signal flux and applying some form of phase-sensitive (lock-in) detection, the weak signal may be extracted from the noise. An analysis of this lock-in amplification technique as applied to molecular beams scattered from solid surfaces was given by Yamamoto and Stickney.⁶⁹

Successful work using this technique in this same laboratory was first done by Shih,²⁹ who studied graphite oxidation by molecular oxygen. Among efforts by other groups was the study of dissociation of hydrogen on tantalum by Krakowski and Olander.⁷⁰ Smith and Fite⁷¹ and McKinley⁷² investigated the nickel-chlorine reaction. Germanium oxidation was studied by Anderson and Bondart⁷³ and the dissociation of nitrous oxide on tungsten by Coltharp et al.⁷⁴ Recently, an investigation pertinent to the present work was completed by Olander et al.,²⁸ who made a comparative

study of the oxidation mechanisms of the basal and prism planes of pyrolytic graphite.

In view of the success of the molecular beam-mass spectrometry technique in studying heterogeneous chemical reactions, it was decided that the present investigation of graphite oxidation by dissociated oxygen was feasible.

D. Thesis Objective

The object of the thesis is to study experimentally the reaction mechanisms of dissociated oxygen on graphite by means of molecular beam-mass spectrometry technique. Separate effects of atomic and molecular oxygen on the oxidation rate were to be determined and isotropic graphite was to be used as the target material. In order to achieve the thesis objective with some insight into the dependence of the reaction on relevant parameters, the following experimental quantities as functions of beam and target temperatures, equivalent beam pressure and incident angle were to be measured:

1. The reaction probabilities of atomic and molecular oxygen.
2. The products of reaction and their relative amounts.
3. The spatial flux distribution of the products and reactants of reaction emitted from the target.
4. Hysteresis behavior patterns.

A major portion of the study involved the design and development of a vacuum system, a high temperature O and O₂ source, together with a sensitive and stable detection scheme. To minimize design complications, all experimental variables were restricted to the principal plane only, i.e., the plane defined by the beam axis and the normal to the target.

CHAPTER II

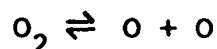
SYSTEM DESIGN AND SOME PERTINENT CONSIDERATIONSA. Generation of an Atomic Oxygen Beam

The most common way of generating atomic oxygen previously was by means of an electrodeless discharge. This includes both radio frequency ($\sim 10^6$ Hz) and microwave ($\sim 10^9$ Hz) discharges. Apart from the usually expensive and elaborate equipment necessary for such a system, there are several drawbacks. One highly undesirable feature is that ionization and electronic excitation of the gas invariably take place along with dissociation. This may have a significant effect on the reaction process. Due to the nature of the discharge, it is impossible to control the temperature of the gas to cover a broad range (e.g., from room temperature to target surface temperature). It has been shown by Rose and Brown⁷⁵ that for a microwave discharge the optimal breakdown pressure for oxygen is about 4 torr, in which case recombination of atoms downstream of the discharge cavity is significant and essentially reduces the atom-to-molecule ratio at the reaction surface. To increase dissociation, various carrier gases such as water vapor, nitrogen, helium and argon have been added to discharge cavities. Such a trial-and-error technique for a particular system depends mainly on the ingenuity of the experimentalist. Though varying degree of success has been

achieved (e.g., 17% dissociation achieved by Lam⁷⁶ using double discharge cavities with the addition of water vapor), the introduction of foreign gases in the reaction contributes another factor of doubt. The same problems plague other O generation techniques such as high voltage DC discharge and chemical reaction (e.g., titration of N with NO).

Direct equilibrium thermal dissociation of oxygen appears to be an attractive procedure, since the present design need incorporates both the heating of O₂ as well as the generation of O. The composition and state of the gas is then known quite accurately and the risk of contaminants is minimal. An investigation into such a scheme revealed, however, some associated problems.

For a symmetrical diatomic gas like oxygen, the dissociation-recombination reaction can be represented by



The degree of dissociation, α , can be defined by

$$\alpha = \frac{N_{\text{O}}}{N^{\text{O}}} = \frac{m_{\text{O}} N_{\text{O}}}{m_{\text{O}} N^{\text{O}}} = \frac{\text{Mass of dissociated O-atoms}}{\text{Total mass of gas}}$$

where N_{O} = number of dissociated O-atoms

N^{O} = total number of O-atoms present in the mixture

and m_{O} = mass of an O-atom.

From the law of mass action, α at equilibrium is given by⁷⁷

$$\frac{\alpha^2}{1-\alpha} = \frac{\{Q_O\}^2}{2N^O Q_{O_2}} \exp(-\theta_d/T) \quad (2.1)$$

Eq. (2.1) can be rewritten in terms of the equilibrium constant, $K(T)$, as

$$\frac{\alpha^2}{1-\alpha} = \frac{K(T)}{4p}$$

or

$$\alpha = \sqrt{\frac{K(T)}{K(T)+4p}} \quad (2.2)$$

where p = total pressure of the gas mixture.

From a tabulation of $K(T)$,⁷⁸ we can obtain the degree of dissociation as functions of temperatures and pressures. Figure 1 shows such a set of curves. For our purposes the O-to-O₂ pressure ratio, β , defined by

$$\beta \equiv \frac{p_O}{p_{O_2}} = \frac{n_O}{n_{O_2}} = \frac{2\alpha}{1-\alpha} \quad (2.3)$$

provides a similar but more useful set of curves shown in Fig. 2. Clearly, there is practically no dissociation of oxygen at temperatures below 2000°K and the degree of dissociation is a strong function of pressure at a given temperature. For example, at a source temperature of

2200°K - presumably a reasonable operating temperature for a source fabricated from a refractory material in an oxygen atmosphere - β is equal to 11% at 1 torr whereas when p is decreased to 0.1 torr, β is about 30%. Though the absolute flux of O-atoms may be higher for 1 torr than a corresponding lower total pressure, the increase in O-to-O₂ flux ratio is more attractive despite the lower pressure level, since a primary concern is separating out of the effects of O and O₂ for the oxidation reaction. In principle, the problem of a mixture of O and O₂ can be eliminated by operating a source at a very low pressure, e.g., pure atomic oxygen can be obtained at a source pressure of about 10^{-7} torr and a temperature of 2300°K. In practice, however, this would mean a beam of extremely low intensity and provide an insurmountable detection problem, at least, by present day techniques. The related problem of minimum detectable signals will be considered in later sections. At present, suffice to say, for a maximum source operating temperature of 2300°K the source pressure should be less than 1 torr for appreciable dissociation of oxygen.

For such low source pressure levels, the use of a Knudsen or effusive source immediately suggests itself. Though generally of lower intensity and characteristically having a wider distribution of velocities than a nozzle or Kantrowitz-Grey source, the effusive source does have some

advantages for present purposes. Recombination of atoms during the free jet expansion process associated with a nozzle source is thereby eliminated, since there is a virtual absence of gas-gas collisions for an effusive source expansion. The properties of an effusive beam, such as velocity distribution, intensity and composition can be predicted easily by applying elementary kinetic theory once the source pressure and temperature are known. In contrast, for a nozzle beam, the precise "freezing" behavior is not known, especially for the ill-defined nozzles customarily employed in beam systems. Additionally, a skimmer or collimator of the nozzle beam generally has a disturbing effect on the flow field. Thus, in order to characterize the state of such a beam, an experimental measurement such as the time-of-flight technique for velocity distribution is almost unavoidable. Although the total gas flow in a nozzle beam system is orders of magnitude greater than that for typical effusive beam apparatus, most of the gas has to be removed upstream of the skimmer. As it turns out, such dumping of oxygen into the source chamber further results in an intolerable background oxygen pressure that leads to rapid oxidation of any heating element. This could be averted only after major modifications of the experimental setup. The reader is referred to an article by Anderson et al⁷⁹ for detailed discussions of the difference in properties and operation of effusive and nozzle beams.

One of the criteria of a Knudsen source is that the Knudsen number, λ/D , where λ is the mean-free-path of the gas and D is a characteristic dimension (e.g., the diameter) of the orifice, is of an order greater than unity. Necessarily, the orifice dimension also should be small compared to the size of the plenum chamber. Physically, the particles then will wander through the orifice without any collision during the transit and without disturbing the state of the gas in the source. Under these circumstances, for a circular orifice of negligible wall thickness, the flux density or intensity of particles at a distance, ℓ , from the orifice along a ray forming an angle, θ , with the axis normal to the orifice area is

$$\begin{aligned}
 I_s &= \left(\frac{n_s \bar{c}_s}{4} \right) \left(\frac{\pi D^2}{4} \right) \frac{\cos \theta}{\pi \ell^2} \\
 &= \frac{P_s}{\sqrt{2 \pi n_s k T_s}} \left(\frac{\pi D^2}{4} \right) \frac{\cos \theta}{\pi \ell^2} \quad (2.4)
 \end{aligned}$$

As an estimate for the appropriate orifice size, consider the case for maximum intensity, i.e., $Kn \approx 1$. This implies

$$D = \lambda = \frac{1}{\sqrt{2n} \pi \delta^2} = \frac{kT}{\sqrt{2p} \pi \delta^2} \quad (2.5)$$

For O_2 , $\delta \approx 3.0 \times 10^{-8}$ cm and at a sample source operating condition of 2200°K and 1 torr, $D = 0.058$ cm. This results in an O-to- O_2 intensity ratio,

$$\frac{I_{\text{O}}}{I_{\text{O}_2}} = 0.11,$$

or about one O-atom for every nine O₂-molecules in the beam, a ratio which would be too small for separating the individual effects of O and O₂. A one-to-three ratio of O-to-O₂ flux at a source temperature of 2200°K requires a source pressure of 0.2 torr. This means, however, a five-fold reduction in the total beam intensity. An enlargement of the source diameter may appear to solve this particular problem, but it was found during the course of the experiment that the most troublesome feature of a thermal dissociation O-atom source proved to be the rapid oxidation rate of the heating element (and not the signal level). Since the total flux from the source is proportional to the square of the source diameter, the bulk of which must be evacuated by the source chamber pump, such an approach to enhancement of signal intensity results in a drastic shortening of filament life. Of course, it is impossible to predict an optimal operating condition a priori since the optimization process involves many unknown quantities, only two of which are the oxidation rate of the heating element and the minimum detectable signal. It was only during the course of the experiment that an ultimate operating condition was arrived at that satisfied all of the practical requirements.

In practice, the orifice wall is of finite thickness. Equation (2.4) for the beam intensity still holds for the beam axis (i.e., the $\theta = 0$ direction), provided that either the wall thickness, L , is less than the orifice diameter, or the Knudsen number, λ/L , is greater than unity. However, the total flux out of the orifice is reduced; the correction factor was worked out by Clausing⁸⁰ in terms of the dimensionless variable L/D .

The presence of oxygen at high temperature severely limits the choice of source and heater materials. Ceramics appear to be the only choice for a source chamber material and thorium oxide (thoria) was selected mainly for its inertness and high melting temperature (3300°K). Nevertheless, it does have drawbacks in connection with poor thermal conductivity and poor thermal shock resistance. Extreme care must be exercised in heating and cooling the thoria to prevent cracking, and no significant load can be applied on the material as it tends to soften at temperatures above 2300°K . Unfortunately, no extensive quantitative data is available for the material, even from the manufacturer, and knowledge about the physical properties must be acquired from experience for a particular application. Tungsten was chosen as the heater material, again for its high melting temperature (3655°K) and its relative inertness in an oxygen atmosphere. However, its non-negligible oxidation rate at high temperatures and its reductive reaction when in contact

with thoria do pose the problem of a finite heater life. The final design of the source and its performance will be described in Chapter III.

It should be noted that various methods to increase beam intensity, such as multiparallel channel or slit sources, were considered and rejected because of difficulty in fabrication and/or an implied intolerable rise in source chamber pressure level.

B. Detection Scheme

The principal disadvantage of molecular beam ⁶⁹ lies of heterogeneous chemical reactions is that related to working with a small signal embedded in a relatively high noise background. Basically, this stems from the fact that usually only a small portion of the signal flux is sampled directly by the detector. The signal-to-noise ratio generally depends on the mass of the product measured, the quality of the background pressure attainable, the incident beam intensity and, in this instance, the reaction probability. By modulating the signal flux and applying some form of phase-lock detection, the weak signal may be extracted from the noise.⁶⁹ In recent years, sophisticated commercial analog lock-in amplifiers have become available and are almost indispensable in modulated molecular beam techniques. The analog lock-in amplifier, however, is not without limitations and is not necessarily adequate for this (Knudsen) experiment in view of the huge decrease in

incident beam intensity (an approximate two orders of magnitude drop from that of a typical nozzle beam).

Theoretically, any desired S/N ratio could be obtained from a lock-in amplifier output provided that the integration time is long enough; in practice, only a finite integration time is possible even for the most sophisticated analog lock-in amplifiers, mainly for reasons of capacitor leakage in the RC type integrator circuits used as well as circuit drift and instability. An integration time constant of 100 sec. for the Princeton Applied Research Model HR-8 lock-in amplifier is typical. In addition, the absolute results obtained in an analog detection scheme may not be too reliable, since the current or voltage type output is often not repeatable due to fluctuations in both electron multiplier and amplifier gain. Frequent calibrations are necessary but may prove too cumbersome in certain experimental setups. In view of these shortcomings, a pulse counting type detection scheme was investigated.

For extremely weak signals (low in count rates), digital or pulse counting techniques are ideal in principle. By counting each individual ion from a mass spectrometer as a discrete pulse, one essentially eliminates the uncertainty factor in the various gains of the amplifiers. In other words, each ion is given equal weight in computing the signal level independent of such electron multiplier and amplifier

gain variations. By setting a suitable threshold level in a discriminator (i.e., using a pulse height discrimination method), certain noise levels (e.g., white noises in electron multiplier and amplifiers) can be filtered out, which is not possible with an analog scheme. White noise in an analog detection system can be reduced only by integration. The use of memory cells for signal storage in a pulse counting scheme also means indefinite integration time, limited only by the capacity of the memory units. However, the pulse counting technique has not been fully exploited in molecular beam studies mainly because the existing signal processing rate has been inadequate. The highest count rates to be handled with negligible counter deadtime are about 10^5 counts/sec, and signal loss due to pulse-pair resolution under such conditions is significant for most scattering experiments. It is due to the recent availability of a high speed, digital lock-in amplifier (SSR Instrument Co. Model 1110 Digital Synchronous Computer, DSC) together with a compatible amplifier/discriminator, A/D (SSR Instrument Co. Model 1120) that pulse counting becomes extremely attractive for the present application. Important features of the DSC are: maximum count rate of 85 MHz; pulse-pair resolution of 12 nsec; dual channels for integration; and channel capacity of 10^8 counts. The A/D, in addition to its role as a noise filter, also generates standard size pulses, as required by the DSC,

according to the input pulse rate. Due to the extremely wide band and high sensitivity of the A/D, transients from switches, running motors, signals from TV and radio broadcasts, and so forth can all be anticipated to be unavoidable pickups by the amplifier and thus introduce spurious counts. Meticulous care is, therefore, necessary to provide good radio frequency shielding and grounding practice.

Whenever a small signal in the presence of a large background (as in the present case to be shown in Section II-C) has to be retrieved, signal modulation technique can be applied. In this case, the DSC is operated in the so-called "chopper" mode. Trigger signals from the modulator or chopper serve to initiate two counting periods per chopper cycle: one when the chopper is open, the other when the chopper is closed, as shown in the timing diagram, Fig. 3. The corresponding signal and noise pulses are directed into two high speed counters, "A" and "B", by means of digital gates. Pulses gated to counter "A" consist of both the modulated signal and DC background noise pulses whereas pulses gated to counter "B" consist only of background noise pulses. This process continues until a preset number of chopper cycles has been achieved. When the accumulated pulses in "A" and "B" are subtracted, the resulting difference is that portion of the signal originally modulated by the chopper. This number, when

divided by the number of chopper cycles and the counter sampling time, is the signal count rate. The counter sampling time during each of the two phases of the operation is generally set to give a maximum duty cycle, whereas the selection of the total number of counting cycles depends mainly on the natural signal-to-noise ratio and the accuracy of the measurement required. At the completion of a number of preset chopper cycles, the DSC can be set to either repeat the "same" measurement or hold the data. For the repetitive operation, the set of data is available until the end of the next counting period.

To estimate the total counting time required to achieve a given accuracy of measurement, an analysis will be given assuming the errors introduced by the processes of totaling the counts and measuring the elapsed time are negligible compared with the statistical error. This assumption is true for most counting equipment. Furthermore, all fluctuations of both the signal and noise level are assumed to follow the Poisson distribution (i.e., all events are random and uncorrelated). The standard deviation, σ , will be used for the precision index in the following discussion.

If N is the number of counts summed over a time interval, t , the counting rate R is

$$R = \frac{N}{t} \quad (2.6)$$

This value with its standard deviation may be stated as⁸¹

$$R \pm \sigma_R = \frac{N}{t} \pm \frac{N^{1/2}}{t} = R \pm \left(\frac{R}{t}\right)^{1/2} \quad (2.7)$$

The error is then

$$\frac{\sigma_R}{R} = \frac{1}{(R t)^{1/2}} = \frac{1}{N^{1/2}} \quad (2.8)$$

Eq. (2.8) is a formal statement of the very important conclusion that the percentage error of a counting measurement is determined entirely by the total number of counts accumulated.

When several quantities having standard deviations $\sigma_1, \sigma_2, \dots, \sigma_n$ are combined by either addition or subtraction, the standard deviation of the result is

$$\sigma = (\sigma_1^2 + \sigma_2^2 + \dots + \sigma_n^2)^{1/2} \quad (2.9)$$

For the present case of a background or noise counting rate of $R_N \pm \sigma_N$ and a total counting rate, due to both signal and the background, of $R_T \pm \sigma_T$, the counting rate, R_S , due to the signal only is

$$R_S \pm \sigma_S = (R_T - R_N) \pm (\sigma_T^2 + \sigma_N^2)^{1/2} \quad (2.10)$$

The error for the signal counting rate is then

$$\begin{aligned}
 \frac{\sigma_S}{R_S} &= \frac{(\sigma_T^2 + \sigma_N^2)^{1/2}}{R} \\
 &= \frac{(\frac{R_N}{t_N} + \frac{R_T}{t_T})^{1/2}}{R_S}
 \end{aligned}
 \tag{2.11}$$

Since the sampling times in channels "A" and "B" are the same, Eq. (2.11) becomes

$$\begin{aligned}
 \frac{\sigma_S}{R_S} &= \frac{(\frac{R_N}{t} + \frac{R_T}{t})^{1/2}}{R_S} \\
 &= \frac{(2R_N + R_S)^{1/2}}{R_S t^{1/2}}
 \end{aligned}
 \tag{2.12}$$

Eq. (2.12) is essentially the reciprocal of the signal-to-noise ratio after integration, namely,

$$\left(\frac{S}{N}\right)_{\text{int}} = \frac{R_S t^{1/2}}{(2R_N + R_S)^{1/2}}
 \tag{2.13}$$

R_S/R_N is the signal-to-noise ratio of the system before the integration scheme and its estimation is given in Section II-C. With typical values of

$$R_S = 10 \text{ cps} \quad \text{and} \quad R_S/R_N = 1/5000$$

an integration time of 10^5 sec. (approximately 3 hours) is required for a maximum error of 10% in the measured signal.

The total number of counts accumulated in this case is 5×10^9 , which will have exceeded the existing counter capacity. To alleviate this problem, the integration scheme may simply be carried out in a series of shorter integration periods within which the total pulse count is less than the saturation limit of the counters. This burden of recording many sets of data has the advantage, however, of providing a means to eliminate some of the spurious counts without jeopardizing the whole measurement as will be discussed in Section II-E.

The pulse-pair resolution limit of the counting equipment is a measurement of the counter dead time. A first order correction for the dead time is given by⁸¹

$$R = R_o / (1 - R_o \tau) \quad (2.14)$$

where R is the true count rate

R_o is the observed count rate

and τ is the pulse-pair resolution time.

For a value of τ of 10^{-8} sec, the correction is approximately 0.1% at a count rate of 10^5 pulses per second, which can be safely neglected.

C. Signal Output and Signal-to-Noise Considerations

A flow chart for the signal processing scheme is shown in Fig. 4. The signal flux from the target or the incident beam was first modulated by the tuning fork chopper before its mass spectrum was analyzed by the mass spectrometer.

The signal, in the form of molecules or atoms, is converted into ions in the mass spectrometer ionizer. The resulting ion number flux is given by

$$F_{\text{ion}} = \frac{n_{\text{ion}} \sigma_{\text{ion}} l_e i_e}{q} \quad (2.15)$$

since the mass spectrometer ionizer is a density sensitive detector. In Eq. (2.15), it is assumed that the particles are singly ionized and that the signal flux is constant across the length of the ionizer so that the local, instantaneous number density in the ionizer is uniform.

Only a portion of the ions produced in the ionizer will pass through the spectrometer and arrive at the first dynode surface of the electron multiplier, their fraction depending upon the ion drawout efficiency of the mass spectrometer and the mass number to which the mass spectrometer is tuned. This fraction, essentially the mass spectrometer transmission factor, t_{ms} , depends on the design of the mass spectrometer and is generally quite small. For a double-slit, magnetic deflection type mass spectrometer, a value of 10^{-4} is typical.³²

The total gain, G_{em} , of an electron multiplier used as an ion detector is given by

$$G_{em} = g_1 g_2^a \quad (2.16)$$

where g_1 is the first dynode conversion efficiency in electrons/ion

g_2 is the secondary emission coefficient of the remaining dynodes

and a is the number of remaining dynode stages.

g_1 and g_2 will, of course, vary with incident ion energy, dynode surface material and electron multiplier voltage.

The electron current output of the mass spectrometer, i_{ms} , is then given by

$$\begin{aligned} i_{ms} &= q F_{ion} t_{ms} G_{em} \\ &= n_{ion} \sigma_{ion} l_e i_e t_{ms} g_1 g_2^a \quad (2.17) \end{aligned}$$

The performance of the mass spectrometer, usually expressed in terms of a sensitivity, S_{ms} , can now be evaluated. The mass spectrometer sensitivity, in torr^{-1} , is given by

$$S_{ms} = \frac{i_{ms}}{i_e p} = \frac{\sigma_{ion} l_e t_{ms} g_1 g_2^a}{kT_a} \quad (2.18)$$

where $p = n_{ion} kT_a$ and $T_a = 300^\circ\text{K}$

In a pulse counting scheme, the absolute value of the electron multiplier gain is unimportant as compared to the overall ion detection efficiency, E_{em} , in detected ions/incident ion. Thus, the pulse frequency output of the mass

spectrometer, F_{ms} , can be written as

$$F_{ms} = F_{ion} t_{ms} E_{em} = \frac{n_{ion} \sigma_{ion} l_e i_e t_{ms} E_{ms}}{q} \quad (2.19)$$

For incident ion energies between 2.5 and 5 KeV, the efficiency remains substantially constant at a value of about unity. As before, we can define another mass spectrometer sensitivity, S_{ms}^i , in terms of the pulse frequency output:

$$S_{ms}^i = \frac{F_{ms}}{i_e p} = \frac{\sigma_{ion} l_e t_{ms} E_{em}}{q k T_a} \quad (2.20)$$

The units for S_{ms}^i are pulses/sec-amp-torr.

From Eqs. (2.18) and (2.20),

$$S_{ms}^i = S_{ms} \left(\frac{E_{em}}{q G_{em}} \right) \quad (2.21)$$

This result can be used to estimate the sensitivity of the present pulse counting scheme from results obtained in the analog system used by Shih.²⁹ Choosing typical values as follows,

$$S_{ms} = 300 \text{ (torr)}^{-1}$$

$$E_{em} = 1$$

$$G_{em} = 10^6$$

results in,

$$S_{ms}^i = 1.87 \times 10^{15} \frac{\text{pulses}}{\text{sec-amp-torr}} \quad (2.22)$$

A convenient expression for estimating the signal output pulse frequency will be one that relates the number of ion output pulses to the number density at the ionizer as given by Eq. (2.19). In terms of S_{ms}^i , this can be written as

$$F_{ms} = n_{ion} S_{ms}^i k_a^T i_e \equiv n_{ion} S^* \quad (2.23)$$

S^* is simply a modified mass spectrometer sensitivity that converts the number density at the ionizer directly to output pulse frequency. Its magnitude, like that of S_{ms}^i , depends on the detected gas species. However, for the gases of interest in this experiment, the variation in magnitude of S^* will be less than 25 per cent.²⁹ At an electron emission current of 1 ma and a mass spectrometer sensitivity as given in Eq. (2.22), a number density of 1 part/cm³ at the ionizer will give rise to 5.8×10^{-2} pulses/sec at the output of the electron multiplier.

An estimation of the signal-to-noise ratio will now proceed.

The incident beam intensity at the target surface, assuming that the target is in the beam axis and that it subtends a small solid angle as viewed from the source

orifice, is given by Eq. (2.4):

$$I_T = \left(\frac{n_s \bar{c}_s}{4} \right) \left(\frac{\pi D^2}{4} \right) \left(\frac{1}{\pi l_{ST}^2} \right) \quad (2.24)$$

The total particle flux on the target, F_T , is

$$F_T = I_T A_T \cos \theta_i \quad (2.25)$$

where θ_i is the beam incident angle on the target relative to the surface normal. Assuming all products of reactions are diffusively emitted from the target, and that the target can be treated as a point source as viewed by the detector, then the total reaction product flux of the j th species entering the detector, i.e., the mass spectrometer ionizer, is

$$(F_j)_D = F_T \frac{P_j \cos \theta_D A_D}{\pi l_{TD}^2} \quad (2.26)$$

where P_j is the probability of the formation and desorption of a j th reaction product species for every incident particle. (A consideration of the correction of the particle flux due to the actual target-detector geometry is given in Appendix A.) P_j is related to the reaction probability, ϵ , defined as the ratio of the carbon atom removal rate to the incident particle flux by,

$$\begin{aligned}\epsilon &\equiv \frac{\text{Carbon atom removal rate}}{\text{Incident particle flux}} \\ &= \frac{\sum_j c_j P_j F_T}{F_T} = \sum_j c_j P_j\end{aligned}\quad (2.27)$$

where c_j is the number of carbon atoms in the j th reaction product.

Now, the total j th reaction product flux entering into the ionizer can be written as

$$(F_j)_D = (n_j)_D \bar{v}_j A_D \quad (2.28)$$

where \bar{v}_j is the average velocity of the j th reaction product. If the products of reaction are in thermal equilibrium with the target surface and they desorb from the surface with a Maxwellian velocity distribution, then

$$\bar{v}_j = \sqrt{\frac{9\pi k T_T}{8m_j}} \quad (2.29)$$

and therefore,

$$(n_j)_D = (F_j)_D \cdot \sqrt{\frac{8m_j}{9\pi k T_T}} \cdot \frac{1}{A_D} \quad (2.30)$$

Eq. (2.30) represents the signal level of the j th reaction product that would be detected by the mass spectrometer. An actual pulse frequency output from the electron multiplier can be obtained from Eq. (2.23).

In a molecular beam experiment, the signal is usually buried in a high background noise level. For a pulse counting scheme, the noise that needs to be considered is that corresponding to ambient gases in the test chamber which have the same mass number as the signal being detected. Electronic noises, such as electron multiplier dark current and input resistor shot noise, can all be eliminated by using the previously mentioned pulse height discrimination technique. The ambient gases are due to two sources primarily. One is the residual gas mixture in the vacuum system, the amount of which depends on the system design and the pumping speed. For an oil diffusion pumped and liquid nitrogen cooled vacuum system, the most common background gases are hydrogen, helium, water vapor, carbon monoxide and nitrogen. The other source for ambient gases is that of products of reaction from the target surface.

The total reaction product flux of the j th species leaving the target surface is

$$F_j = F_T P_j \quad (2.31)$$

This will result in an ambient partial pressure of the j th gas component in the test chamber,

$$(p_j)_T = \frac{F_T P_j}{\dot{V}_t} \quad (2.32)$$

where \dot{V}_t is the test chamber pumping speed. If we denote the partial pressure of the j th gas component due to the residual gases as $(p_j)_R$, then the total ambient partial pressure of the j th gas component is

$$(p_j)_a = (p_j)_T + (p_j)_R = \frac{F_T P_j}{\dot{V}_t} + (p_j)_R \quad (2.33)$$

In terms of number density, equivalently

$$(n_j)_a = \frac{1}{kT_a} \left[\frac{F_T P_j}{\dot{V}_t} + (p_j)_R \right] \quad (2.34)$$

where T_a is usually equal to the room temperature. The signal-to-noise, S/N , ratio for the j th reaction product is then,

$$\left(\frac{S}{N}\right)_j = \frac{(n_j)_D}{(n_j)_a} \quad (2.35)$$

where $(n_j)_D$ and $(n_j)_a$ are given by Eqs. (2.30) and (2.34) respectively.

For an estimation of the magnitude of the S/N ratio, the following realistic parameters may be used:

$$\begin{aligned}
p_s &= 1 \text{ torr}, & T_s &= 2200^\circ\text{K} \\
D &= 0.025 \text{ cm}, & \ell_{ST} &= 9 \text{ cm} \\
A_T &= 1 \text{ cm}^2, & A_D &= 1 \text{ cm}^2 \\
\theta_i, \theta_D &= 45^\circ, & \ell_{TD} &= 18 \text{ cm} \\
T_T &= 1300^\circ\text{K}, & T_a &= 300^\circ\text{K} \\
p_j &= 10^{-2}, & (p_j)_R &= 10^{-9} \text{ torr} \\
\dot{V}_t &= 2000 \text{ litres/sec}
\end{aligned}$$

Assuming CO is the reaction product, the resulting S/N ratio is

$$\left(\frac{S}{N}\right)_{\text{CO}} = \frac{1.21 \times 10^4}{3.22 \times 10^7} \approx \frac{1}{2700} \quad (2.36)$$

This is a very small S/N ratio indeed, and without any S/N enhancement scheme the signal would be impossible to detect. For CO_2 detection, the S/N ratio is much improved since there is usually little or no residual CO_2 gas present, and thus the noise is contributed entirely by the reaction product flux from the target surface. In this case, assuming $(p_{\text{CO}_2})_R$ to be zero and using similar parameters, the resulting S/N ratio is

$$\left(\frac{S}{N}\right)_{\text{CO}_2} = \frac{1.21 \times 10^4}{9.50 \times 10^5} \approx \frac{1}{80} \quad (2.37)$$

It is worthwhile to point out the advantage of having a huge pumping speed, as illustrated by Eq. (2.34), using the above parameters for CO detection:

$$(n_j)_a = \frac{1}{kT_a} \left[\frac{F_T P_j}{\dot{V}_t} + (P_j)_R \right]$$

or

$$(n_{CO})_a = \frac{1}{kT_a} (2.95 \times 10^{-11} + 10^{-9}) = \frac{10^{-9}}{kT_a} (0.0295 + 1) \quad (2.38)$$

We can see that the ambient noise is contributed almost entirely by the residual gases with only about 3% being due to the reaction product flux in this case. The advantage of a high pumping speed is even more dramatically demonstrated for the case of CO_2 detection, as shown by the relatively high S/N ratio.

In estimating the signal output level, it was assumed that the particle beam is well collimated so that all particles effusing from the source orifice, except for the portion directed at the target surface, are pumped away in the source chamber. This, in fact, was the case for most of the present experimental runs. It was found, however, that for source temperatures above 2200°K, an efficient way of prolonging the heater life was to move the source orifice close to the source collimator so that essentially all particles actually are effused into the source chamber. The drawback of this solution to the heater

life problem is that the resulting increase in oxygen pressure in the test chamber may contribute a significant portion to the detected signal.

The total flux out of an effusive channel source is

$$F_s = K \left(\frac{n_s \bar{c}_s}{4} \right) \left(\frac{\pi D^2}{4} \right) \quad (2.39)$$

where K is the Clausing factor.⁸⁰ The resulting increase in ambient pressure in the test chamber is

$$(p_s)_a = \frac{F_s}{\dot{V}_t} \quad (2.40)$$

and the incident particle flux on the target due to this pressure is given by

$$(F_T)_a = \frac{(p_s)_a}{\sqrt{2\pi mkT_a}} \cdot A_T \quad (2.41)$$

A ratio of this incident flux and the flux directly from the source orifice onto the target (Eq. (2.25)) furnishes an estimate of the correction that is necessary to arrive at the reaction probability. This ratio, after simplification, is

$$\frac{(F_T)_a}{F_T} = \frac{K \pi l_{ST}^2}{\dot{V}_t \sqrt{2\pi mkT_a} \cos \theta_i} \quad (2.42)$$

With the same parameters previously used for estimating the S/N ratio and the additional parameter of $L = 0.080$ cm, Eq. (2.42) results in

$$\frac{(F_T)_a}{F_T} = 0.15 \quad (2.43)$$

a correction which is not negligible.

D. Data Reduction Scheme

The reaction probability, as defined by Eq. (2.27), is obtained experimentally by measuring the incident beam flux and the reaction product angular flux distribution from the target surface in the principal plane, i.e., the plane defined by the beam axis and the normal to the target. The reaction product angular flux distribution is then assumed to be axisymmetric with respect to the surface normal. This assumption appears to be reasonable in view of the actual measured angular flux distribution, which shows that the reaction product desorbs in a lobular fashion towards the surface normal.

The incident beam flux is measured by positioning the mass spectrometer ionizer directly on the beam axis. In this case, the beam intensity at the detector is

$$(I_D)_i = \left(\frac{n_s \bar{c}_s}{4}\right) \left(\frac{\pi D^2}{4}\right) \left(\frac{1}{2}\right)_{\text{SD}} \quad (2.44)$$

Thus, the beam intensity at the target is obtained by

$$I_T = (I_D)_i \left(\frac{\ell_{SD}}{\ell_{ST}} \right)^2 \quad (2.45)$$

For a Maxwellian beam, the average beam velocity is

$$\bar{v}_B = \sqrt{\frac{9 \pi k T_S}{8 m_S}} \quad (2.46)$$

Therefore, the number density at the detector for the incident beam is

$$n_i = (I_D)_i \sqrt{\frac{8 m_S}{9 \pi k T_S}} \quad (2.47)$$

The pulse frequency output from the mass spectrometer for the incident beam is then

$$(F_{ms})_i = n_i S_i^* \quad (2.48)$$

where S_i^* denotes the mass spectrometer conversion factor for the incident gas. From Eq. (2.25), the total particle flux on the target, F_T , in terms of the detected pulse frequency of the incident beam is

$$F_T = (F_{ms})_i \frac{A_T \cos \theta_i}{S_i^*} \sqrt{\frac{9 \pi k T_S}{8 m_S}} \left(\frac{\ell_{SD}}{\ell_{ST}} \right)^2 \quad (2.49)$$

Consider the case when the products of reaction are diffusively desorbed from the target surface and let the

intensity of the j th species measured at the normal direction (i.e., $\theta_D = 0$) be $(I_{10})_j$, then the total flux of the j th reaction product desorbed from the surface, $(F_1)_j$, is

$$\begin{aligned} (F_1)_j &= \int_{\Omega} (I_{10})_j \cos \theta \, d\omega = \int_{\phi=0}^{2\pi} \int_{\theta=0}^{\pi/2} (I_{10})_j \cos \theta \sin \theta \, d\theta d\phi \\ &= \pi (I_{10})_j \end{aligned} \quad (2.50)$$

If $(F_{ms})_j$ denotes the measured pulse frequency output from the mass spectrometer for the j th reaction product at $\theta_D = 0$, then using Eqs. (2.30) and (2.50), $(F_1)_j$ is given by

$$(F_1)_j = \frac{\pi l_{TD}^2}{S_j^*} \sqrt{\frac{9 \pi k T_T}{8 m_j}} (F_{ms})_j \quad (2.51)$$

Therefore, the reaction probability is

$$\begin{aligned} \epsilon &= \frac{\sum_j c_j (F_1)_j}{F_T} \\ &= \frac{\pi}{A_T \cos \theta_i} \left(\frac{l_{TD} l_{ST}}{l_{SD}} \right)^2 \sqrt{\frac{T_T}{T_S}} \sum_j c_j \frac{S_i^* \sqrt{m_S}}{S_j^* \sqrt{m_j}} \frac{(F_{ms})_j}{(F_{ms})_i} \end{aligned} \quad (2.52)$$

Eq. (2.52) is a relatively simple expression for the reaction probability. The principal assumption is that the products of reaction desorb in a diffuse pattern, i.e., the flux distribution follows the cosine law. If the

reaction products desorb in a lobular manner in the normal direction and the flux distribution can be described empirically by $\cos^n \theta$, then the total flux of the j th reaction product desorbed from the surface, $(F_n)_j$, is

$$\begin{aligned}
 (F_n)_j &= \int_{\Omega} (I_{n0})_j \cos^n \theta \, d\omega \\
 &= \int_{\phi=0}^{2\pi} \int_{\theta=0}^{\pi/2} (I_{n0})_j \cos^n \theta \sin \theta \, d\theta \, d\phi \\
 &= \frac{2\pi}{n+1} (I_{n0})_j
 \end{aligned} \tag{2.53}$$

where $(I_{n0})_j$ is the measured intensity of j th species at the normal direction.

The reaction probability, in this case, is simply obtained by multiplying Eq. (2.52) by the factor $2/(n+1)$.

For a dissociated incident beam, the reaction probabilities of O and O₂ have been determined by applying the method of superposition. In principle, this is only applicable for linear surface processes. Although non-linear surface processes are quite common (e.g., bimolecular recombination), the method is justified in this experiment in view of the extremely low incident flux on the surface and the observed first order pressure dependence of the O₂ oxidation rate. The reaction probability of O₂ at the dissociated beam temperature was obtained by extrapolation from results of lower beam temperatures, at which the beam consists, essentially, of pure O₂.

Up to this point, the analysis has not considered the molecular transit effects. Due to the finite molecular velocities, there will be a time lag between the time when the molecules first pass the chopper and when they are detected at the mass spectrometer ionizer. This time lag is usually expressed as a phase lag in terms of the chopper frequency. Previously, it was assumed that the molecules travel with an average velocity of the molecular beam, making it quite straight forward in determining the phase lag for detection process. Moreover, the wave shape of the chopped beam will be exactly similar to the chopper opening shape. However, since the beam contains the whole Maxwellian velocity spectrum, the chopped wave shape will be distorted at the detector, depending on the beam temperature and flight path. In other words, the chopped wave shape will vary as the faster molecules move ahead and the slower molecules fall behind from the average speed molecules. In general, this results in a decrease in the wave amplitude and the effect is known as dispersion attenuation.

The dispersion attenuation and phase shift for Maxwellian molecular beams have been computed and tabulated for different beam properties by Harrison, Hummer and Fite.^{83,84} The magnitude of these corrections depends on the chopper frequency, f_c , the chopper-to-detector distance, l_{CD} , and the gas temperature, T , as reflected in the most probable

speed, $v_{mp} = (2kT/m)^{1/2}$. The amplitude dispersion attenuation and phase shift are tabulated as functions of the dimensionless parameter, X , defined by

$$X = \frac{2 \pi f_c l_{CD}}{v_{mp}} \quad (2.54)$$

For $f_c = 377$ Hz, $l_{CD} = 6$ cm, and a molecular oxygen beam of $300^\circ K$, $X = 0.363$ giving an amplitude dispersion attenuation of 4% and a phase lag of 22° , as compared to a 16° lag from the simple-minded calculation of using the average beam speed, \bar{v} , in

$$\phi = \frac{360 f_c l_{CD}}{\bar{v}}, \quad (2.55)$$

ϕ being the phase lag in degrees.

For gas at higher temperatures, the amplitude attenuation is even less and the difference between the phase lag from the exact analysis and Eq. (2.55) will become almost negligible. Curves of the amplitude attenuation and phase lag for range of X of interest in this experiment are available in Ref. 29 and they are reproduced in Fig. 5. It can be seen that for minimal corrections, short flight paths are applicable for a given chopper frequency. However, long flight paths are desirable when the transit dispersion effects are measured for determining the speed spectrum of a molecular beam.⁸⁵

E. Statistical Treatment of Experimental Data

In this section the rather controversial question of data rejection will be considered. It concerns the problem of what to do if, among a set of observations, one or more have deviations so large as to seem unreasonable. Such an observation creates an awkward situation for the experimenter. If one retains the questionable observation, it can have quite a large effect on the mean. If, on the other hand, it is discarded, one runs the risk of throwing away information which might lead to discovery of some unexpected phenomenon in the experiment. Important discoveries have resulted from apparently anomalous data. One could take the point of view that there is never any justification for discarding data on purely statistical grounds unless there is a definite reason for suspecting that a particular observation is invalid. In that case, there is nothing more to say except to advocate taking sufficient data such that the results are "unaffected" by the questionable observations.

Due to the extremely wide band and sensitive amplifier used in the detection scheme, strong transient electronic noises from the surroundings are liable to be picked up as signals by the counter, even though the input end of the amplifier has been subjected to meticulous shielding. These transient noises (e.g., arcing caused by bad contacts in electrical switches) are usually high frequency bursts

with very short durations that cannot be averaged out by the integration scheme. Due to the low signal frequency output, taking additional data to minimize the effects of these noises will require an unreasonable observation time. It is precisely with this problem in mind that a systematic treatment of the experimental data was considered.

Chauvenet's criterion⁸⁶ is frequently used for the purpose of rejecting outlying data. The criterion states that any one in a series of N readings will be rejected when its deviation from the mean of the series is such that the probability of the occurrence of such a deviation being as large or larger is less than $1/2N$.

In general, the probability for a measurement to occur in an interval within $k\sigma$ of the mean is

$$P(k) = \frac{1}{\sqrt{2\pi}} \int_{-k}^k e^{-x^2/2} dx \quad (2.56)$$

σ is the standard deviation given by

$$\sigma = \sqrt{\frac{1}{N-1} \sum_{i=1}^N (R_i - \bar{R})^2} \quad (2.57)$$

and \bar{R} is the mean value of the readings,

$$\bar{R} = \frac{1}{N} \sum_{i=1}^N R_i \quad (2.58)$$

Eq. (2.56) is the integral of the Gauss or normal error function and numerical values of this integral are extensively tabulated.⁸⁷

The probability for a measurement to occur in an interval larger than $k\sigma$ of the mean is $[1-P(k)]$ and according to Chauvenet's criterion, a reading will be rejected if

$$1-P(k) \leq \frac{1}{2N} \quad (2.59)$$

For example, if there are ten readings for one experimental measurement, i.e., $N=10$, then

$$P(k) \geq 1-0.05 = 0.95$$

and from Ref. 87, $k \geq 1.96$

This means that a reading should be rejected if its deviation from the mean, $|R_i - \bar{R}|$, is greater than 1.96 times the standard deviation, σ . Table II-1 gives the magnitude of this deviation in terms of multiples k of σ for several values of N .

Table II-1
Maximum Acceptable Deviations in Accordance
with Chauvenet's Criterion

Number of readings, N	2	5	7	10	15	20	25
Ratio of deviation to standard deviation, k	1.15	1.65	1.80	1.96	2.13	2.24	2.33

This method of "filtering" the experimental data has been adopted in the present work. After the "anomalous" observations are eliminated in accordance with Chauvenet's criterion, the mean and the standard deviation are re-computed using the remaining observations. The criterion for discarding experimental data is carried out once more and, if necessary, the whole process is repeated until all observations are within the maximum acceptable deviation. For widely scattered data, the repeated applications of Chauvenet's criterion may lead to the elimination of most or all of the data. Fortunately, in the present work, it has not been necessary to carry out the procedure for more than once and in no case the elimination of more than two observations is required.

CHAPTER III

EXPERIMENTAL DETAILS

A. Description of Apparatus

1. General Features

The present experiment and the work of Shih²⁹ represent the first generation of molecular beam studies of heterogeneous chemical reactions in the Molecular Beam Laboratory of the M.I.T. Department of Aeronautics and Astronautics. Although the ideal design of an experimental setup involves the capability of controlling a maximum number of experimental parameters for studying heterogeneous reactions, the complexities introduced with each variable generally make it impractical to do so. An early decision was made to emphasize a system with a high detection sensitivity (i.e., capable of studying heterogeneous systems with reaction probabilities as low as 10^{-3} to 10^{-4}) together with reasonable flexibility (i.e., parameters such as incident beam angle, reaction product detector angle, detector angular resolution, to be readily varied). No velocity analyzing scheme, such as mechanical velocity selection or time-of-flight technique, was incorporated into the design because such a scheme usually implies a severe reduction in signal levels. In view of the high operating temperature range of the source and target, key components of the system were all designed to be water-cooled and

materials in the vacuum chambers were chosen to have minimum outgassing rates wherever possible. New parts, such as braided fiber glass insulators, were always degassed in a separate oven at temperatures of about 400°C before they were placed in the vacuum system, whereas metal components were subjected to repeated cleansing in solutions of trichloroethylene and acetone. An ultrasonic cleaner was also used to clean parts which could not be done by hand easily. Fabrication of the vacuum chambers made use of heliarc welding to exclude atmospheric gases and prevent the formation of nitrides and oxides on or in welds. Interior surfaces as well as all internal components of the vacuum chambers were mechanically polished whereas the exterior surfaces had sand-blast finishes. An overall view of the experimental setup is shown in Fig. 6.

2. Vacuum System

The vacuum system consisted of two separately pumped chambers -- an 18" diameter by 25" test chamber housing the target-detector assembly and a 12' diameter by 20" source chamber which housed the beam generating assembly. The two chambers were connected by a 12" diameter flanged opening, as shown in Fig. 7. Both were fabricated from stainless steel SS 304.

The test chamber, in the shape of a bell jar, had a 12" diameter flanged opening in its side, opposite to the flanged connection to the source chamber, for easy access

to the interior of the chamber without necessitating lifting up of the whole chamber. It was evacuated by a National Research Corporation 10,000 liters/sec, 16" oil diffusion pump (Model HS16) using Silicone D.C. 705 oil. Due to its relatively high conductance, a copper, chevron-type baffle, cooled by either liquid nitrogen or Freon 12 refrigerant, was used to prevent backstreaming of the pump oil vapor and to trap condensible gases. On top of the baffle was a 4" high, aluminum feedthrough ring with eight equally spaced 3" diameter ports. One of the ports was connected to a mechanical pump for vacuum rough-down purpose while the others were an assortment of electrical, mechanical and water feedthroughs. The water feedthroughs were mostly made in the laboratory, whereas the electrical feedthroughs were generally high voltage, hermetically sealed and of a commercial kind. The test chamber was placed directly above the feedthrough ring, whose inside diameter was equal to the chamber diameter, so as to achieve a minimum loss in pumping conductance. A stainless steel wire mesh was placed in between the baffle and the feedthrough ring -- the purpose of which was to trap any dropped objects. Though the pumping speed then was reduced somewhat, the saving in system downtime well compensated the minor drawback. All vacuum surfaces were sealed by single Viton-A "O" rings with Apiezon-L vacuum grease except the 12" diameter, aluminum cover plate for the

access opening, which had a double "O" ring seal, since it was subjected to repeated cycling. Two glass view ports were provided for monitoring the test chamber conditions: one (3" diameter) in the side of the chamber facing directly at the target surface was used to measure the latter's temperature with an optical pyrometer, and the other one (6" diameter) in the center of the cover plate of the access opening served to view mechanical alignment and allow source tip temperature measurement.

An interior view of the test chamber with the bell jar removed is shown in Fig. 8. The photograph was taken at an angle from the top to show all components and support structures. The main frame consisted of four 1" diameter stainless steel rods that were mounted vertically on a ring fixed to the inside of the feedthrough ring. Two platforms were supported by main frame cross bars that also provided rigidity to the structure. The upper platform supported the mass spectrometer analyzer tube and its magnet as well as the drive train for their rotation and translation motion. The drive train consisted of gears and linkages driven by Globe AC motors, whose planetary gear boxes were completely degreased and then lubricated with Silicone D.C. 705 pump oil. The rotation motion of the mass spectrometer was pivoted about the center-line axis of the target, thereby allowing measurements of the re-emitted particle flux angular distribution from the

target in the principal plane defined by the beam axis and target normal. The position of the source housing, as shown in Fig. 9 at its location relative to the target detector assembly, nevertheless limited the mass spectrometer rotation range. For example, at $\theta_i = 45^\circ$, $0^\circ \leq \theta_D \leq 90^\circ$, whereas at $\theta_i = 35^\circ$, $10^\circ \leq \theta_D \leq 90^\circ$. The translation motion of the mass spectrometer allowed for adjustment of the target-to-detector distance. As shown in Section II-C, the signal level is inversely proportional to l_{TD}^2 . A shortening of l_{TD} leads to an increased signal level and thus also signal-to-noise ratio. However, the price paid for this is reduced angular resolution.

The position of the mass spectrometer was monitored by two potentiometers, turning simultaneously with the rotation and translation motors and forming one branch of a Wheatstone bridge completed by two identical potentiometers located external to the vacuum chamber. The imbalance of the Wheatstone bridge induced by the rotation when the mass spectrometer was moved was manually nulled by the external pots, thereby establishing the position of the mass spectrometer in accord with previous calibration.

The lower platform (Fig. 8) supported the target assembly, which could be rotated as well as moved vertically. The up-and-down motion was necessary to provide the target

with one (down) position which did not interfere with incident beam measurements. The beam incident angle was varied by rotating the target while in the up position, in which case a geared potentiometer was engaged by a pin in the target support shaft. The rotation angle was then measured in a scheme similar to that for the mass spectrometer. θ_i could be varied from 0° to 90° . The motion of the target was actuated manually from outside of the vacuum system by means of a Consolidated Vacuum Corporation linear-rotary feedthrough (Model SP-50) located at one of the ports of the feedthrough ring. A 6" long flexible metal shaft (Stow Manufacturing Co. Model 13FC), encased in a 3/4" diameter tubular housing, served as the coupling between the linear-rotary feedthrough and the target support shaft.

The chopper and its collimators were also mounted on the lower platform between the target and the mass spectrometer detector. Rotation of the assembly about the target centerline was provided by a Globe AC motor. Alignment of the chopper with the mass spectrometer detector was accomplished by visually matching two wire pointers -- one on each component -- within an accuracy of $\pm 0.5^\circ$.

A schematic diagram of the test chamber interior arrangement is shown in Fig. 10.

Fig. 11 shows a view of the vacuum system from the source chamber side. The source chamber, in the shape of

a tee, was evacuated by an Edwards High Vacuum Inc. 300 liters/sec, 6" vapor booster pump (Model 9B3) using Silicone D.C. 704 oil together with a Freon 12 cooled copper chevron baffle. One side of the tee served as an access port whereas the other side was connected to an aluminum feedthrough ring similar in design and function to that of the test chamber. Bolted onto the feedthrough ring was a rectangular stainless steel source housing that protruded into the test chamber. The source support assembly could be moved vertically as well as in-and-out to provide both alignment and variation of source-to-collimator distance. It was driven manually external to the source chamber through rotary feedthroughs with flexible couplings and its position was calibrated against the number of turns of the crank handle. The source collimator, which consisted of a 0.003" thick tungsten foil with a 3/32" diameter hole mounted on a beryllium-copper holder, was bolted to the center of the end plate of the rectangular housing, which was water-cooled due to the proximity of the hot source and target. The source chamber was completely sealed by Viton-A "O" rings from the test chamber, excepting for the collimator hole. A 3" diameter glass view port was provided in the center of the cover plate for the access opening. An interior view of the source chamber is shown in Fig. 12.

The initial pump-down of both chambers from atmosphere was done by a NRC 100 CFM, 2-stage rotary gas ballast pump (Model 100-C), which also served as the backing pump for the two oil diffusion pumps. The exact pumping speeds of the diffusion pumps pertaining to the present experimental setup were determined by Shih.²⁹ A summary of the results is presented in Appendix B. Pressures in the vacuum system were measured by two General Electric hot filament miniature ionization gauges (Model 22GT115) with Granville-Phillips gauge controllers (Model 236). Both gauges were mounted in the respective feedthrough rings of the test and source chambers. The ion gauge calibration for different gases is given in Appendix C.

3. Target and Its Support

The target used in this experiment was fabricated from ultra pure isotropic graphite sheets (Grade DFP-2) obtained from POCO Graphite, Inc. The graphite sheets (0.005" thick, 4" x 6") were shipped individually sealed in air-tight plastic envelopes to avoid contamination and were not opened until ready for use. Though the process of purification was not known, the total impurity content of the graphite was stated to be less than 5 ppm with only traces of Fe, Si, Al and Mg. Except for degassing under vacuum, no special treatment of the graphite was performed. Some of its physical properties are shown in Table III-1.

Table III-1

Physical Properties of Graphite Target Material

Average Density	1.79 gm/cm ³
Maximum Particle Size	0.025 cm
Average Pore Size	4 x 10 ⁻⁵ cm
Coefficient of Thermal Expansion	8.3 x 10 ⁻⁶ (°C) ⁻¹
Thermal Conductivity at 40°C	0.289 cal/sec-cm-°C
Electrical Resistivity at 40°C	2.76 x 10 ⁻⁴ ohm-cm

The target, 1 cm x 2.6 cm, was clamped in the holder as shown in Fig. 13. The holder consisted of two water-cooled copper blocks, each with a screwed-on flat clamp, connected by an aluminum oxide plate which also served to insulate the two blocks electrically. The unit was mounted on the movable shaft with another Al₂O₃ plate in between for electrical insulation. The centerline of the target coincided with the axis of rotation for the mass spectrometer and chopper. A spring tension was applied to the target to prevent it from warping due to thermal expansion; this was done by fastening the upper copper block to the Al₂O₃ plate through a spring plate. A silver-plated beryllium copper sheet was connected to each of the copper blocks at the back side of the target. The sheets served as both radiation heat shields for the Al₂O₃ plate and thermal energy reflectors.

The target was heated resistively with a Hewlett-Packard DC power supply (Model 6269A). The water lines for cooling the copper blocks (1/16" diameter flexible copper tubing) served as the electrical conductors and they were covered by braided fiber glass insulators. The temperature of the target was monitored by an optical pyrometer through the 3" diameter view port. A spectral emissivity of 0.90 at a wavelength of 0.65μ was used for the graphite temperature calibration though the actual emissivity of a finely machined graphite surface varies from 0.90 to 0.95 with temperature and surface finish.⁸⁸ The resulting error at an observed temperature of 1400°K was about 10°K and in no case was the error greater than 1%. A correction for sighting through a clear glass window was also made according to the pyrometer manufacturer's recommendation. At a graphite surface temperature of about 1600°K , a total power input of 180 watts from the power supply was required.

4. Chopper and Its Collimator

Instead of a conventional slotted disc mounted on a motor shaft, a tuning fork chopper was used for modulating the molecular beam and re-emitted particle flux from the target. There are several advantages. The compact size makes it relatively easy for mounting and positioning, especially in the present case of rather limited space between the target and detector. No special sealing is

necessary as in the case for a high speed motor, since there are no parts that need lubrication. The driving voltage of the tuning fork can also serve as a reference point for the signal processing scheme; for a motor drive chopper, a separate setup such as a light-photocell combination would have been necessary. The tuning fork chopper has, however, the drawback of a fixed frequency. It cannot be readily used in experiments that require a variable chopper frequency as in the case of Olander et al.²⁸

The tuning fork chopper was ordered from American Time Products Dept. of Bulova Watch Co. The unit (Model L40 HHB) with frequency of 400 Hz was supposed to operate in vacuum and up to a temperature of 250°C. As it turned out, the unit was designed only for a bakeout, not operating, temperature of 250°C. Eventually, an almost completely custom-made unit with a frequency of 377 Hz was used. A picture of the chopper is shown in Fig. 14. This consisted of a fork driven by two electromagnets located at about the middle of each prong. Two stainless steel blades, soldered on top of the prongs by a special low temperature-high strength silver-based alloy (Gemini SA alloy from Nassau Alloys and Research Corp.), served as the chopper. They were placed such that the blades just overlapped in the stationary mode, giving equal open and shut times (i.e., a duty cycle of 0.5) when in operation. The blades were polished on the side facing the hot target to minimize

heat absorption and had a sandpapered finish on the back side so that any absorbed heat could be more readily radiated away due to the relatively higher emissivity. The tuning fork was bolted to an L-shape copper bracket with water-cooled coils silver-soldered on the surface facing the target. The bracket, excepting for a small opening for the passage of gas molecules, shielded the entire chopper assembly as well as a portion of the mass spectrometer ionizer. A tungsten sheet of 0.012 cm thickness with a 0.508 cm square opening was mounted between the chopper blades and copper bracket and served as the chopper collimator. The whole assembly sat on an aluminum plate that rotated about the target centerline as described in Section III-A-2.

The electromagnets were driven by an oscillator circuit (ATP Model 5A driver) and the exact frequency was determined by a General Radio Company Model 1191 digital counter. The chopper amplitude, viewed with a GRC Strobotac shining through the 6" diameter view port, was adjusted to cover the whole collimator opening. The shutter function, expected to be a half sine wave, was measured by a light-photocell scheme.²⁹ Fig. 15 shows the measured shutter function together with the driver voltage which was used as a reference point for signal processing. It can be seen that the chopper lags the driver voltage by approximately 90° (an exact phase lag of 90° was measured by a lock-in

amplifier). This phase lag was not unpredicted due to the inductive nature of the driving force. The shutter function was confirmed to be a half sine wave by comparing the magnitude of the photocell signal as displayed on the oscilloscope with that of the output of the same signal as processed by a lock-in amplifier (which measures the root-mean-square value of the fundamental component of the Fourier expansion of an input signal). The calculated value based on the maximum amplitude of the scope trace agreed with the lock-in amplifier output to within 2%.

Though the chopper assembly was completely shielded from the hot target except for the chopper blades, the heat flux still had an effect on the chopper operation nevertheless. The chopper frequency and amplitude were very stable up to a target temperature of 1700°K. A further increase in target temperature invariably resulted in an erratic behavior of the chopper, such as fluctuation of frequency and drastic reduction in amplitude. Subsequent reduction in target temperature alleviated this problem. No definite explanation could be found; possibly softening of the solder led to this effect since the chopper performance, especially the amplitude, depended heavily on the delicate operation of soldering the blades onto the prongs. Accordingly, the maximum target temperature was limited to 1700°K for all measurements except when degassing the target.

5. Mass Spectrometer

The mass spectrometer was a General Electric unit that consisted of a stainless steel analyzer tube (Model 22PT120) and a 3 kilogauss permanent magnet (Model 22PM103) for ion focussing and deflection. The analyzer tube consisted of an exposed Nier-type, electron-bombardment ion source; a 90-degree sector, double-slit magnetic analyzer with a 5 cm radius of curvature; and a 10-stage electron-multiplier ion detector. Originally, the analyzer tube was designed to mount directly on a vacuum system through the use of a 4 3/4" O.D. flange at the ion source. In the present application the analyzer was modified to be used inside the vacuum system and supported through the magnet. The flange was removed along with rerouting of some electrical connections to permit operation as a "flow through" ionizer. The original electron multiplier was replaced by an EMI Gencom Division 18-stage, venetian-blind type multiplier with BeCu dynode surfaces (Model D1AT) for higher gain and stability. Resistors (glass-encased metal film type) for the dynode chain were all spot-welded on the dynode stages and decoupling capacitors were installed between the last three stages and ground to avoid the need for large chain currents when measuring large amplitude pulses. The current output end was redesigned to provide complete shielding of the multiplier and electrical leads. The stainless steel housing of the multiplier was first

lined by a layer of 0.025 cm thick μ -metal to minimize magnetic pickup and then followed by a 0.14 cm thick copper enclosure with two BNC connectors at the end for signal and high voltage leads. The signal lead was a special coaxial cable with two braids of flat strips of silver-covered copper (Stripflex cable from Times Wire and Cable Company) for greater shielding efficiency, and it was connected to the input of the amplifier/discriminator through a one-pin BNC feedthrough to provide as much isolation as possible from other wirings. An overall view of the mass spectrometer is shown in Fig. 16.

The ion source consisted of an ion cage, two thorium coated iridium filaments (one being a spare), draw-out and deflection electrodes and the defining slits (entrance and collimating). An electron current was drawn from the filament to the ion cage. Inside the ion cage the neutral atoms and molecules diffusing into the cage were ionized by electron bombardment. The ions were drawn from the ion cage by a constant drawout potential and accelerated through a particular ion focussing potential (accelerating potential). The beam of ions thus formed was focussed by the deflection electrodes and passed into the magnetic analyzer through the defining slits.

The ion beam leaving the ion source consisted of particles having approximately identical energies and direction. The kinetic energy (K.E.) of the ions in the beam is

defined by:

$$\text{K.E.} = \frac{mv^2}{2} = qV_{\text{acc}} \quad (3.1)$$

When a charged particle moves through a magnetic field, it is subjected to a force acting perpendicular to both the field and the direction of the motion. This deflecting force (F_{mag}) has a magnitude given by:

$$F_{\text{mag}} = \frac{qvB}{c} \quad (3.2)$$

and equal to the centrifugal force on the particle; thus

$$F_{\text{mag}} = \frac{qvB}{c} = \frac{mv^2}{r} \quad (3.3)$$

Combining Eqs. (3.1) and (3.3) to eliminate v yields:

$$\frac{m}{q} = \frac{1}{2c^2} \frac{r^2 B^2}{V_{\text{acc}}} \quad (3.4)$$

Thus, for a given magnetic field strength, the mass of those particles which are deflected by the correct amount so as to strike the ion collector is inversely proportional to the ion accelerating voltage. The mass range is scanned, therefore, by varying the accelerating potential.

With the 3 kilogauss magnet, the mass spectrometer was able to cover a mass range of 2-200 AMU with unit resolution of m/q up to 50.

The electronic controller of the mass spectrometer (GE Model 22PC110) consisted of a chart recorder and three separate modules: electron emission control, signal readout and ion sweep control. The experiment demanded the viewing of a particular mass peak for long periods of time, and the circuit drift in the ion sweep control module was found to be unacceptable over the necessary time intervals. Subsequently, only the electron emission control module was used in the experiment. This contained the emission regulated filament power supply and the controls to adjust the draw-out and two deflection voltages, which formed and collimated the ion beam. The ion sweep control module, which provided the variable ion accelerating voltage for electrostatically scanning the mass range, was replaced by a John Fluke Manufacturing Co. DC power supply (Model 407DR) with the voltage measured by a digital voltmeter. The electron multiplier voltage generator was also replaced by a Hewlett-Packard high voltage DC power supply (Model 6516A) for stability. All leads were connected through a GE 8-wire, high voltage ceramic feedthrough (Model 22HN020). A picture of the instrument panels is shown in Fig. 17.

Under electron bombardment in the ion source, some of the gas molecules are dissociated into their constituent atoms. This gives rise in the mass spectrum to a mass peak for each fragment of the parent molecule. These peaks along

with the peak resulting from the parent molecule are known as the "cracking pattern" for that species. This cracking pattern is unique for each gas under a set of mass spectrometer operating conditions and is, in effect, used to determine the relative amounts of two species, both of which make a major contribution to the spectrum at identical masses. An overall calibration of the mass spectrometer for different gas species is given in Appendix C.

6. Amplifier/Discriminator

The output current from the mass spectrometer was fed into a SSR Instrument Co. amplifier/discriminator (Model 1120). A table of its specifications is given in Table III-2.

Table III-2

SSR Model 1120 Amplifier/Discriminator Specifications

Input Impedance	50 ohms
Overall Gain	2300 min.
Discriminator Sensitivity	25 mV to 500 mV, internal screwdriver adjustment
Rise Time	6 μ sec
Pulse-Pair Resolution	10 nsec
Maximum Input Pulse Amplitude for Linear Operation	500 μ V
Minimum Detectable Pulse Amplitude	50 μ V
Input RMS Noise Equiv. (50 ohm)	10 μ V (max)
Pulse Output, Current Source Output	20 mA, MECL compatible
Output Pulse Width	10 nsec between 10% points

The amplifier consisted of a low noise, current-mode stage having a 50 ohm input impedance followed by two current-mode stages and a base-grounded amplifier having a combined amplification of 350. The discriminator, preceded by a discriminator driver having an amplification of 7, was an internally adjustable tunnel diode discriminator having an adjustable threshold from 25 to 500 mV. It was followed by a line driver to permit connection over long lengths of coaxial cable. The A/D output could be used directly to drive high speed counting equipment requiring 1 volt or less signal amplitude.

The A/D was contained within a heavy walled aluminum housing with multiple internal shields. The input connector was a panel BNC jack, and all output and power connections were made through an Amphenol connector incorporating both coaxial connecting pins for signals and normal pins for power. The unit should be mounted in as close proximity to the electron multiplier anode connection as is feasible. This was done by strapping the A/D immediately adjacent to the signal output feedthrough and using a 6" double-shielded interconnecting cable. Careful filtering and decoupling of the electron multiplier high voltage power supply is mandatory to avoid coupling spurious pulses, ripple and noise into the electron multiplier anode circuit from the supply. This was accomplished by by-passing the last three dynodes to ground by high frequency, metal-encased capacitors of 0.01 μ F.

The power required for the A/D was supplied by the Digital Synchronous Computer.

7. Digital Synchronous Computer

The signal pulses were processed by a SSR Digital Synchronous Computer (Model 1110). It is a highly versatile digital counting and computing instrument that consists of:

- A. Two High Speed 8-digit Scalers.
- B. A crystal controlled Master Clock for accurate timing.
- C. An Arithmetic Processor which converts the counter outputs, their sum and their difference into "floating point" form (3 significant digits and exponent).
- D. A Preset Counter which preselects chopper cycles, time, or input events, depending on the mode of operation.
- E. A Preset Counter for chopper sampling time.
- F. Front panel controls and display.

Its specifications are given in Table III-3.

Table III-3

SSR Model 1110 Digital Synchronous Computer Specifications

Pulse Pair Resolution	12 nsec
Maximum Count Rate	85 MHz
Crystal Clock Accuracy	.01% (long term) 1 part in 10^8 (short term)
Gating Symmetry (Chopper Mode)	10 nsec or 1 part in 10^8 , whichever is greater
Deadtime between Successive Main Cycles	67-85 μ sec
Capacity of "A" and "B" Counters	10^8 counts BCD
Input Signal Pulses	Negative 1 V min (5 V max) Duration (FWHM) 10 nsec (min)
Chopper Reference Signal (or Sync Trigger)	± 50 mV min (5 V max) Adjustable. Inputs may be operated in parallel or individually.
Digital Output	Four 16-bit full parallel words.
Preset Scale Factor	Three significant figures plus exponent for time (μ sec), counts, or chopper cycles. Range: 001 to 999×10^6 .

The DSC was operated in the "chopper" mode as described in Section II-B. An external "chopper trigger" was used to create two counting periods per chopper cycle. During each counting period, counts were stored either in counter "A" or counter "B". Usually when the chopper was open, counts were stored in counter "A" (Signal + Background) and when it was closed, counts were stored in counter "B" (Background). The total counting time was determined by selecting the number of chopper cycles (up to 10^9) on the front panel preset switch whereas the counting duration for each chopper cycle was set on the rear panel preset switch labeled "Chopper

Sampling Time" (1 μ sec to 1 sec). Upon finishing a counting cycle, the results (A, B, A+B, A-B) were selectively displayed in three significant figures, plus exponent, plus sign. An automatic mode was available, in which case each time a counting cycle ended and the display was updated, a new counting cycle would begin.

Since the driving voltage of the tuning fork chopper was used to trigger the DSC sampling gates, a phase adjusting scheme was necessary to allow for the difference in phase of the chopper opening and the driver voltage, and particle transit time. Originally, a delay circuit was supposed to be incorporated in the DSC and could be activated by the addition of a potentiometer at appropriate points in the circuit. It was found, however, that such an approach brought about an instability in the circuit and caused an erratic behavior of the unit. This phenomenon was confirmed by SSR designers, who conceded that the phase delay mode of the unit was not yet fully debugged. Subsequently, a Rutherford Electronics Co. pulse generator (Model B7B) was used to adjust the opening times of the DSC counter gates.

A timing diagram for the phase adjusting scheme is shown in Fig. 18. The driving voltage of the tuning fork was used to trigger the pulse generator, which in turn produced a rectangular pulse of adjustable amplitude, duration and delay. The pulse was adjusted to equal on-off time and fed into the DSC as trigger with the delay set to maximize signal output.

The exact delay time was monitored continuously by a General Radio interval counter. A schematic diagram of the signal processing procedure is shown previously in Fig. 4.

8. Beam Source

A cross-section diagram of the beam source is shown in Fig. 19. The source plenum chamber consisted of a closed end 1/4" O.D. thorium oxide (thoria) tube of 1/32" wall thickness and 2 1/2" in length. A 0.010" diameter hole in the closed end, drilled by means of an ultrasonic wire drilling technique in the M.I.T. Ceramics Laboratory, served as the source orifice. The front 1 1/4" portion of the tube was heated by a helically wound tungsten ribbon filament (0.010" x 0.025") of approximately 12 coils. The whole heating section was protected by a spiral radiation shield for its compactness, effectiveness and convenience of construction.⁸⁹ The shield was made by rolling a sheet of 1 1/2" x 15" x 0.005" thick tungsten into a spiral of approximately six layers each separated by two crinkled tungsten strips. The shield, about 3/4" in diameter, was supported by two alumina washers fitted over the thoria tube. The thoria tube was adapted to a water-cooled BeCu block with two Swagelok fittings and a pressure tap. The metal-to-thoria seal in the source fitting was achieved by two gold "O" rings with an indium "O" ring sandwiched in between. This solution was arrived at after repeated experimentation.

At high source operating temperatures, the indium "O" ring had actually melted but was retained in the two gold "O" rings gap by surface tension, thereby maintaining an effective seal. The gas inlet line was connected to the other Swagelok fitting and the source holder was bolted onto an all stainless steel source support carriage assembly that provided fore-aft and up-down motion with respect to the source collimator as described in Section III-A-2. Two views of the source as mounted on the carriage assembly are shown in Fig. 20.

The tungsten ribbon filament was heated by a homemade AC power supply capable of putting out 5000 watts. All electric power connections in the vacuum chamber were 1/4" diameter solid or stranded copper leads for good heat conduction, since there were no provisions for water cooling.

9. Gas Inlet System

A schematic diagram of the source gas inlet system is shown in Fig. 21. Ultra pure grade molecular oxygen was supplied by AIRCO that needed no further purification for use in this experiment. A lot analysis of the gas impurities is shown in Table III-4.

Table III-4

<u>Impurity Contents of O₂</u>	
<u>Impurity</u>	<u>PPM</u>
Kr	10.5
N ₂	3.8
Xe	0.276
Hydrocarbons	< 0.5
H ₂ O	0.8

Gas from the cylinder first passed through a cold trap that was employed to condense water vapor and other condensibles from regular grade oxygen that was used earlier. The gas flow rate was then controlled by a Granville-Phillips "variable leak" diaphragm valve (series 203) with conductance continuously variable from 100 cc/sec to less than 10^{-10} cc/sec. By setting the upstream supply pressure at 10 psig, the valve was found to be quite satisfactory in maintaining a typical flow rate of 2×10^{-4} cc/sec. Any variation of the flow rate, however, required an adjustment time of up to half an hour. The source tube pressure was measured, at the point of the pressure tap in the source holder block, by a Wallace-Tiernan 6" dial absolute pressure gauge (0.1 - 20 torr), which was calibrated against a trapped McLeod gauge. A calculation showed that less than a 1% correction was necessary to allow for the pressure drop from the pressure tap point to the source tip. The gas supply line was

evacuated by a Welch mechanical pump with a cold trap to prevent backstreaming of pump oil. All gas lines were soft copper tubings, which had been thoroughly cleaned by trichloroethylene and acetone. The valves were Nupro vacuum bellows valves.

10. Optical Pyrometer

The temperatures of the source and target were monitored by an optical pyrometer made by the Pyrometer Instrument Co., Inc. The "Pyro Micro-Optical Pyrometer" was a telescopic, disappearing filament type with vernier horizontal and vertical adjusting gears. It was capable of measuring temperatures of targets smaller than 0.001" in diameter and had a direct reading galvanometer with overlapping black-body scales from 700 - 3200°C. The galvanometer was compensated against variations in ambient temperatures and had a suppressed zero in order to permit maximum use of the full length of the scale. Temperature measurements were reproducible within two or three degrees Centigrade.

An optical pyrometer, however, determines only the brightness temperature of an incandescent body at the mean effective wavelength between the brightness temperature and the color temperature of the body. If the spectral emissivity of the body is known, the temperature of the body may be determined from the following equation using Wien's radiation approximation⁹⁰:

$$\frac{1}{T} = \frac{1}{T_B} + \frac{\lambda_e}{C_2} \ln \epsilon_{\lambda_e}(T) \quad (3.5)$$

where λ_e is the mean effective wavelength
 $\epsilon_{\lambda_e}(T)$ is the spectral emissivity at λ_e
 C_2 is the second radiation constant, 1.432 cm-°K
 and T_B is the brightness temperature of the body at λ_e

A table listing the true temperatures corresponding to various emissivities and brightness temperatures for $\lambda_e = 0.65\mu$ was provided by the pyrometer manufacturer.

Beam Properties and Source Performance

The oxygen beam was formed by collimating the effusive flux from the circular source orifice. To ensure that Knudsen flow existed, both the source pressure and temperature were maintained at levels such that the source gas mean-free-path was greater than or equal to the critical orifice dimension -- in this case the wall thickness, L , since it was greater than the orifice diameter, D . Namely,

$$Kn = \frac{\lambda_s}{L} = \frac{kT_s}{\sqrt{2} p_s \pi \delta^2 L} \geq 1 \quad (3.6)$$

For O_2 , $\delta \approx 3.0 \times 10^{-8}$ cm and with $L = 0.080$ cm, Eq. (3.6) implies the criterion

$$3.27 \times 10^{-4} \frac{T_s}{p_s} \geq 1 \quad (3.7)$$

where T_s is in °K and p_s is in torr.

For 0, the criterion for Knudsen flow (Eq. (3.6)) is less stringent, since $\delta_o < \delta_{o_2}$. Accordingly, the following discussion is restricted to molecular oxygen only. Throughout the experiment, Eq. (3.7) was nearly always adhered to except in some cases when the source was operating at room temperature. In order to achieve $\lambda_s/L \geq 1$ at room temperature, $p_s \leq 0.10$ torr. The drawback for this low source pressure, of course, is a low centerline intensity, which means a low signal level. Since the calculation of the absolute reaction probability (as given in Eq. (2.52)) depends partly on the assumption of a Knudsen source to interpret the measured incident beam signal, the only data that were used to calculate such quantities were those that satisfied Eq. (3.7). However, for measurements that did not require a precise knowledge of the incident beam (such as the relative angular flux distribution from the target), the source was operated at higher pressures to save, primarily, signal integration time. Such an approach was justified by comparing the angular distributions measured with the source operated at $Kn = 1$ and at Kn as low as $1/4$; no difference of the angular distributions was observed. The lower limit of $Kn = 1/4$ was chosen to avoid both an excessive increase in the background O_2 pressure and a radical departure from the ideal channel source. The departure from an ideal source at low Kn is illustrated in Fig. 22 that shows the detected incident beam centerline

signal versus source pressure for a room temperature source. The straight line is the theoretical centerline intensity for Knudsen flow, which is directly proportional to the source pressure as can be seen in Eq. (2.4). As expected, the measured signal at higher source pressure fell short of the theoretical value due to the departure from Knudsen flow. This method of increasing centerline intensity, though resulting in a small loss in beam directivity or "peaking", was frequently used in practical application of a channel source to fully utilize the source chamber pumping capacity. Theory has been developed to predict the variation of beam intensity with source pressure. Interested readers are referred to, for examples, Refs. 91 and 92.

The direct experimental verification of the centerline intensity of a channel source requires a difficult absolute calibration. Instead, an indirect method of checking the total leak rate and determining the angular flux pattern was used to evaluate the source performance.

The total flux out of an effusive source is

$$F_s = K \frac{p_s}{\sqrt{2\pi m_s kT_s}} \left(\frac{\pi D^2}{4}\right) \quad (3.8)$$

It can be seen that at constant leak rate, the source pressure will adjust to the source temperature as

$$P_s \propto \dots \quad (3.9)$$

if the Clausing factor, K , remains unchanged as will be the case when the Knudsen flow criterion (i.e., $Kn \geq 1$) is satisfied at all times.

The relationship in (3.9) was tested by providing a fixed leak through the Granville-Phillips "variable leak" valve (i.e., ensuring a constant F_s) with the source at initial conditions of $p_s = 0.1$ torr and $T_s = 300^\circ\text{K}$ (which satisfied the Knudsen flow criterion). The source temperature was then raised and the corresponding source pressure was recorded, with ample waiting time in between change of source temperatures to ensure equilibrium conditions. The results are shown in Fig. 23 and they clearly verified the relationship in (3.9). The implication of such a result was that the source functioned as an effusive source within the pressure and temperature range tested (which, incidently, satisfied $Kn \geq 1$ at all times). It should be pointed out that there was practically no dissociation of the oxygen under these test conditions. Otherwise, the result could be interpreted differently, as the presence of O could lead to a different leak rate.

One could further check the Clausing factor by measuring the total leak rate out of the source. This could be done quite easily by feeding the source from a

constant pressure reservoir and measuring the volumetric change of the reservoir. However, due to the extremely low flow rate of the source and the requirement of an upstream pressure of more than one atmosphere for satisfactory operation of the GP "variable leak" valve, a reasonable volumetric change of the reservoir (e.g., a change of 10 cm^3) would require a flow time of more than 20 hours. Since an accurate knowledge of the total flux rate from the source was not important as compared to the assurance of an effusive source in this experiment, this measurement was by-passed.

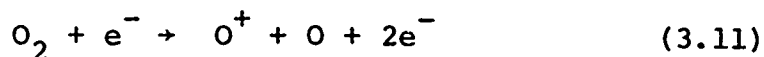
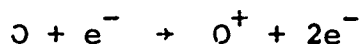
The source flux angular distribution at different source temperature is shown in Fig. 24. No absolute measurement of the intensity is necessary in this case. The angular distribution was measured by rotating the mass spectrometer with respect to the target axis. The geometry is also shown in Fig. 24. The angle of rotation of the detector, ϕ_D , and the angle measured from the source tip, ϕ_S , are related by

$$\tan \phi_S = \frac{\sin \phi_D}{\cos \phi_D + l_{ST}/l_{TD}} \quad (3.10)$$

The detector width was set by the amplitude of the chopper. At $\phi_S = 0$, the detector width corresponded to a $\Delta\phi_S$ of 0.6° . Due to the geometry of the detector with respect to the source, ϕ_S was limited to cover the range from $-3 \frac{1}{2}^\circ$ to 7° .

Though a far from complete pattern of the source emission was obtained, the ϕ_s range measured was sufficient to evaluate the uniformity of the incident flux on the target, since the target subtended only a source angle of less than 6° . The angular flux distribution for an ideal cosine source is plotted in Fig. 24 for comparison. As can be seen, the angular flux distribution of the source at the temperature range tested (300° to 2200°K) deviated little from the ideal Knudsen source; it was more lobular, if any, as would be expected for a channel source. In taking the data, the O_2 mass peak ($\frac{m}{q} = 32$) was monitored for $T_s \leq 1800^\circ\text{K}$ whereas at $T_s = 2200^\circ\text{K}$ the O mass peak ($\frac{m}{q} = 16$) was monitored. Though it cannot be said that the signal level at $\frac{m}{q} = 16$ represents solely the atomic oxygen flux in the beam (as will be discussed later), the measurement nonetheless is an indication of the O level. In any case, for the small source angle subtended by the target, the non-uniformity of the incident flux on the target can be quite safely neglected.

It is quite difficult to separate a recorded mass peak signal level in a mass spectrograph into fractions that are contributed by different mass species. For example, at $m/q = 16$, even with the presence of only O and O_2 , the signal level represents constituents of O_2^{++} and O^+ , the latter of which arises from both O and the dissociative ionization of O_2 , namely



Additional contribution to the signal level is possible with the presence of other species such as water vapor.

To avoid such complication in interpreting the mass spectrograph, the ratio of O-to-O₂ signal level (more precisely the ratio of m/q = 16 and m/q = 32 mass peak signal levels) was used to determine the degree of oxygen dissociation in the beam. In this scheme, the O/O₂ ratio was first obtained for a pure O₂ beam, which established the "cracking pattern" of O₂ under the operating conditions of the present mass spectrometer. The O/O₂ ratio was then measured for a dissociated oxygen beam. Comparisons were made between the two O/O₂ ratios to infer the degree of dissociation of the dissociated oxygen beam.

The O/O₂ ratio for pure O₂ was found to be equal to 0.087. This value was constant (within 3%) for both "stagnant" O₂ as occurred in O₂ background gas and "directed" O₂ as in the O₂ beam flux for source temperatures from 300° to 1800°K. This result was contrary to that obtained by Lam⁷⁶, who found that monoenergetic molecular oxygen beams generally gave a smaller O/O₂ ratio than that of a stagnant system of the same composition. That discrepancy was attributed to the present case of a relatively large mass spectrometer ion draw-out energy (approximately 200 eV)

compared to the beam energy (maximum 0.4 eV) and the Maxwellian velocity distribution in the beam. After ionization and being subjected to the draw-out potential, a particle has practically no memory of its previous energy and direction, making them irrelevant to the detected O/O₂ ratio.

In principle, one could calculate the atomic oxygen level in the beam once the cracking pattern of O₂ was established and provided that such parameters as ionization cross-section, mass spectrometer ion draw-out efficiency and electron multiplier dynode ion-to-electron conversion efficiency were accurately known. However, such parameters could only be obtained through calibration, which in the present case was not possible. Instead, a calculation of the O/O₂ ratio was made for a dissociated beam at a particular source pressure and temperature assuming a mass spectrometer sensitivity for the atomic oxygen, as defined in Eq. (2.23). This assumed mass spectrometer sensitivity for O, an educated guess to begin with, was used to calculate subsequent O/O₂ ratios for different beam compositions as generated by different source conditions. Comparisons were made between the "calculated" and measured O/O₂ ratios while the mass spectrometer O sensitivity was continuously adjusted to provide a most consistent fit. Such a table showing the calculated and measured O/O₂ ratios that covers the entire range of source

conditions that was used to generate atomic oxygen is given in Table III-5.

Table III-5
Dissociation Level as Shown by O/O₂ Ratio

<u>p_s (torr)</u>	<u>T_s (°K)</u>	<u>F_O/F_{O₂}</u>	<u>O/O₂ Ratio</u>	
			<u>Calculated</u>	<u>Measured</u>
0.10	2220	0.49	0.1311	0.128
0.20	2205	0.31	0.1139	0.112
0.24	2200	0.27	0.1091	0.111
0.26	2110	0.14	0.1031	0.100

For the calculated O/O₂ ratio in the table, an $S_{O}^{*}/S_{O_2}^{*}$ ratio of 1/8 was used. This value appears quite reasonable in view of the reduced ionization cross-section of O (approximately equal to 1/4 of the ionization cross-section of O₂), and the fact that the mass spectrometer output was maximized on the O₂ rather than the O peak. In measuring the O/O₂ ratio, the mass spectrometer was always "tuned" to the O₂ peak. This provided a consistent basis for the measurement, since it was possible to arrive at a different O/O₂ ratio for the same beam composition if the mass spectrometer was "tuned" to the O peak instead. The consistency of the measured and calculated O/O₂ ratios over the entire source operating range, as shown in Table III-5, clearly indicates the satisfactory operation of the source in regard to the equilibrium dissociation level of oxygen.

The phase lag of the incident beam due to the particle transit time was measured for different source temperatures and is shown in Fig. 25. The results agreed quite well with the theoretical predictions of Harrison et al.⁸³ However, due to the circuit drift of the pulse generator and the rather insensitive nature of the phase measurement, the measured phase shift was only accurate to within $\pm 3^\circ$. Accordingly, it was not possible to separate out the O and O₂ cracking signals at $m/q = 16$ for a dissociated beam by a phase lag discrimination technique, since at a source temperature of 2200°K a phase lag difference of only 4° existed for monoenergetic O and O₂ beams. With the amplitude dispersion effect for a Maxwellian beam, it was impossible to distinguish O and O₂ by the phase lag method.

Up to a source temperature of 1800°K, the source functioned as expected and the only necessary precaution was an allowance for ample time for the source to reach thermal uniformity during the heat-up and cool-down processes. A four-hour heat-up time was required to avoid cracking of the thorium tube due to thermal shock, while a two-hour period was sufficient for the cool-down process. When the source was operated in the oxygen dissociative regime (i.e., source temperature greater than 2100°K), rapid oxidation of the tungsten filament by the background oxygen in the source chamber invariably took place. At a source temperature of 2200°K and source pressure of 0.20

torr, the filament burnt out after approximately 10 hours of continuous operation. Efforts spent to prolong the filament life by using heftier tungsten filament and shielding it from direct impingement of the reflected oxygen from the source collimator were of little avail; a lengthening of only a few hours of the filament life was achieved. This problem of limited filament life at $T_s \geq 2100^\circ\text{K}$ was finally remedied by positioning the source close to the source collimator so that virtually all oxygen particles effused into the test chamber. This remedy would ordinarily be impossible, since the increase in noise level in the test chamber due to the background oxygen would most likely be intolerable. Fortunately, due to a combination of extremely low pressure of the source ($0.1 \sim 0.25$ torr) and a huge pumping speed in the test chamber (10,000 liters/sec), only a longer integration time and a slight correction had to be made, as discussed previously in Section II-C. The source has been operated under this condition for more than 100 hours and exhibited neither a visible change nor change of electrical resistance of the tungsten filament. The minor drawbacks of longer integration time and a correction in data reduction well compensated the formidable task of replacing the filament, which was both uneconomical and time consuming.

C. Experimental Program and Procedure

1. Experimental Program

From the initiation of the present study, it had been realized that a major effort was to be spent on the experimental hardware -- in particular, the high temperature source and the pulse counting equipment. Before the present vacuum system was available, source tests had been conducted in a small vacuum system in regard to the maximum operating temperature, temperature gradient between the heating element and thoria, filament life, metal-to-thoria seal, and so on. The small vacuum system was quite useful in this respect -- in particular, due to its short vacuum cycling time, many ideas could be tried out rather readily. Though an understanding of the source performance was far from complete, the results obtained in that period proved to be quite valuable in arriving at the final design that was used in the experiment.

At the time when the vacuum system was ready for use, the most promising source configuration consisted of two concentric thoria tubings forming the annular Knudsen cavity with a tungsten rod inside the smaller tubing serving as the heating element. This source was installed in the source chamber and much of the room temperature beam data was obtained with that arrangement. At high source temperatures, cracking of the tubing occurred as a result of differential thermal expansions. Eventually, the source described in Section III-A was developed.

In view of the low beam intensity, transient studies, as carried out by Shih,²⁹ were not attempted. Instead, the emphasis was placed on experimental accuracy and the dependence of the reaction on relevant parameters. In order to separate out the individual effects of O and O₂ on the oxidation rate when using a mixed beam, the oxidation rate of O₂ had to be accurately determined. In fact, this was the first objective when the pulse counting system was installed. Comparison of room temperature O₂ results with those of Shih was used to evaluate the detection system. Hot O₂ beams were used after the detection system proved to be satisfactory. The dissociated beam measurements were carried out during the latter part of the experiment. Although "fast" time-response surface phenomena could not be detected, a time-dependent nature of the oxidation rate for both O and O₂ was observed.

While it was planned earlier to also study the oxidation rate of pyrolytic graphite (made by depositing benzene vapor on a tungsten or isotropic graphite substrate), an expected drop in signal level (which meant a higher sensitivity requirement than the present detection system) precluded this study.

2. Mechanical Alignment

The mechanical alignment of the experiment consisted of two requirements. The first requirement was to position the beam axis, the target normal and the center points of

the chopper and mass spectrometer ionizer all in the same horizontal plane. This was partially accomplished by adjusting the platforms that supported the mass spectrometer, target and chopper, as seen in Fig. 8, by means of level and height gauges with the test chamber removed. The target support platform served as a datum. The second alignment criterion was that the beam axis, target surface, center points of the chopper and ionizer should also lie in a common vertical plane. Again, the target, chopper and ionizer were aligned with the test chamber removed and with the aid of two plumb lines suspended from the mass spectrometer platform. The axes of rotation of the mass spectrometer and target should coincide; this was accomplished by continuously adjusting the platforms' support so that the edge view of the target was always viewed as a line through the centerline of the ionizer. While the procedure may sound complicated, many of the alignments were incorporated into the design. With the source and test chambers assembled, the alignment of the source with the rest of the components completed the procedure. With the aid of a telescope, the source tip orifice was first positioned at the center of the then-aligned ionizer; the source collimator was then centered around the source orifice. A picture of the aligned assembly as viewed through the test chamber access opening was shown previously in Fig. 9. The mass spectrometer

translation and rotation potentiometers were calibrated against the known gear ratios once the alignment was completed whereas the target rotation potentiometer was calibrated against the mass spectrometer.

3. Typical Operating Procedure

A set operating procedure was always followed to ensure both data consistency and the attainment of steady state conditions of the target in view of the foreseen dependence of the reaction rate on previous target history.

The system was maintained in vacuum whenever possible to minimize contamination of the target and electron multiplier dynode surfaces. When the target was first installed, it was degassed under vacuum ($< 10^{-7}$ torr) at 1800°K for over 24 hours. The oxygen beam was then turned on with the target at about 1300°K (the temperature for maximum reaction probability) for at least 48 hours to activate the surface after annealing and before any measurements were carried out. This procedure of degassing and activation was repeated whenever vacuum was broken and after the subsequent pump-down.

A typical day of experimenting began by switching the test chamber baffle from Freon 12 to liquid nitrogen cooled and turning on all electronic equipment, in particular the mass spectrometer controller and pulse generator, for warm-up. This was followed by the slow process of

simultaneously heating up the source and adjusting the source leak for a hot beam experiment. The source inner wall temperature was continuously monitored through the orifice by the optical pyrometer viewing through the 6" diameter view port on the test chamber cover plate. A spectral emissivity of 0.20 at $\lambda_e = 0.65\mu$ for the thorium, as furnished by the manufacturer, was used for its temperature calibration. A source heat-up time of approximately 4 hours was required, after which all other equipment had well reached their steady state operating conditions.

The incident beam was first monitored to check all equipment as well as to record its intensity and O/O_2 ratio. The planned experiment was then carried out with the Bayard-Alpert ionization gauges turned off about 15 minutes prior to the data taking; this step was taken since it was found that the interaction of background oxygen with the hot filament gave rise to an increased $m/q = 28$ background signal, apparently due to the CO produced by the reaction of the impurities in the tungsten filament with the oxygen. During the experiment, the functioning of all equipment was continuously checked and the quality of vacuum was monitored by the background count rates from the DSC. At the end of an experiment (which at times ran for more than 24 hours in a stretch), the source was slowly cooled down (over a time span of

2 hours) and the target was kept at 1300°K with the beam on. The baffles were switched back to Freon 12 cooling and the whole system remained in vacuum.

4. Data Processing

The DSC has the capability (with the addition of a plug-in Serial Converter circuit board) to transmit data to any serial digital device such as a Teletype printer, a tape punch, or a time-shared computer for fast or real-time pre-programmed data processing. Due to economics and the relatively small amount of data, all data were recorded by hand. Much of the data reduction was done with the aid of a Wang Laboratories, Inc. Model 380 programmable calculator and a Panasonic Model 850 electronic calculator.

CHAPTER IV

RESULTS AND DISCUSSIONS

A. Introduction

The experiment was carried out chronologically in two phases: the first phase concerned with the C-O₂ reaction whereas the latter was aimed at the C-O reaction. Though the C-O₂ reaction had been studied previously using a molecular beam technique,^{28,29} the present experimental set-up with its unique capability of varying several important experimental parameters made it worthwhile to further investigate the reaction. In particular, only one previous reference²⁹ considered the reaction product angular distribution and therefore a check on that work is worthwhile. The effects of beam energies and incident angles on the oxidation rates may be helpful in understanding the reaction mechanisms. In addition, precise and consistent O₂ data are required for the specific subtraction process intended to deduce the O results, as discussed in Section II-D.

B. O₂ Scattering from Graphite

The angular distribution of scattered O₂ from the graphite target was the first measurement made for this gas-surface interaction. One of the purposes of this measurement was to evaluate the detection scheme and, in particular, to test such theoretical prediction as the

signal-to-noise ratio after integration with respect to integration time, as shown in Eq. (2.13). The system behaved quite as expected. For example, a signal fluctuation level of approximately 25 percent was obtained after each integration period of 5 minutes for a given operating condition (i.e., at given R_S and R_N count rates) whereas prolonging the integration period to 30 minutes resulted in a signal fluctuation level of approximately 10 percent, thereby proving the square root dependence of the $(S/N)_{int}$ ratio on the integration time.

Results of the angular distribution of scattered O_2 are shown in Figs. 26-28. Theoretical distributions based on a cosine flux distribution are plotted for comparison. It should be pointed out that the theoretical cosine distribution deviates from that of both a point and infinite target; this is due to the target edge corrections for the present target-to-detector geometry. An exact analysis of the target edge corrections is presented in Appendix A. In any case, all theoretical angular distributions are plotted out with the present target-to-detector geometry in mind. Figs. 26 and 27 show the angular distributions of scattered room temperature O_2 at incident angles of 45° and 60° respectively. The target temperatures were essentially all about $1400^\circ K$. As can be seen, the scattering patterns resembled those of diffuse scattering independent of the incident angles tested. Similar results were obtained by

Shih,²⁹ who used nearly monoenergetic beams at an incident angle of 45° with target temperatures varying from 300° to 1760°K . In particular, Shih also found no apparent change of the angular distribution due to either target temperature or target history. This behavior can be attributed to the roughness of the target surface used in this experiment (incidentally, exactly the same type of isotropic graphite was used by Shih). If a molecule makes several collisions with a roughened surface before being re-emitted, the angular distribution of the re-emitted flux should be both insensitive to the incident angle and correspond to a random pattern (i.e., a cosine distribution). Similar arguments hold for the insensitivity of the scattered distribution in regard to the incident beam temperature. This is shown in Fig. 28 where a beam temperature of 1370°K was used; again, no apparent dependence on the incident angle was observed.

The "Maxwellian" beam temperature of the re-emitted O_2 at $T_T = 1370^\circ\text{K}$ was measured to be about 1000°K (i.e., $\phi \approx 12^\circ$) regardless of detector angle. This implied an incomplete energy accommodation of O_2 on hot graphite. However, such an interpretation should be taken with some reservation due to the inherent insensitive nature of the phase shift measurement and the experimental accuracy, as discussed previously in Sections II-D and III-B. At the operating target temperature of 1400°K , an inaccuracy in

the phase shift measurement of only 2° could raise the possibility of a fully accommodated oxygen molecule. Nonetheless, results of Shih indicate that the energy accommodation for O_2 adsorption on graphite is less than unity for a hot target. For a surface temperature range of 950° to $1750^\circ K$, Shih found that the "Maxwellian" beam temperature of the re-emitted O_2 was insensitive to the target temperature and remained at a constant value of about $900^\circ K$ with a fluctuation of $\pm 150^\circ K$. The interpretation of the measured phase lag was based, however, on the assumption of a Maxwellian velocity distribution of the re-emitted flux and that by no means was confirmed.

Previous investigations in the thermal accommodation of different gases on graphite revealed similar trends. Meyer,⁹³ in his study of the energy exchange between argon and a hot graphite surface, noted the existence of a critical surface temperature above which the temperature of the argon leaving the surface remained constant. Recently, Siekhaus et al⁹⁴ studied the energy of O_2 scattered from pyrolytic graphite using molecular beams. In the target temperature range of 1000° to $2200^\circ K$, they found a corresponding re-emitted O_2 Maxwellian temperature range of 700° to $900^\circ K$, again indicating an incomplete energy accommodation and its weak target temperature

dependence. Furthermore, the beam temperature (from 300° to 1300°K) was found to have no effect on the observed phase shifts. This was attributed to trapping of the gas on the surface for a sufficiently long period such that the initial state is forgotten; the result was apparently in agreement with the present measured O₂ scattering patterns in regard to both incident beam angles and temperatures.

C. Reaction Product and Its Angular Distribution

For both O and O₂ reactions, CO was found to be the only detectable reaction product. The CO₂ signal, barely observable in the background count rate, was estimated to be at least two orders of magnitude lower than that for CO and a quantitative measurement of the signal level was simply beyond the sensitivity of the present detection scheme. This finding was in agreement with that of Shih, who used only molecular oxygen with a beam intensity almost two orders of magnitude higher than the present case. Both CO and CO₂ have been observed by previous investigators as products of graphite oxidation. However, as the target temperature is increased to above 1000°K for the C-O₂ reaction (the temperature range of the present experiment covers from 1000° to 1700°K), the ratio of CO to CO₂ is drastically increased with CO as the dominant product (at least one order of magnitude higher than CO₂).^{26,28} CO₂ detection from previous experiments,

a number of which were reviewed in Section I-B, can be partially explained by the presence of gas-gas collisions where CO in the gas phase is oxidized to CO₂ by the background O₂. Such a mechanism is clearly ruled out in the present case as well as similar experiments^{28,29} in which the background pressure is of the order 10⁻⁸ torr.

Batty and Stickney⁹⁵ have analyzed the chemical reactions of gaseous O₂ with solid surfaces under conditions of high temperature and low pressure. Using equilibrium considerations and without assuming a detailed kinetic model, they formed a thermodynamic model of reactive gas-surface scattering that correlates many features of existing experimental data. In particular, for the C-O₂ reaction, CO was predicted to be the dominant product for target temperatures above 800°K with a CO₂-to-CO ratio of less than 10⁻⁴.

There is scarcely any data, in particular the reaction product, on the C-O reaction at the temperature range covered in this experiment; however, those at lower target temperatures⁶⁰ indicated that CO was also the principal product. Subsequently, all future referrals to products of reaction are concerned solely with CO.

The angular distributions for CO desorption off the target are shown in Figs. 29 and 30 for different source temperatures and beam incident angles. Again, the target temperature was maintained at about 1400°K for all runs.

This temperature was chosen principally because the reaction probability was found to exhibit a maximum (thereby contributing to maximum CO signals and shortening of integration time) at $T_T \approx 1400^\circ\text{K}$. In addition, Shih²⁹ found that the angular distributions were independent of target temperatures. Since a typical set of angular measurements required an operating time of up to 10 hours, variation of the target temperature was not considered.

Fig. 29 shows the angular distributions of the CO flux from the target for a room temperature O_2 incident beam at incident angles of 45° and 60° . The results also covered a four-fold increase in incident intensity (as discussed in Section III-B). No apparent dependence of the angular distribution on the incident angles can be seen. It must be conceded, however, that the incident angles used did not encompass a wide range; this was due to both geometric constraints and a severe drop in signal levels at large incident angles (since the incident flux on the target varies as $\cos \theta_i$). Nevertheless, the incident angle range did represent a 41% change of incident beam normal momentum and a 22% change of tangential momentum. The insensitive nature of the CO angular distributions with regard to incident angles -- equivalently, normal and tangential momenta -- may be related to the fact that the first step necessary for a reaction to occur at the surface is adsorption of the gas molecules. Once adsorbed, a

molecule tends to have a lesser "memory" of its past history. While it may have an effect on the reaction probability (in the sense of affecting the sticking probability), the incident angle should have a minor or no influence on the desorption patterns of the reaction products, as indeed was found to be the case.

Similar results with respect to the CO desorption patterns corresponding to different beam temperatures were obtained, as shown in Fig. 30. It should be pointed out that two of the source temperatures -- 2200° and 2220°K -- represented dissociated beams with O-to-O₂ flux ratios of approximately one-to-two, but apparently no effects on the desorption patterns could be observed. The CO signals in these two cases were contributed almost entirely by the C-O reaction, since O was found to be more than ten times as reactive as O₂, as will be discussed later. The arguments for the unchanged CO desorption patterns suggested earlier for the case of room temperature O₂ beams may also be applied here. However, to draw the conclusion that the reaction sites for both O and O₂ are similar based on the similarity of the CO desorption patterns is certainly premature; the influence of the rough surface structure of the present target could very well dominate over the difference in desorption patterns, if any, arising from CO formed at different sites. The larger fluctuation of data observed at $\theta_D = 60^\circ$ (Fig. 30)

choice of isotropic graphite as the target material (primarily for its higher reaction probability than, say, pyrolytic graphite) has the drawback of a rather rough and uncharacteristic surface, resulting in both a possible broadening of desorption peaks and an insensitivity of the desorption patterns with regard to incident beam parameters (such as beam energy and incident angle). Clearly, additional studies must be made before an understanding of such a desorption phenomenon can be expected. The result does have an immediate significance in the sense that experimentally measured reaction probabilities (such as those measured by Olander et al²⁸), which assumed a diffuse desorption pattern may be questionable; the corrections of such results, if necessary, will be quite straight-forward once the angular desorption distributions for those carbon surfaces are known.

It should be pointed out that the measured "Maxwellian" beam temperature of the desorbed CO corresponded quite closely to the target temperature within the accuracy of the phase shift measurement. This behavior of a fully accommodated CO particle was in contrast to the partially accommodated scattered O₂. Such a difference is quite reasonable, since the formation of a reaction product involves a "completely trapped" oxygen particle and most likely the reaction product desorbs after equilibration with the target surface.

D. C-O₂ Reaction

Before the results are presented, some pertinent points about obtaining such measurements will be mentioned. The preliminary treatment of the target before any measurements was discussed previously in Section III-C-3. In addition, a waiting period of up to one hour was needed before data taking for each change of target temperatures. This step was taken to ensure: (1) the attainment of thermal equilibrium of the mass spectrometer ionizer components due to the change of heat flux as the target temperature was varied; (2) a steady state condition of the reaction surface.

It was found that the mass spectrometer ionizer performance (such as the controls for tuning to a peak) was affected by the heat load on it. This was apparently due to the differential thermal expansions of the different materials making up the ionizer components. The drift in tuning was particularly noticeable when the target was first heated up. However, once the ionizer attained thermal equilibrium (approximately one hour after target heat-up), any subsequent variation of the target temperatures (in the range of 1000° to 1700°K) had a minimal effect on its performance -- an adjustment time of only about 5 minutes was required.

Shih²⁹ found that whenever the target temperature was varied, a finite adjustment time was necessary in order for the oxidation rate to reach a steady state value. The adjustment time depended on both the target temperature range and the direction of temperature changes. Such behavior has been reported previously^{27,28} as a "hysteresis" effect when a cyclic measurement was carried out over times that were short compared to the adjustment times. Basing the procedure on the transient measurement results of Shih, the experiment for steady state oxidation rates was carried out in such a way so as to avoid the hysteresis effect. Typically, the target temperature was first set at 1000°K and then increased at 100°K intervals (up to $T_T = 1700^\circ\text{K}$) after each measurement was made. For $1000^\circ\text{K} < T_T < 1300^\circ\text{K}$, a waiting period of 30 minutes was observed while for $T_T > 1300^\circ\text{K}$, the waiting period lasted for 1 hour. Such time spans between measurements seem adequate as there was little change in oxidation rates with longer waiting periods. Lastly, once a set of results was obtained, the target was brought back to about 1400°K with the beam on for at least 36 hours to "reactivate" the surface before another set of measurements was carried out.

The reaction probabilities of O_2 with graphite at different beam temperatures and incident angles are shown in Table IV-1. The reaction probability is previously defined by Eq. (2.27).

Table IV-1

Reaction Probabilities of O_2 at Different
Beam Temperatures and Incident Angles

θ_i	$T_B (^{\circ}K)$	$\bar{v} \text{ (cm/sec)}$	$\bar{v} \cos \theta_i \text{ (cm/sec)}$	ϵ_{O_2}
60°	300	5.23×10^4	2.62×10^4	1.56×10^{-2}
60°	1430	1.14×10^5	5.70×10^4	1.40×10^{-2}
60°	1875	1.31×10^5	6.55×10^4	1.62×10^{-2}
45°	300	5.23×10^4	3.70×10^4	1.66×10^{-2}
45°	1370	1.12×10^5	7.92×10^4	1.50×10^{-2}

Throughout the above measurements, the target temperature was maintained at 1385°K for comparison purposes (the variations of ϵ_{O_2} with target temperatures will be discussed later). Within a 5-fold increase in beam temperatures (i.e., beam energies) and a 2 1/2-fold increase in normal beam velocity components (shown in column 4 of the table), the reaction probabilities remain virtually constant within experimental accuracy (approximately 15% fluctuations) and show no definite dependence on either parameters. Olander et al,²⁸ using pyrolytic graphite, also found the reaction rate to be insensitive to the temperature of the incident beam ($300^{\circ}K < T_B < 1200^{\circ}K$) for the basal plane reaction. The constant reaction probability with respect to beam temperature implies one or both of two possibilities. Assuming that a beam molecule makes only one collision with the surface before reacting or scattering, then the results

suggest that the surface reaction kinetics are truly independent of the thermodynamic state of the incident gas molecules such as translational energy, rotational and vibrational excitations. On the other hand, if a beam molecule made several collisions with the surface before reacting or being re-emitted (most likely in the case of a rough and uncharacteristic surface), then the molecule would be preheated to (or nearly equal to, depending on the thermal accommodation coefficient) the target temperature regardless of the incident beam temperature and a beam heating experiment would be inconclusive. Similar possibilities hold for the dependence of the reaction probability as regard to angle of incidence. In view of the rough surface nature of the present target, the latter case probably prevails. The roughness of the target surface, apart from examination under a microscope, is further confirmed by the measured re-emitted oxygen flux distribution, which is a diffuse pattern regardless of beam and target temperatures as well as angle of incidence, as discussed previously in Section IV-B.

Though Olander et al started with a polished pyrolytic graphite sample, they noted definite texturing of the surface due to oxidation after removal from the vacuum system following several months of experimentation. Scanning electron micrographs of the target before and after the experimental program showed that the relatively high

oxidation rates represent conditions far too chaotic to permit formation of the nearly hexagonal etch pits observed in the low temperature oxidation of single crystal flakes of natural graphite.⁴⁵ The actual area of the surface is undoubtedly considerably greater than the superficial area. Accordingly, it is difficult to contend that the reaction occurs upon perfect basal planes of the graphite lattice, despite the fact that a specimen of this orientation was utilized -- a result that could lead to similar findings with the present work in regard to the insensitiveness of the reaction probability with respect to beam temperatures.

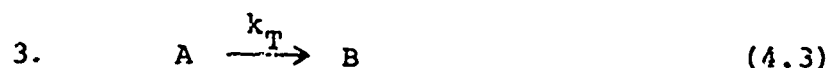
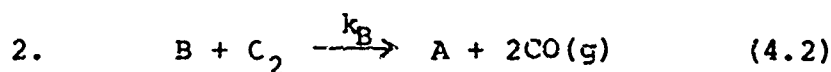
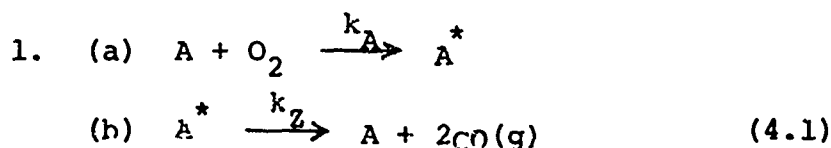
The reaction probabilities of O_2 at different target and beam temperatures are shown in Fig. 31 in the Arrhenius plot. It can be seen readily that the independent nature of the reaction probabilities with respect to beam temperatures extends over the entire target temperature range covered (1000° to 1700°K). This result should be expected in view of the arguments given previously. A typical set of reaction probabilities measured by Shih, using the same target material but with a nozzle beam source and an analog lock-in detection scheme, is included for comparison. It is satisfying to see that the results agree with those of the present case even though the incident beam flux of the two independent experiments differs by almost two orders of magnitude. Such a first order dependence of the reaction

rate on the incident pressure (implied by the constant reaction probability with varying incident flux) within the measured pressure range is quite reasonable in view of the low incident flux and the low reaction probabilities, which suggest that the low reaction probability is due to a surface reaction limited step rather than some other mechanisms such as gas-to-surface diffusion limited reaction. Olander et al found the same first order pressure dependence for the reaction probability in a comparable range of beam intensities. It should be pointed out that the results of Shih vary about 30-40% in absolute magnitude in comparison to a maximum of 15% fluctuations in the present case. The present, relatively consistent O_2 oxidation data is required to extrapolate, with confidence, the O_2 oxidation rate to higher beam temperatures for the interpretation of dissociated beam results (in spite of the fact that ϵ_{C_2} turns out to be independent of T_B in this case).

Fig. 31 also shows that the reaction probabilities do not display simple Arrhenius behavior (i.e., a constant activation energy represents by a constant slope in the Arrhenius plot) and exhibit a maximum at $T_T \approx 1350^\circ K$ regardless of beam temperatures. The existence of a maximum in reaction probabilities with varying target temperatures is perhaps the most consistent feature of various previous data for graphite oxidation involving both different forms of graphite and incident pressure levels. The present work, however, is probably the first to show such a behavior for

high temperature O_2 , since the previous experiments deal almost exclusively with room temperature oxygen. In general, it is the competition between generation of active sites by O_2 impingement and their deactivation by thermal annealing that results in the observed maximum in the reaction probability with varying target temperatures. Though previous results show a qualitative agreement for the shape of the reaction probability curve in an Arrhenius plot, the magnitude and location of the maximum reaction rate is frequently inconsistent even among graphites of the same type -- some examples were given in Chapter I in the review of past graphite oxidation investigations.

Perhaps the most widely accepted model for correlating the C- O_2 reaction rates at various O_2 pressures and carbon temperatures is the semiempirical, two-site model of Nagle and Strickland-Constable.³⁷ Without considering detailed surface mechanisms and nature of reaction sites, they arbitrarily classified the surface reaction sites into two groups: a more reactive A-site and a less reactive B-site. The surface reaction mechanisms are postulated as follows:



where A^* represents a surface complex,

A/B represents a more/less reactive site,

and k 's are the respective rate constants.

(4.1) provides the formation of a surface oxide complex and its subsequent desorption as CO , without a net generation or depletion of active sites. The apparent increase in reactivity with continuous impingement of O_2 on the surface is represented by the generation of A -sites from B -sites in (4.2). The deactivation of a surface due to thermal annealing is provided by (4.3). It is the competition between the last two processes that results in the observed maximum in the reaction probability with varying target temperatures. Though somewhat crude, the classification of the surface sites into two groups is not unreasonable physically. It is well documented that grain boundaries and lattice defect points such as vacancies, edge and screw dislocations are the more reactive sites for oxidation.⁴⁵

At steady state surface conditions, the Nagle and Strickland-Constable model results in a specific surface oxidation rate given by

$$\dot{w} = \left[\left(\frac{k_A p_{O_2}}{1 + k_Z p_{O_2}} \right) \chi + k_B p_{O_2} (1 - \chi) \right] \frac{\text{gm}}{\text{cm}^2 \text{-sec}} \quad (4.4)$$

$$\text{where } \chi = \left(1 + \frac{k_T}{k_B p_{O_2}} \right)^{-1} \quad (4.5)$$

= the fraction of A -sites on the surface.

The first and second terms in Eq. (4.4) represent the oxidation rates at A and B sites respectively. Nagle and Strickland-Constable then tried to correlate, and with some success, the available data of oxidation rates of pyrolytic graphite with the following set of rate constants:

$$\begin{aligned}
 k_A &= 20 \exp(-15,100/T) && \text{gm/cm}^2\text{-sec-atm} \\
 k_B &= 4.46 \times 10^{-3} \exp(-7,640/T) && \text{gm/cm}^2\text{-sec-atm} \\
 k_T &= 1.51 \times 10^5 \exp(-48,800/T) && \text{gm/cm}^2\text{-sec} \\
 \text{and } k_Z &= 21.3 \exp(2,060/T) && \text{atm}^{-1} \quad (4.6)
 \end{aligned}$$

Radcliffe and Appleton⁵⁸ are able to correlate more extensive soot and pyrolytic graphite oxidation data using the two-site model of Nagle and Strickland-Constable with the same parameters. In particular, agreement is good for an oxygen pressure range of 2.5×10^{-5} to 1.0 atm. Recently, Park and Appleton¹⁰¹ have measured the surface oxidation rates of soot in a shock-tube over the range of temperature 1700° - 4000°K and of pressure 0.05 - 13 atm of oxygen. Again, the results can be approximately correlated (within a factor of two) by the semi-empirical formula (Eq. (4.4)) proposed by Nagle and Strickland-Constable. Furthermore, surface temperatures above approximately 2800°K, the reaction rate tends to again increase, after reaching a local maximum at a lower temperature. This behavior is predicted in the two-site model, apparently due to an increase in reactivity of B-sites at high temperatures. In

Fig. 31, there is an apparent flattening of the reaction probability curve at temperatures above 1500°K that may indicate the possibility of an increase in reactivity with further rise in temperatures. Unfortunately, an increase in surface temperatures to above 1700°K is beyond the capabilities of the present experimental set-up. Clearly, it would be interesting to see whether such behavior actually takes place. Strickland-Constable's earlier work²⁶ in measuring the oxidation rates of graphite at O₂ pressure level of approximately 2.5×10^{-5} atm, however, does not show an increase in reactivity at high temperatures (> 2000°K) as predicted by the two-site model even though it fits quite well with the rest of his data, including the location of the maximum reactivity and its absolute magnitude. One other possibility that may lead to the apparent increase in reactivity observed by Park and Appleton¹⁰¹ is the direct sublimation of graphite, significant at temperatures above 3000°K⁴.

While the Nagle and Strickland-Constable model with their chosen rate constants seems to correlate quite well (within a factor of two) for high pressure measurements, substantial disagreements are present for the low pressure data. The semi-empirical formula tends to underestimate the reaction rates for O₂ pressure range of 10^{-7} to 10^{-9} atm by approximately two orders of magnitude. Furthermore, it no longer predicts the characteristic local maximum for

the reaction rate at $p_{O_2} \lesssim 10^{-8}$ atm, as shown by Shih.²⁹

This is in direct contradiction with the present results

($p_{O_2} \approx 10^{-9}$ atm) as well as with other low pressure

measurements, such as those of Olander et al²⁸ ($p_{O_2} \approx 10^{-7}$

atm), Shih ($p_{O_2} \approx 10^{-8}$ atm) and Duval²⁷ ($p_{O_2} \approx 10^{-6}$ atm),

which all show a local maximum in the reaction rate even

though different forms of carbon were used.

One may take the view that the apparent differences between the Nagle and Strickland-Constable predictions and the present available experimental results of low oxygen pressure may be attributed to the large number of parameters (eight in all -- one pre-exponential factor and one activation energy for each of the four rate constants) that were originally chosen to fit principally the Strickland-Constable data. Obviously, such a set of parameters may not be the optimum for correlating results that vary over ten orders of magnitude in oxygen pressure levels. Furthermore, recent results of Park and Appleton¹⁰¹ at relatively high pressures ($0.05 \text{ atm} < p_{O_2} < 13 \text{ atm}$) indicate that the Nagle and Strickland-Constable formula also tends to underestimate the oxidation rates at high temperatures (i.e., $T_T \geq 2200^\circ\text{K}$). However, in view of the current lack in fundamental understanding of the surface oxidation mechanism, an attempt to adjust the parameters in order to obtain a better fit for all the experimental results will not be made here.

On the other hand, one may agree that though the Nagle and Strickland-Constable formulation of the oxidation reaction is basically sound, as proved by the experiments (such as those of Shin and Olander et al) of thermal annealing and oxidation-induced generation of active sites, it nevertheless neglects the detailed dynamics of the surface processes. In spite of the fact that the formulation does provide a fractional order dependence of \dot{w} on p_{O_2} (as shown by the first term in Eq. (4.4), which arises because the degree of coverage of the A-sites by surface oxides increases with increasing oxygen pressure in accordance with the Langmuir isotherm), which was experimentally confirmed¹⁰¹ by the changing of the reaction order from first to zeroth as the oxygen pressure was increased, at low pressures a somewhat more detailed account of the surface processes (such as oxygen dissociation-recombination, migration and diffusion) may be necessary. The success of the Nagle and Strickland-Constable model in fact may be due to the relatively fast reaction rates, especially in cases of high pressure levels, which tend to mask whatever surface phenomena that may take place in a time scale τ_t compared to the experimental observation time. However, at low pressure levels, surface processes are all, if not equally, important and a correct prediction of the oxidation rate should require that account

be taken of all such surface phenomena. Since the Nagle and Strickland-Constable model does not consider any detailed reaction mechanisms, any prediction of the oxidation rate in such a low pressure regime may well be expected to be in error.

It is impossible to formulate a detailed reaction model from the present measurements of steady state oxidation rates. For such a purpose, it may be helpful if the incident beam chopping scheme of Olander et al²⁸ is incorporated into the design, in which case information such as residence time may be obtained. However, the resulting experimental complexities and corresponding reduction in signal levels may be prohibitive in practice. In the present case, the two-site model of Nagle and Strickland-Constable seems to be adequate to explaining most of the observed phenomena as well as illustrating some of the major differences between O and O₂ oxidation as will be discussed in the next section.

F. C-O Reaction

1. Reaction Probability

The reaction probability of O at different target temperature is shown in Fig. 32 in an Arrhenius plot. The corresponding O₂ reaction probability is included for comparison. The O oxidation rate was inferred by subtracting the CO signal due to O₂ from the CO flux measured for a dissociated beam with an O-to-O₂ flux ratio of approximately

one-to-three. An average maximum O_2 reaction probability of 1.6×10^{-2} was used for this purpose and the waiting period after each target temperature change was identical to that described in the previous section for the measurement of the $C-O_2$ reaction probability.

Some distinct features of the O reaction probability are apparent in Fig. 32. First and foremost is the fact that ϵ_O is more than an order of magnitude higher than ϵ_{O_2} at corresponding target temperatures. The ratio of ϵ_O to ϵ_{O_2} varies from a high of approximately 37 at $T_T = 1000^\circ K$ to a low of approximately 16 at $T_T = 1350^\circ K$ within the target temperature range of 1000° to $1700^\circ K$. The O reaction probability also exhibits a non-Arrhenius behavior (i.e., a variable slope in the Arrhenius plot, implying a variable activation energy) with the maximum reactivity at $T_T \approx 1400^\circ K$, which is within $50^\circ K$ of the target temperature for maximum O_2 reactivity. However, it is reasonable to state that the O and O_2 reactivities peak at a common target temperature within the experimental accuracy. The slope of the ϵ_O curve is also less steep than that of ϵ_{O_2} , implying that the O reaction probability is only slightly target temperature dependent. In fact, within the target temperature range, ϵ_O varies by only 45% as compared to 75% for ϵ_{O_2} .

In order to test the reliability of the data reduction scheme and to ensure the consistency of the measured data

(in particular, the high absolute value of the O reaction probability, which at the maximum case corresponds to more than one reacting O-atom for every four such incident particles), the reaction probability of O was obtained for different source conditions that represent different O-to-O₂ flux ratios and total incident pressures. Table IV-2 shows the measured ϵ_O for different incident beam and target conditions.

Table IV-2

Reaction Probabilities of O at Different
Source and Target Conditions

<u>p_s (torr)</u>	<u>T_s (°K)</u>	<u>F_O/F_{O₂}</u>	<u>T_T (°K)</u>	<u>ε_O/ε_{O₂}</u>	<u>ε_O</u>
0.10	2220	0.49	1355	20.1	0.32
0.20	2205	0.31	1300	16.4	0.26
0.24	2200	0.27	1390	14.6	0.24
0.26	2110	0.14	1380	15.7	0.25

An average value of $\epsilon_{O_2} = 1.6 \times 10^{-2}$ was used in calculating the ϵ_O -to- ϵ_{O_2} ratio in column 5 and the target temperatures are all within a range of $\pm 50^\circ\text{K}$ of the most reactive target temperature (i.e., 1350°K). No attempt is made to account for the difference in ϵ_{O_2} in view of the same small target temperature range in question. It can be seen that the measured O reaction probability is reasonably repeatable (within a maximum fluctuation level of 25%) by beams of

different compositions (which vary from an O-to-O₂ flux ratio of 0.14 to 0.49) and flux levels (which cover a 2 1/2-fold range in magnitude). The apparent higher reaction probability at $p_s = 0.10$ torr ($\epsilon_o = 0.32$ as compared to an average ϵ_o of 0.25 for the rest of the data) may lead to the suggestion that ϵ_o is pressure dependent. However, a closer examination reveals that the O flux levels in all experimental runs are comparable (e.g., the O intensity at $p_s = 0.10$ torr is within 25% variation of all the remaining O intensities), thereby eliminating such a possibility. For establishing the pressure dependence of a reaction probability, a variation of at least one order of magnitude of the pressure level is desirable. Furthermore, in view of the low pressure level in the experiment (which means a low surface coverage, as there are approximately 100 surface carbon atoms for every incident oxygen particle), a first order pressure dependence of the carbon atoms removal rate is likely. The variations of ϵ_o may be attributed to the experimental accuracy, which shows a 25% fluctuation level as compared to 15% for ϵ_{O_2} . Nevertheless, the results clearly establish the fact that O is much more reactive (by more than ten times) than O₂ at the corresponding target temperature.

To the best of the author's knowledge, the only other available data for high temperature oxidation of graphite by dissociated oxygen is that of Rosner and Allendorf.^{3,10}

Using a microwave discharge tube for generating dissociated oxygen and calibrating the O-atom concentrations in the vicinity of the graphite by a NO_2 light titration technique, Rosner and Allendorf measured the oxidation rates of both pyrolytic and isotropic graphite in a gas flow system. The graphite, in the form of a circular filament and heated resistively, was placed in the gas stream and the reaction rate was calculated from microscopic determinations of the reduction in filament diameter after known exposure times. A typical total test section pressure of 1 torr was maintained and oxygen diffusional limitations were apparently ruled out on the basis of the absence of effects of flow rate and carrier gas identity on the observed reaction rates. No reaction products were monitored.

The reaction probabilities for isotropic graphite measured by Rosner and Allendorf together with the present results are shown in Fig. 33. Apart from the absolute magnitude and the location of the maximum reactivity, the essential features of the two findings are surprisingly similar in view of the completely different experimental techniques and oxygen pressure levels (which vary by almost five orders of magnitude). The common features are:

- (1) O is much more reactive than O_2 (by approximately one order of magnitude) at corresponding target temperatures;
- (2) neither O nor O_2 exhibits simple Arrhenius behavior with the reaction probabilities of both O and O_2 peak at

a common target temperature within the temperature range; (3) the surface temperature dependence of the oxidation probabilities by O is much less pronounced than that by O₂. The difference in reaction probability magnitude may be attributed to the different kinds of graphite used in the two experiments -- the more porous (and hence more surface area and grain boundaries) graphite used by Rosner and Allendorf, with a density of 1.73 gm/cm³ as compared to the present graphite density of 1.79 gm/cm³, may account for its higher reactivity. The same explanation may be valid for the difference in maximum reactivity location, since such peak behavior is presumably due to the competitive processes of thermal annealing and oxidation-induced generation of active sites and the equilibrium point for the two processes definitely depends on the kind of surface structures. The reaction probability of Rosner and Allendorf was also found to be higher than predicted by the Nagle and Strickland-Constable model at the corresponding pressure level.⁵⁸ Nevertheless, Fig. 33 clearly establishes the consistency of some dominant features of the C-O and C-O₂ reactions that may lead to an understanding of the reaction mechanisms.

While detailed reaction mechanism propositions are certainly premature based on the preceding data, the large absolute value of the reaction probability and its weak target temperature dependence strongly suggest that O-oxidation takes place along a different path than does

O_2 -oxidation. Since CO is the dominant product for both O and O_2 oxidation, it can be suggested that while the reaction rate of O_2 is limited by the surface migration and dissociative adsorption processes, the O-oxidation occurs via a Rideal-type mechanism in which direct O-atom strikes from the gas phase lead to formation and desorption of product molecules, and no migration along the surface to reaction sites is necessary. To test such a view, the so-called "hysteresis" behavior of the reaction probability in regard to thermal annealing of the target has been investigated, as will be described in the following section. Rosner and Allendorf also suggested that the surface structure may have a minor effect on the O reaction probability -- a fact that they proved by showing the relatively constant O reaction probability for both pyrolytic and isotropic graphite. However, their postulation of the C-O reaction mechanism in which a gaseous O-atom impacts upon an adsorbed O-atom leading to the formation and desorption of a CO_2 molecule may be in error, since no CO_2 is observed as the reaction product in this case.

2. Hysteresis Behavior

To further investigate the influence of the surface conditions in regard to the reaction rates, a series of experiments has been carried out in which the thermal annealing of the surface is known to influence the O_2 reaction

probability. The results are presented in Fig. 34, in which the ordinate is not the reaction probability but a normalized CO signal flux from the target for O and O₂ separately instead. This is done simply to present a clearer picture and to give a common datum point for comparing the O and O₂ results.

The sequence of data taking is important in interpreting the respective curves in Fig. 34. Firstly, the O₂ curve was obtained using pure O₂ at a beam temperature of 1875°K. Starting at a low surface temperature of 1000°K, T_T was increased at 100°K intervals, after each data point, to a maximum temperature of 1700°K. T_T was then decreased to 1100°K at 150°K intervals. The waiting periods between points for the increasing target temperature sequence are similar to the ones used for obtaining steady state O₂ reaction probability, as discussed in Section IV-D; namely, 30 minutes for 1000°K < T_T < 1300°K and 1 hour for T_T > 1300°K. On decreasing T_T from 1700° to 1100°K, a waiting period of also 1 hour was used between points. A similar experimental procedure was carried out for the case of a dissociated oxygen beam. The data reduction for the O results is standard except when dealing with the decreasing target temperature regime -- the CO signal due to O₂ that is subtracted out from the combined signal for a dissociated beam is based on the previously measured O₂ signal for a decreasing target temperature regime rather than the steady

state O_2 signal. This ensured that the CO signal due to O_2 in a dissociated beam is accounted for under identical conditions for a pure O_2 beam.

It is interesting to see in Fig. 34 that on decreasing the target temperature from 1700°K, the CO signals (equivalently, the reaction probabilities) due to both O and O_2 do not return to their previous values at the corresponding target temperatures; instead, both show a decrease in magnitude. This "hysteresis-like" behavior, upon cycling target temperatures, has been witnessed previously by Shih,²⁹ Olander²⁸ and Duval,²⁷ all using molecular oxygen; however, this is the first time that O has been shown to exhibit a similar behavior. Such behavior can be explained along the two-site model of Nagle and Strickland-Constable. At high surface temperatures, thermal annealing of the active surface sites takes place. When the target temperature is lowered, the annealed active sites require a finite time for them to be regenerated by oxygen bombardment. If the reaction probability is measured at a time when the surface is still undergoing adjustment, then the measured ϵ will invariably be smaller than the steady state value. While one hour seems to be sufficient as the adjustment time for the increasing temperature sequence, it appears to be inadequate for the decreasing temperature direction, as shown by the decrease in ϵ , possibly due to the concomitant reduced oxidation (therefore

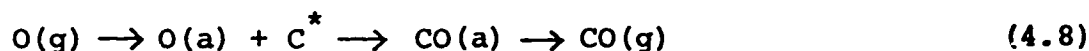
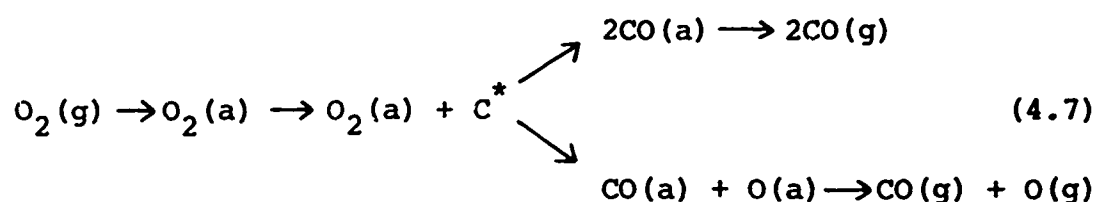
site regenerating) rates. The readjustment time, of course, depends on the type of graphite and the degree of surface annealing which is highly temperature dependent, as shown by the decrease in ϵ at high surface temperatures. For the present isotropic graphite, a readjustment time of several hours is required to reach steady state at $T_T \approx 1300^\circ\text{K}$ after previously annealing the surface at $T_T = 1700^\circ\text{K}$, as shown by Shih.

While an apparent hysteresis exists for both O and O₂, a difference in the degree or extent is definitely noticeable for the two. For example, at a target temperature of 1300°K , ϵ_O comes back to within 80-85% of the stationary state value before annealing as compared to only approximately 20% for ϵ_{O_2} . The significance of this result is either or both of two possibilities: (1) the surface structure has a relatively minor effect on the O reaction probability; (2) the regeneration rate of active sites for O is much faster than that for O₂. Most likely both of these possibilities contribute in view of the much less pronounced dependence on surface temperature as well as the higher absolute value for ϵ_O .

3. Reaction Mechanism

Though an understanding of the graphite oxidation mechanism is far from complete, the results in this experiment nonetheless provide enough information for the postulation, at least qualitatively, of a plausible reaction model.

The processes for C-O₂ and C-O reactions are summarized in the following mechanisms respectively:



where (g) denotes the gaseous state

(a) denotes the adsorbed state

and C^{*} denotes an active carbon site.

For a C-O₂ reaction, the first step is O₂ adsorption, which is followed by surface migration to an active site. O₂ then dissociates to form either two adsorbed CO or one adsorbed CO and one adsorbed O. The adsorbed particles are all subsequently desorbed. This mechanism is essentially similar to that proposed by Olander et al.²⁸ with the exception that the adsorbed O-atom formed by O₂ dissociation either desorbs or reacts to form another CO without further surface migration. The surface migration of the adsorbed O-atom to another reactive site is the mechanism proposed by Olander et al. This step is unlikely in view of the high reaction probability of O and its relative independence on both target temperature and structure. Since O₂ tends to dissociate and react around

active sites (a fact shown by electron microscopy studies^{40,45}), the most probable process will be the formation and desorption of two CO molecules at the same point, as represented by the upper branch mechanism in (4.7). The lower branch mechanism of (4.7) is possible but probably accounts for only a small fraction of the adsorbed O₂, again due to the high reaction probability of an adsorbed O-atom. Unfortunately, whether such a mechanism takes place or not cannot be verified experimentally, since the desorbed O signal, if any, will be buried in the huge O (or m/q = 16) signal from the cracking pattern of the surface scattered O₂ molecules. CO₂ formation has not been considered, since it was found to be experimentally insignificant, thereby leading to the present postulation of O₂ adsorption, migration and dissociative reaction mechanisms. The role of the active carbon sites, C^{*}, can be explained along the two-site model of Nagle and Strickland-Constable.³⁷ In this model, all surface sites can be considered as possible reactive sites with the only distinction of an associated degree of reactivity -- in particular, they are classified into two types: the more reactive A-site and the less reactive B-site. The balance of A and B sites is considered in Section IV-D and will not be repeated here.

A Rideal-type mechanism in which a reaction readily takes place after the adsorption of an O-atom is proposed for the C-O reaction, as shown in (4.8). The absence of a dissociation process probably accounts for the high O reaction probability and its relatively independent nature on surface structure. The proposed mechanism is in disagreement with that suggested by Rosner and Allendorf^{3,10} in which the high reaction probability of O is attributed to the direct impingement of O(g) on O(a) that leads to the formation and desorption of CO₂. The high O reaction probability can also be attributed, in part, to the increased sticking probability of O than O₂, as shown by its lower activation energy (at surface temperatures below approximately 1300°K, the O and O₂ data can be represented by straight lines with corresponding local activation energies of about 7 kcal/mole and 36 kcal/mole respectively). As to the question of what constitutes an active site, C*, the same classification of surface sites for O₂ can be applied here with a modification only in the reactivity, namely

$$\text{A-sites: } \epsilon_{\text{O}} \approx 1, \epsilon_{\text{O}_2} \lesssim 1$$

$$\text{B-sites: } \epsilon_{\text{O}} < 1 \approx 0.2-0.3, \epsilon_{\text{O}_2} \ll 1.$$

In general, all surface atoms are fairly reactive for O as shown by the high reaction probability. This could account for the absence of a surface migration process in

the proposed C-O reaction mechanisms in (4.8). The suggestion of two types of surface sites for O-oxidation is reasonable in view of the observed local maximum in reaction probability and the hysteresis behavior upon surface annealing (both of which are fairly well explained by the two-site model). This classification of surface sites is further supported by studies of the surface structures after exposing single-crystal graphite to streams of dissociated oxygen.⁴⁵ Using electron microscopy, it has been shown that while O₂-oxidation forms distinctive hexagonal pits at crystal defect points, O-oxidation generally creates a background of conical pits over the entire basal plane with a higher concentration of pits along grain boundaries. The implication of this result is that while O-oxidation does not necessarily initiate at crystal defect points, it tends to have a higher reaction probability at such points.

CHAPTER V

CONCLUSIONS AND SUGGESTED FUTURE WORK

A. Conclusions

CC has been observed as the primary reaction product for both C-O and C-O₂ reactions (C being isotropic graphite in this case) within the target temperature range of 1000° to 1700°K and a beam pressure of about 2×10^{-7} torr. No CO₂ was observed by either a phase sensitive detection technique or monitoring of the background CO₂ peak. Both CO and CO₂ have been observed by previous investigators as products of graphite oxidation; however, as the target temperature is increased to above 1200°K, the ratio of CO to CO₂ is drastically increased, especially for experiments in the low pressure range.^{28,29} CO₂ detection from previous experiments can be partially explained by the presence of gas-gas collisions, where CO in the gas phase is oxidized to CO₂ by the background O₂. Such a mechanism is clearly ruled out in the present experiment, where the background pressure is approximately 10^{-8} to 10^{-9} torr.

Both O and O₂ reaction probabilities exhibit non-Arrhenius behavior and show a local maximum in the target temperature range. A qualitative explanation of such a behavior can be presented along the lines of the two-site model of Nagle and Strickland-Constable,³⁷ though their

suggested parameters for the various rate constants do not seem to fit available data in the low pressure range. It is the competition between generation of active sites by oxygen impingement and their deactivation by thermal annealing that results in the observed maximum in the reaction probability with varying target temperatures. Physically, the more active surface sites are grain boundaries and lattice defect points, such as vacancies, edge and screw dislocations.

The reaction probability of O is more than an order of magnitude higher than that of O₂, reaching a maximum of almost 0.3 at a target temperature of about 1350°K. It is also weakly target temperature dependent. The large absolute value of the reaction probability and its weak temperature dependence strongly suggest that O-oxidation takes place along a different path than does O₂-oxidation. Since CO is the dominant product for both O and O₂ oxidation, it is proposed that while the reaction rate of O₂ is limited by the adsorption, surface migration and dissociation processes, the O-oxidation occurs via a Rideal-type mechanism in which the surface adsorption of an O-atom from the gas phase leads directly to the formation and desorption of a product molecule, and no migration along the surface to a defect point is necessary. This view is further supported by a surface annealing experiment in which it was found that while annealing at high temperature

(1700°K) apparently reduces the O_2 reaction probability subsequently measured by virtue of a reduction of the defect points in the graphite, it simultaneously has a minimal effect on the O reaction rate. Recent observation by McCarroll and McKee⁶⁴ using electron microscopy techniques indicates that while O_2 attacks graphite at lattice defect points, O produces a general background of conical pits in the surface -- a result that also lends credence to the suggested reaction mechanisms.

While not surprising, it is disappointing to find that the reaction probability of O_2 does not vary as functions of beam temperature (300°K to 1875°K) and angle of incidence (45° to 60°) within the accuracy of the experiment. This behavior can be attributed partly to the rough and uncharacteristic surface of the graphite being used in this experiment. If a molecule made several collisions with a roughened surface before reacting or being re-emitted, then the oxygen would be preheated to the target temperature regardless of the incident beam temperature and a beam heating experiment would be inconclusive. Similar arguments hold for the insensitivity of the reaction probability as regard to angle of incidence. The roughness of the surface is also confirmed by the measured re-emitted oxygen flux distribution, which is a diffuse pattern regardless of beam and target temperatures as well as angle of incidence.

The flux distribution of CO off the target is surprisingly lobular in the normal direction and can be fitted quite closely by a cosine square distribution independent of target and beam temperatures and incident angle. Lobular desorption patterns have been observed for H_2 and D_2 desorbed from metal surfaces^{96,98} and although Van Willigen⁹⁶ suggested that the activated-adsorption model of Leonard-Jones may be used as the basis for developing an approximate model of the desorption process, actual agreement between the observation and theory was fair. It is questionable whether Van Willigen's model can be applied in our case and clearly additional studies must be made before an understanding of such a desorption phenomenon can be expected.

B. Suggested Future Work

Though a great deal of information has been learned about graphite oxidation recently, the reaction mechanisms are far from fully understood. There are still apparently contradictory results (and hence different conclusions) obtained by various investigators using different experimental techniques.¹³ Some of the discrepancies may no doubt be attributed to the complexities of the oxidation processes, but much may be due to the vastly different crystalline structures of the carbon samples used by different investigators. The present isotropic graphite target may not be the ideal material for investigating the

importance (or irrelevance) of some experimental parameters for the oxidation reaction due to its macroscopic roughness as well as its uncharacteristic crystalline structure. For example, whether the gas energy and momentum have any effect on the reaction probability is still open to questions. One way to clarify such problems is to use single-crystal (limited by available size, however) or pyrolytic graphite for better surface characterization. This approach may also serve as a more consistent basis for comparison of results among various work. One must be cautioned that continuous monitoring of the surface structure may be necessary, since the surface condition of a sample is liable to change as the experiment is carried on.

The primarily steady state measurements of the present experiment fail to obtain the rate constants of such processes as thermal annealing and oxidation-induced surface reactivation. Transient studies under various surface conditions, such as those performed by Shih,²⁹ may be helpful in estimating some of the rate constants. In addition, the incident beam chopping scheme of Olander et al²⁸ is particularly promising in correlating results with proposed mechanisms. These approaches, however, are plagued by the ever-present problem of low signal-to-noise ratio, especially in the present case of a relatively low incident beam flux for dissociated oxygen.

Time-of-flight technique may be used to measure the velocity distributions of the surface re-emitted particles. The resulting measured thermal accommodation coefficients and momenta transfer efficiencies may further elucidate surface roughness effects in regard to the reaction rate. The velocity distributions of the desorbed reaction products may be revealing in understanding the lobular desorption patterns measured in this experiment.

APPENDIX A

Target-Detector Geometry

Due to both the finite size of target and detector and the relatively short distance between them, the target can no longer be considered as a point source for the measurements of the spatial distributions of the re-emitted particles. The flux measurement as a function of the detector angle (measured from the target normal) requires a correction that arises from a non-uniform flux across the chopper collimator, resulting from purely geometrical effects as well as non-uniform incident beam flux on the target. Since the incident beam intensity is, for all practical purposes, uniform across the whole target (which subtends a source angle of less than 6°), as can be seen in Fig. 24, no correction is necessary for non-uniform incident flux in this case. Corrections due to geometrical effects are necessary when the detector view includes either one or both target edges, which results in deficiencies in the chopper collimator flux when compared with that of an infinite target. The corrections for the exact present target-detector geometry with the identical chopper have been considered in Ref. 29 and what follows will be a summary of the steps to arrive at the theoretical distribution

curves, as shown in the figures for the angular distributions of the scattered or reaction product particles from the target.

Fig. 35 shows a schematic diagram of the target-detector geometry, which is taken directly from Ref. 29. The notation is quite self-explanatory except perhaps the following: X_e is the point in the chopper collimator where the detector first sees a target edge; $\Delta\theta_m$ is the lateral angle measured from the target edge, over which there is no flux contribution to the chopper collimator and results in a maximum flux deficiency at the edge, i.e. $X = 0$; θ_0 is the angle subtended by the detector at any point in the collimator and is independent of X for $d_1 \ll l_1$. All these parameters have expressions given in Ref. 66 on which the analysis is originally based.

When the detector is rotated about the target normal, it begins to see target edges which results in a deficiency in the detected flux when compared with that of an infinite target. The deficiency terms are given by²⁹

$$\frac{F}{F_0} = \begin{cases} 1 - \frac{\Delta\theta_m}{\theta_0} \left(\frac{X_e - X}{X_e} \right) & , X < (d_1 - X_e) \\ 1 - \frac{\Delta\theta_m}{\theta_0} \left(\frac{2X_e - d_1}{X_e} \right) & , (d_1 - X_e) < X < X_e \\ 1 - \frac{\Delta\theta_m}{\theta_0} \left(\frac{X - d_1 + X_e}{X_e} \right) & , X_e < X < d_1 \end{cases} \quad (A.1)$$

where F/F_0 is the chopper collimator flux per unit chopper collimator width divided by the infinite target value. The effective shutter function, $A(\theta_r)$, that accounts for the flux deficiency due to the target-detector geometry for the present half sine wave shutter function of the tuning fork has been evaluated in Ref. 29; this is done by weighting the half sine wave function (which corresponds to an effective shutter function for an infinite target) by Eq. (A.1) and integrating over the entire shutter period. Such a procedure will not be repeated here and the reader is referred to Ref. 29.

The theoretical curves for the detected signal for given flux distributions can now be calculated. If $F_0(\theta_r)$ is the angular flux distribution per unit target area for an infinite target, then the detected flux by a fixed size detector (as in the case of the mass spectrometer ionizer) is $\sim F_0(\theta_1)/\cos \theta_r$ since the area of the target seen by the detector is $\sim 1/\cos \theta_r$. For the case of a finite target, the actual detected flux, $D(\theta_r)$, would be less due to target edge effects and the reduction in signal level is proportional to the ratio of the areas of the effective shutter function, $A(\theta_r)$ and the true shutter function, A_0 , which is simply the area of the half sine wave in this case, resulting in

$$D(\theta_r) \sim \frac{F_o(\theta_r)}{\cos \theta_r} \cdot \frac{A(\theta_r)}{A_o} \quad (A.2)$$

If the emitted flux is diffuse, i.e., $F(\theta_r) \sim \cos \theta_r$, then $D(\theta_r) \sim A(\theta_r)/A_o$. This is the curve that is plotted in, for example, Fig. 26 as the cosine distribution curve. As can be seen, for small θ_r , $D(\theta_r)$ is constant since $A(\theta_r)/A_o$ is unity as no target edge corrections are necessary. Only when the detector begins to see target edges does the curve begin to depart from the infinite target curve, which in the diffuse emission case is simply a constant line.

In general, if $F_o(\theta_r) \sim \cos^n \theta_r$, i.e., the flux emits in a lobular manner, then

$$D(\theta_r) \sim \cos^{n-1} \theta_r \cdot \frac{A(\theta_r)}{A_o} \quad (A.3)$$

The case for $n = 2$ has been plotted, for example, in Fig. 29 for comparison with detected data.

APPENDIX B

Pumping Speed Measurements

The pumping speeds of the diffusion pumps as installed in the vacuum system were measured. This was necessary because the manufacturers' supplied values are for those of an unbaffled system.

Gas at atmospheric pressure was trapped in a graduated burette immersed in an open glass beaker containing D.C. 704 oil (vapor pressure of D.C. 704 at room temperature is approximately 10^{-8} torr). The gas in the burette was leaked into the vacuum chamber through a small adjustable leak valve with the gas supply pressure at almost constant pressure (atmospheric) since the rise in oil column in the burette due to the gas evacuation was always kept to be less than 5 cm as compared to 8.6 meters of oil for one atmosphere. From a measurement of both the time for a given volume of gas to leak into the chamber and the resulting rise in chamber pressure, one can obtain the pumping speed, \dot{V} , in liters/sec from

$$\dot{V} = \frac{P_s \Delta v}{t \Delta p_c} \quad (B.1)$$

where p_s = gas supply pressure in torr
 Δv = volume of gas evacuated in liters
 t = time of evacuation in sec
 Δp_c = change of chamber pressure in torr

Different gases were used for the calibration of the test chamber 16" diffusion pump and only O_2 was used for the source chamber 6" booster pump. The results of the calibrations are shown in Table B-1.

Table B-1
Pumping Speeds of the Diffusion Pumps

<u>Pump</u>	<u>Gas</u>	<u>\dot{V} (liters/sec)</u>	<u>\dot{V}/\dot{V}_{O_2}</u>	<u>(m_{O_2}/m)</u>
16" dia. (Test Chamber)	O_2	1730	1.00	1.00
	CO	1955	1.13	1.07
	CO_2	1510	0.87	0.85
6" dia. (Source Chamber)	O_2	380		

Under free-molecule-flow conditions in the vacuum chamber as in the present case, the pumping speeds for different gases vary as the inverse of the square root of the gas molecular weight. This result is confirmed by comparing the last two columns in the table.

APPENDIX C

Ion Gauge and Mass Spectrometer Calibrations

The two ion gauges (GE hot filament miniature ionization gauges) that were used to measure test and source chamber pressures respectively were calibrated by means of a Knudsen flow method and the results checked independently by a McLeod gauge. A small chamber, approximately 6" x 4" diameter, was mounted on the side of the test chamber from which it was separated by a thin stainless steel plate with a 3/4" diameter orifice. An adjustable leak system with a measurable flow rate, similar to that used for the pumping speed measurements, was connected to the small chamber with its pressure monitored by the ion gauge to be calibrated. The pressure in the small chamber, under Knudsen flow conditions, is given by

$$p = \frac{F}{A} \sqrt{2\pi mkT} \quad (C.1)$$

where A is the orifice area and F is the total flux out of the orifice which in steady state conditions is equal to the flow rate measured by the gas supply system. The measured gauge sensitivities, $S_i = i_i / (p_i i_e)$, for different gases are shown in Table C-1.

Table C-1

Ion Gauge Sensitivities for Different Gases

<u>Gas</u>	<u>S_i (Torr)⁻¹</u>	<u>S_i/S_{N_2}</u>
N ₂	1.88	1.00
O ₂	1.54	0.82
CO	1.87	0.99
CO ₂	2.06	1.09

The gauge sensitivity for N₂ was further checked by a liquid nitrogen trapped McLeod gauge which showed an agreement to within 10% of the measured chamber pressure for a pressure range of 3×10^{-6} to 10^{-4} torr. The calibrated ion gauge was used for subsequent calibration of the mass spectrometer.

The mass spectrometer sensitivities for different gases were calibrated by leaking the gases into the test chamber through the beam source with the test chamber pressure monitored by the calibrated ion gauge. The ionizer electron emission current, electron accelerating voltage and the electron multiplier voltage were set at 1 ma, 70 volts and 2750 volts respectively, whereas the ion draw-out and deflection plates 1 and 2 were set nominally at 5.6, 3.2 and 5.3 units respectively, which correspond to

a maximum output signal for N_2 ($\frac{m}{q} = 28$). These mass spectrometer settings were kept constant throughout the experiment to provide a consistent basis for comparing the various signal levels and they were maximized on only the N_2 peak since 28 is about the medium mass number for all the gases of interest in this experiment. Table C-2 shows the mass spectrometer sensitivities of the different gases in terms of S_{ms}^i as defined in Eq. (2.20). The units for S_{ms}^i are pulses/sec-amp-torr.

Table C-2

Mass Spectrometer Sensitivities for Different Gases

<u>Gas</u>	<u>m/q</u>	<u>$S_{ms}^i (10^{15})$</u>	<u>$S_{ms}^i / (S_{ms}^i)_{N_2}$</u>
N_2	28	2.05	1.00
O_2	32	1.72	0.84
CO	28	2.26	1.10
CO_2	44	1.56	0.76

Ionization of the gaseous molecules by electron bombardment also results in a dissociation of the molecule into different components. The resulting "cracking pattern" of each gas of interest in this experiment is tabulated in Table C-3; the cracking pattern is shown by the ratio of

the component signal level, S_i , to that of the parent gas signal level, S .

Table C-3

Mass Spectrometer Cracking Patterns for Different Gases

<u>Parent Gas</u>	<u>S_C/S</u>	<u>S_N/S</u>	<u>S_O/S</u>	<u>S_{CO}/S</u>
O_2			0.087	
CO	0.032		0.016	
CO_2	0.030		0.091	0.076
N_2		0.067		

REFERENCES

1. Mantell, C.L., Carbon and Graphite Handbook, Interscience Publishers, N.Y. (1968).
2. Schiff, D., "Pyrolytic Materials for Re-entry Applications," Metals Engineering Quarterly (ASM), 2, 32-42 (1962).
3. Rosner, D.E. and Allendorf, H.D., "High Temperature Kinetics of Graphite Oxidation by Dissociated Oxygen," AIAA Journal, 3, 8 (1965).
4. Scala, S.M. and Gilbert, L.M., "The Sublimation of Graphite at Hypersonic Speeds," General Electric, R64SD55, (Aug. 1964).
5. Byram, E.T., Chubb, T.A. and Friedman, H., "Dissociation of Oxygen in the Upper Atmosphere," Phys. Rev., 98, 1594 (1955).
6. Laider, K.J., Chemical Kinetics, Second Edition, McGraw-Hill, (1965).
7. Scala, S.M. and Gilbert, L.M., "Aerothermochemical Behaviour of Graphite at Elevated Temperatures," General Electric, R63SD89, (Nov. 1963).
8. Blyholder, G. and Eyring, H.J., "Kinetics of Graphite Oxidation," J. Chem. Phys., 61, 682 (1957).
9. Horton, W.S., "Oxidation Kinetics of Pyrolytic Graphite," General Electric, 60GL218, (Jan. 1961).

10. Rosner, D.E. and Allendorf, H.D., "Comparative Studies of the Attack of Pyrolytic and Isotropic Graphite by Atomic and Molecular Oxygen at High Temperatures," AIAA Journal, 6, 4, 650 (1968).
11. Blackwood, J.E., "The Gasification of Carbon," Rev. Pure App. Chem., 4, 4, 251 (1954).
12. Walker, P.L., Jr., Rusinko, F., Jr. and Austin, L.G., "Gas Reactions of Carbon," Adv. Catalysis, 11, 133 (1969).
13. Thomas, J.M., "Reactivity of Carbon: Some Current Problems and Trends," Carbon, 8, 413 (1970).
14. Smith, R.A., Proc. Roy. Soc. (London), 12, 425 (1863).
15. Rhead, T.F.E. and Wheeler, R.V., J. Chem. Soc., 103, 461 (1912).
16. Lowry, H.H. and Hulett, G.A., J. Am. Chem. Soc., 42, 1408 (1920).
17. Langmuir, I., "The Gasification of Carbon," Rev. Pure Appl. Chem., 4, 4, 251 (1954).
18. Lambert, J.D., Trans. Faraday Soc., 32, 249 (1931).
19. Bartell, F.E. and Miller, E.J., J. Phys. Chem., 28, 992 (1924).
20. Shah, M.S., "The Combustion of Charcoal in Oxygen, Nitric Oxide and Nitrous Oxide. Part I: The Adsorption of Oxygen," J. Chem. Soc., 2661, 2676 (1929).

21. Chukhanov, Z.F. and Karzhavina, N.A., J. Tech. Phys. (U.S.S.R.), 9, 1932 (1939); 10, 1256 (1940).
22. Tsukhanova, O.A., J. Tech. Phys. (U.S.S.R.), 5, 41 (1938).
23. Meyer, L., Trans. Faraday Soc., 34, 1056 (1938).
24. Mayers, M.A., "The Combustion of Carbon," Chem. Reviews, 14, 31 (1934).
25. Kuchta, J.M., Kant, A. and Damon, G.H., Abstract Papers, Am. Chem. Soc., 120th Meeting, New York, N.Y. (1951).
26. Strickland-Constable, R.F., "The Interaction of Oxygen and Carbon Filaments at High Temperatures," Trans. Faraday Soc., 40, 333 (1944).
27. Duval, X., J. de Chimie Physique, 47, 339 (1950).
28. Olander, D.R., Siekhaus, W., Jones, R. and Schwartz, J.A., "Reactions of Modulated Molecular Beams with Pyrolytic Graphite. I. Oxidation of the Basal Plane. II. Oxidation of the Prism Plane," J. Chem. Phys., 57, 1 (1972).
29. Shih, W.C.C., "Molecular Beam Studies of Graphite Oxidation," M.I.T. Ph.D. Thesis (1973).
30. Van Loon, W. and Smeets, H.H., Fuel, 29, 119 (1950).
31. Meyer, L., J. de Chimie Physique, 47, 328 (1950).
32. Scott, G.S. and Jones, G.W., U.S. Bureau Mines Repts. Invest. 3405 (1938).
33. Gulbransen, E.A. and Andrew, R.F., Ind. Eng. Chem.,

- 44, 1034 (1952).
34. Loebenstein, W.V. and Deitz, V.R., J. Phys. Chem.,
59, 481 (1955).
35. Bonnetain, L., Duval, X. and Letort, M. "On the Role
of Surface Oxides in the Graphite-Oxygen Reactions,"
Proc. of the Fourth Conf. on Carbon, p.107, Perga-
mon Press (1960).
36. Laine, N.R., Vastola, F.J. and Walker, P.L., Jr., "The
Role of the Surface Complex in the Carbon-Oxygen
Reaction," Proc. of the Fifth Conf. on Carbon,
Vol. 2, p.211, Pergamon Press (1963).
37. Nagle, J. and Strickland-Constable, R.F., "Oxidation of
Carbon Between 1000-2000°C," Proc. of the Fifth
Conf. on Carbon, Vol. 1, p.154, Pergamon Press (1962).
38. Walls, J.R. and Strickland-Constable, R.F., "Oxidation
of Carbon Between 1000-2400°C," Carbon, 1, 333 (1964).
39. Blyholder, G., Binford, J.S., Jr. and Eyring, H., "A
Kinetic Theory for the Oxidation of Carbonized
Filaments," J. Phys. Chem., 62, 263 (1958).
40. Hennig, G.R., "Electron Microscope Studies of Graphite
Single Crystals," Proc. of the Fourth Conf. on
Carbon, p.145, Pergamon Press (1960).
41. Hennig, G.R., "Surface Oxides on Graphite Single Cry-
stals," Proc. of the Fifth Conf. on Carbon, p.143,
Pergamon Press (1962).
42. Hennig, G.R. and Kanter, M.A., "Effect of Lattice De-

- fects on the Reactivity of Graphite," Fourth Int. Symp. on the Reactivity of Solids, p.648, Elsevier Publishing Co. (1961).
43. Thomas, J.M. and Hughes, E.E.G., Carbon, 1, 209 (1964).
 44. Hughes, E.E.G., Thomas, J.M., Reed, R. and Marsh, H., Carbon, 1, 339 (1964).
 45. Thomas, J.M., "Microscopic Studies of Graphite Oxidation," Chemistry and Physics of Carbon, Vol. 1, p.121, Walker, P.L., Jr., ed., Marcel Dekker Inc., N.Y. (1965).
 46. Harker, H., Proc. of the Fourth Conf. on Carbon, p.125, Pergamon Press (1960).
 47. Amariglio, H. and Duval, X., Carbon, 4, 323 (1966).
 48. Roscoe, C., Carbon, 6, 365 (1968).
 49. Evans, T. and Phaal, C., Proc. of the Fifth Conf. on Carbon, Vol. 1, p.147, Pergamon Press (1962).
 50. Hart, P.J., Vastola, F.J. and Walker, P.L., Jr., Carbon, 5, 363 (1967).
 51. Lussow, R.O., Vastola, F.J. and Walker, P.L., Jr., Carbon, 5, 591 (1967).
 52. Bansal, R.C., Vastola, F.J. and Walker, P.L., Jr., Carbon, 8, 443 (1970).
 53. Walker, P.L., Jr., Vastola, F.J. and Hart, P.J., Fundamentals of Gas-Surface Interactions, p.207, Saltzburg, H. and Smith, J.N., Jr., eds., Academic Press (1967).

54. Bowman, J.C., "Imperfections in the Graphite Structure,"
Proc. of the First and Second Conf. on Carbon,
Waverly Press, Baltimore (1956).
55. Nightingale, R.E. and Snyder, W.A., "Distribution of
Radiation Damage in Graphite," Proc. of the Third
Conf. on Carbon, Pergamon Press (1959).
56. Price, R.J. and Bokros, J.C., "Annealing of Neutron
Irradiated Pyrocarbons," Carbon, 9, 555 (1971).
57. Antonowicz, K., "Formation of Spin Centers in Carbons
by Oxidation and their Thermal Anneal," Proc. of
Fifth Conf. on Carbon, Vol. 1, Pergamon Press (1962).
58. Radcliffe, S.W. and Appleton, J.P., "Soot Oxidation
Rates in Gas Turbine Engines," Combustion Science
and Technology, 4, 171 (1971).
59. Streznewski, J. and Turkevich, J., "The Reaction of
Carbon with Oxygen Atoms," Proc. of the Third Conf.
on Carbon, p.273, Pergamon Press (1959).
60. Vastola, F.J., Walker, P.L., Jr. and Wightman, J.P.,
"The Reaction between Carbon and the Products of
Hydrogen, Oxygen and Water Microwave Discharges,"
Carbon, 1, 11 (1963).
61. Marsh, H., O'Hair, T.E. and Wynne-Jones, W.F.K., "Oxi-
dation of Carbons and Graphites by Atomic Oxygen:
Kinetic Studies," Trans. Faraday Soc., 61, 274 (1965).
62. Marsh, H., O'Hair, T.E. and Reed, R., "Oxidation of
Carbons and Graphites by Atomic Oxygen: An Electron

- Microscope Study of Surface Changes," Trans. Faraday Soc., 61, 285 (1965).
63. March, H., O'Hair, T.E. and Wynne-Jones, W.F.K., "The Carbon-Atomic Oxygen Reaction--Surface Oxide Formation on Paracrystalline Carbon and Graphite," Carbon, 7, 555 (1969).
64. McCarroll, B. and McKee, D.W., "The Reactivity of Graphite Surfaces with Atoms and Molecules of H_2 , O_2 and N_2 ," Carbon, 9, 301 (1971).
65. Buck, U. and Pauly, H., Ziets. fur Physik, 208, 390 (1968).
66. Moran, J.P., "Experiments on Scattering of Mono-Energetic Argon Beams by Heated Platinum," M.I.T. Fluid Dyn. Res. Lab. Rept. T68-1 (1968).
67. Logan, R.M. and Stickney, R.E., "A Simple Classical Model for the Scattering of Gas Atoms from a Solid Surface," J. Chem. Phys., 44, 195 (1966).
68. Merrill, R.P., Catalysis Review, 4, 115 (1970).
69. Yamamoto, S. and Stickney, R.E., "Analysis of 'Lock-In' Detection of Modulated Molecular Beams Scattered from Solid Surfaces," J. Chem. Phys., 47, 3 (1967).
70. Krakowski, R.A. and Olander, D.R., J. Chem. Phys., 49, 5027 (1968).
71. Smith, J.N. and Fite, W.L., J. Chem. Phys., 37, 698 (1962).
72. McKinley, J.D., J. Chem. Phys., 40, 120 (1964).
73. Anderson, J. and Boudart, M., J. Catalysis, 13, 216 (1964).

74. Coltharp, R.N., Scott, J.T. and Muschlitz, E.E., Jr.,
J. Chem. Phys., 51, 5180 (1969).
75. Rose, D.J. and Brown, S.C., J. Appl. Phys., 28, 561
(1957).
76. Lam, C.K., "Development of a Nozzle Beam Containing
Atomic Oxygen," University of Toronto, Institute
for Aerospace Studies, Technical Note No. 153 (1970).
77. Vincenti, W.G. and Kruger, C.H., Jr., Introduction to
Physical Gas Dynamics, John Wiley, New York (1965).
78. NACA Tech. Note 3270.
79. Anderson, J.B., Andres, R.P. and Fenn, J.B., Advances
in Atomic and Molecular Physics, Vol. 1, p.345,
Academic Press, New York (1965).
80. Clausen, P., Ann. Physik, 12, 961 (1932).
81. Price, W.J., Nuclear Radiation Detection, McGraw Hill,
New York (1964).
82. McDowell, C.A., Mass Spectrometry, McGraw-Hill, New
York (1963).
83. Harrison, H., Hummer, D.G. and Fite, W.L., J. Chem.
Phys., 41 2567 (1964).
84. Harrison, H., Hummer, D.G. and Fite, W.L., Document 8097,
Photoduplication Service, Library of Congress, Wash-
ington D.C.
85. Seikhaus, W.J., Jones, R.H. and Olander, D.R., J. Appl.
Phys., 41, 4392 (1970).
86. Parratt, L.G., Probability and Experimental Errors in

Science, John Wiley, New York (1961).

87. "Tables of Normal Probability Functions," National Bureau of Standards, Washington, D.C. (1953).
88. Plunkett, J.D. and Kingery, W.D., "The Spectral and Integrated Emissivity of Carbon and Graphite," Proc. of the Fourth Conf. on Carbon, p.457, Pergamon Press (1960).
89. Wang, K.L. and Crawford, C.K., Massachusetts Institute of Technology, Particle Optics Laboratory, Technical Report No. 6, p.27 (1971).
90. Kostkowski, H.J. and Lee, R.D., "Theory and Methods of Optical Pyrometry," National Bureau of Standards, Monograph 41 (1962).
91. Giordmaine, J.A. and Wang, T.C., "Molecular Beam Formation by Long Parallel Tubes," J. Appl. Phys., 31, 463 (1960).
92. Jones, R.H., Olander D.R. and Kruger, V.P., "Molecular-Beam Sources Fabricated from Multichannel Arrays. I. Angular Distributions and Peaking Factors," J. Appl. Phys., 40, 4641 (1961).
93. Meyer, L., "The Energy Exchange between Argon and a Hot Graphite Surface," Proc. of the Fourth Conf. on Carbon, p.155, Pergamon Press (1960).
94. Siekhaus, W.L., Schwartz, J.A. and Olander, D.R., "A Modulated Molecular Beam Study of the Energy of Simple Gases Scattered from Pyrolytic Graphite,"

presented at the Eighth International Symposium on
Rarefield Gas Dynamics at Stanford (1972).

95. Batty, J.C. and Stickney, R.E., "Quasiequilibrium Treatment of Gas-Solid Reactions. I. Evaporation Rates of Volatile Species Formed in the Reaction of O_2 with W, Mo, and C," J. Chem. Phys., 51, 447 (1969).
96. Van Willigen, W., "Angular Distribution of Hydrogen Molecules Desorbed from Metal Surfaces," Physics Letters, 28A, 2, 80 (1968).
97. Palmer, R.L., Smith, J.N., Jr., Saltsburg, H. and O'Keefe, D.R., "Measurements of the Reflection, Adsorption, and Desorption of Gases from Smooth Metal Surfaces," J. Phys., 53, 5, 1666 (1970).
98. Dalbiri, A.E., Lee, T.J. and Stickney, R.E., "Spatial and Speed Distributions of H_2 and D_2 Desorbed from a Polycrystalline Nickel Surface," Surface Science, 26, 2, 522 (1971).
99. Cosma, G., "Angular Distribution of Scattered and Desorbed Atoms from Metal Surfaces," J. Chem. Phys., 48, 7, 3235 (1968).
100. Estermann, I. and Stern, O., Z. Physik, 61, 95 (1930).
101. Park, Chul and Appleton, J.P., "Shock-Tube Measurements of Soot Oxidation Rates," Combustion and Flames, 20, 369 (1973).

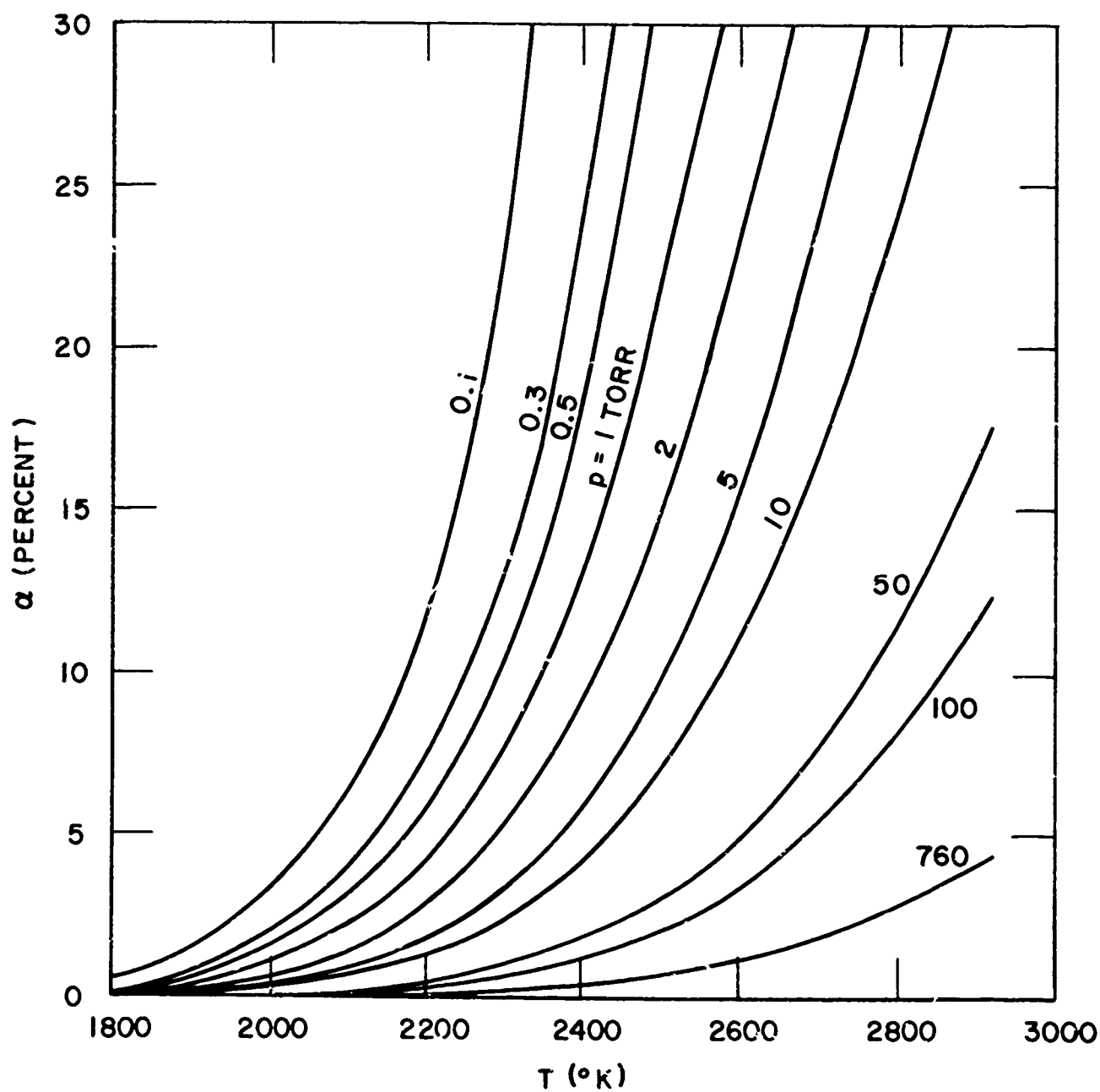


Fig. 1. Degree of Dissociation of Oxygen at Thermal Equilibrium

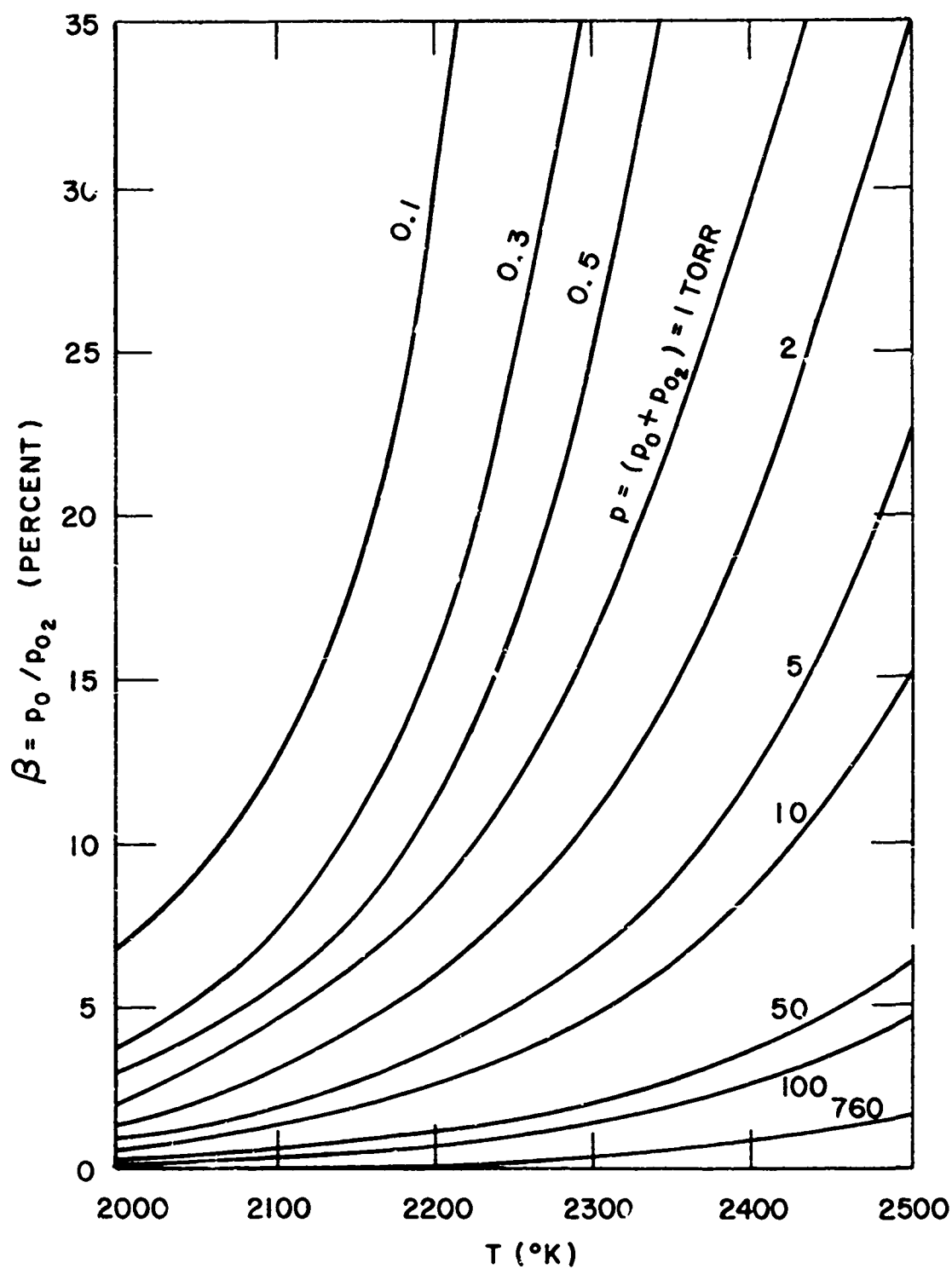
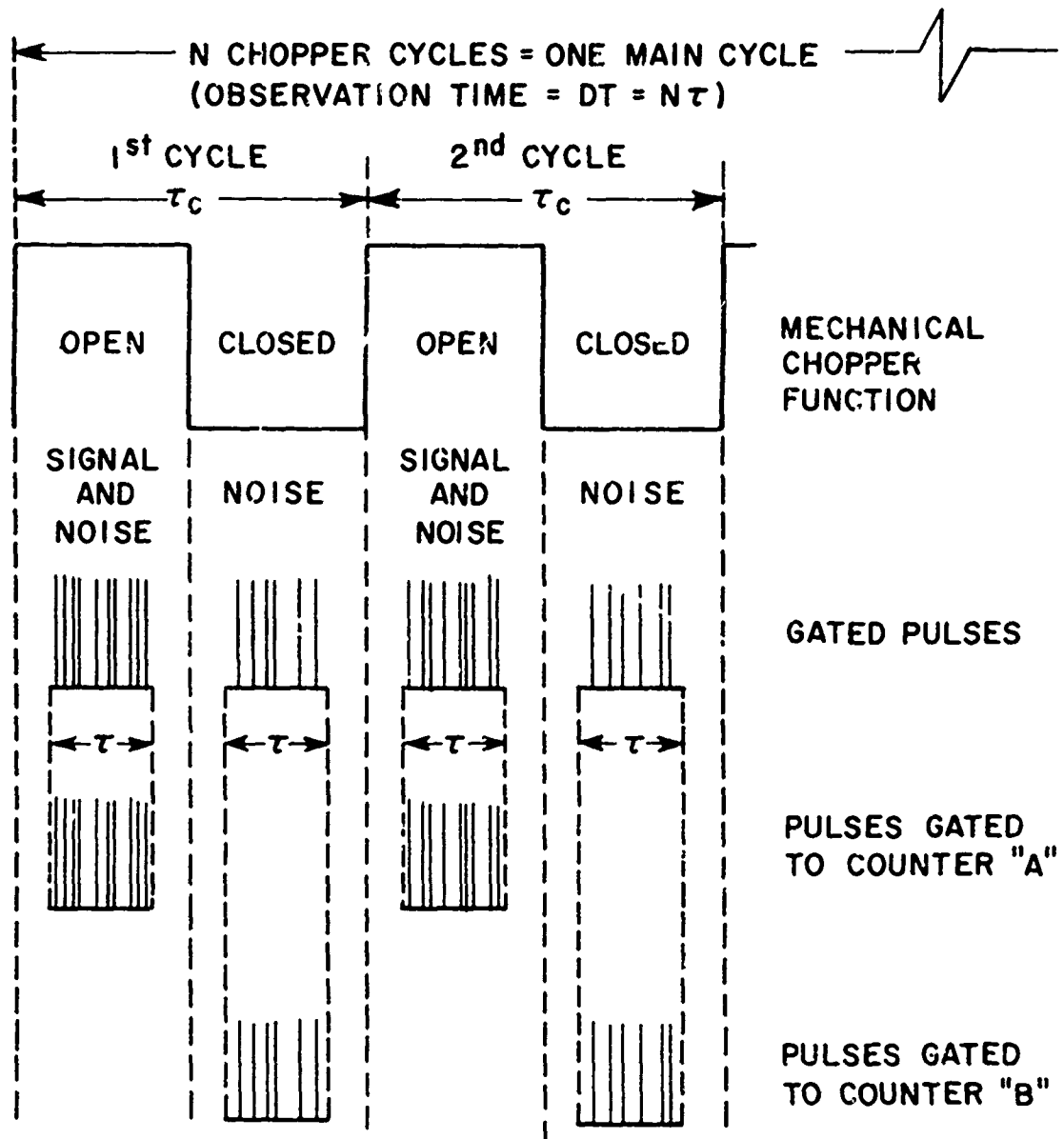


Fig. 2. Pressure Ratio of O to O_2 at Thermal Equilibrium



τ_c = CHOPPER PERIOD
 τ = COUNTER SAMPLING TIME
 D = DUTY CYCLE = $\tau / \tau_c \leq 0.5$
 N = PRESET CHOPPER CYCLES
 T = TOTAL ELAPSED TIME

Fig. 3. Timing Diagram for Chopper Mode Operation of DSC

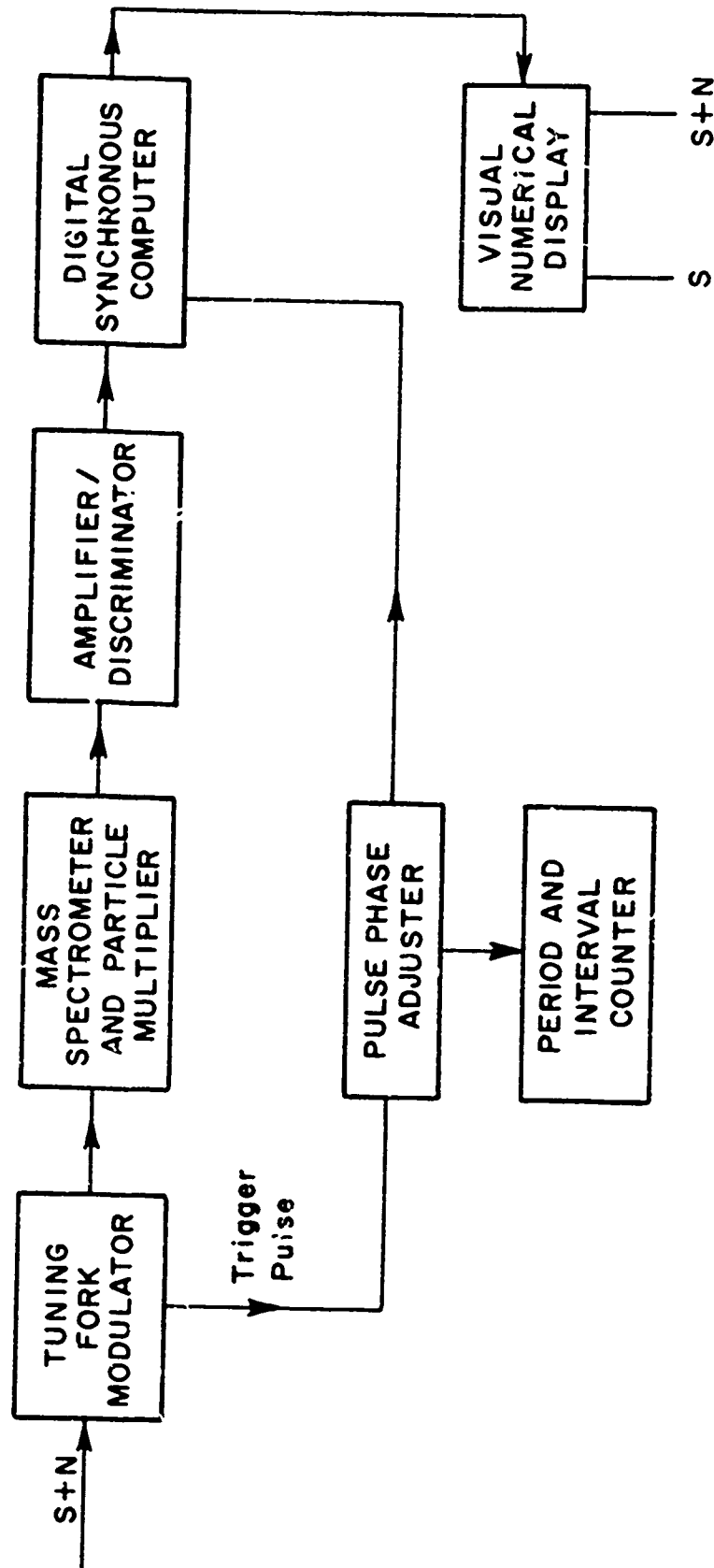


Fig. 4. Flow Chart for Signal Processing

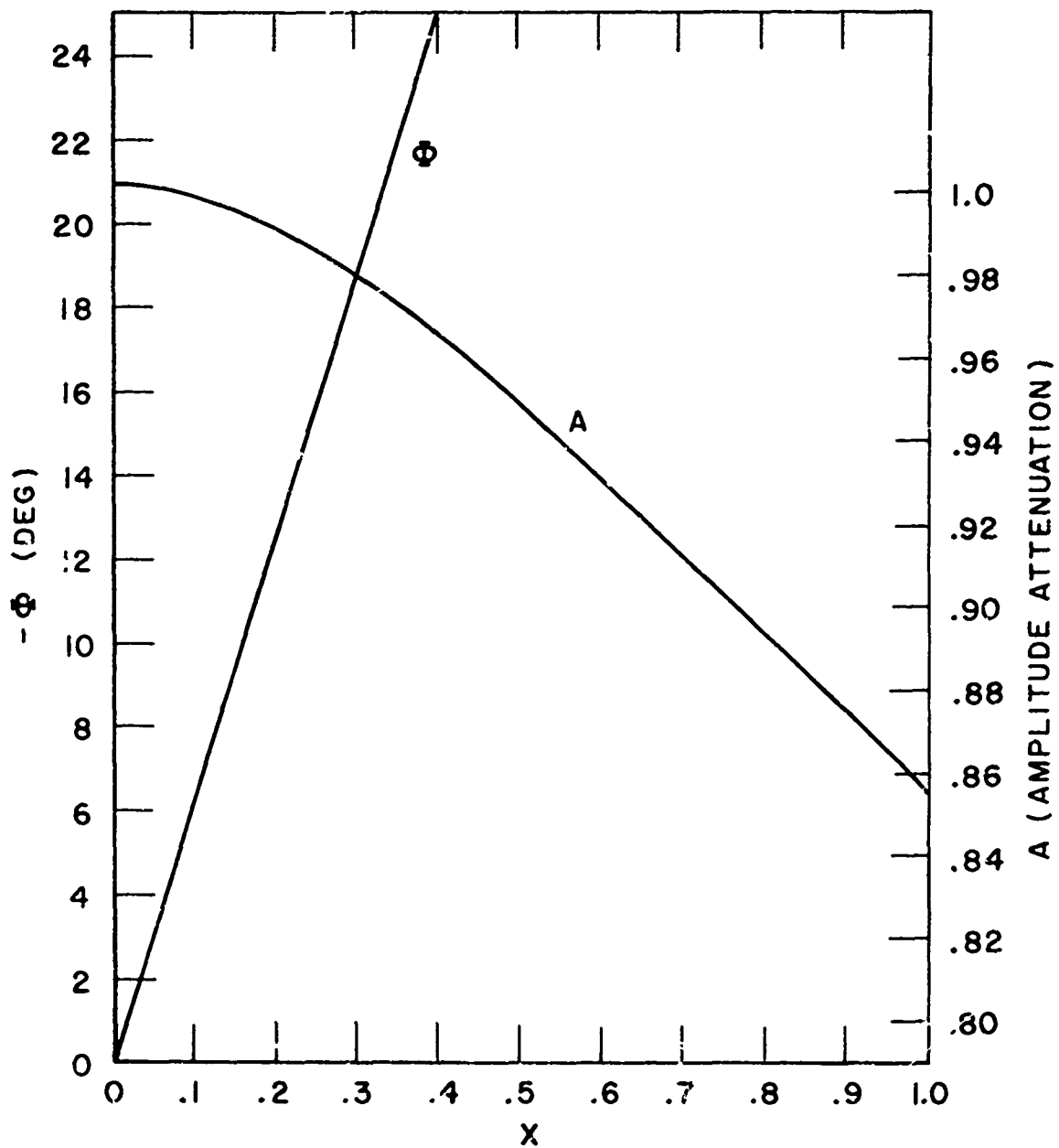


Fig. 5. Amplitude Attenuation and Phase Shift for Square Modulated Maxwellian Beam (Ref. 29)

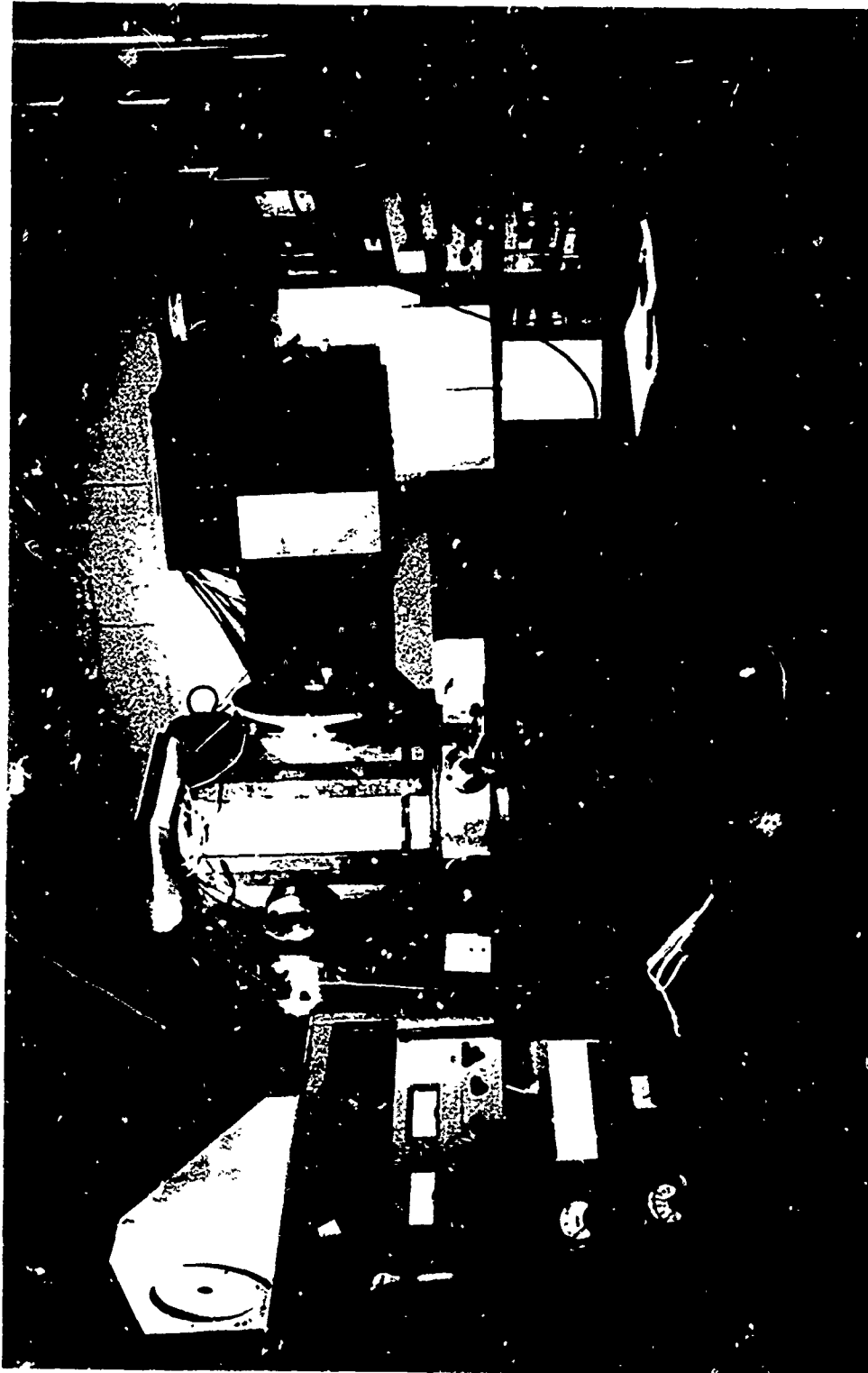


Fig. 6. Overall View of Experimental Setup

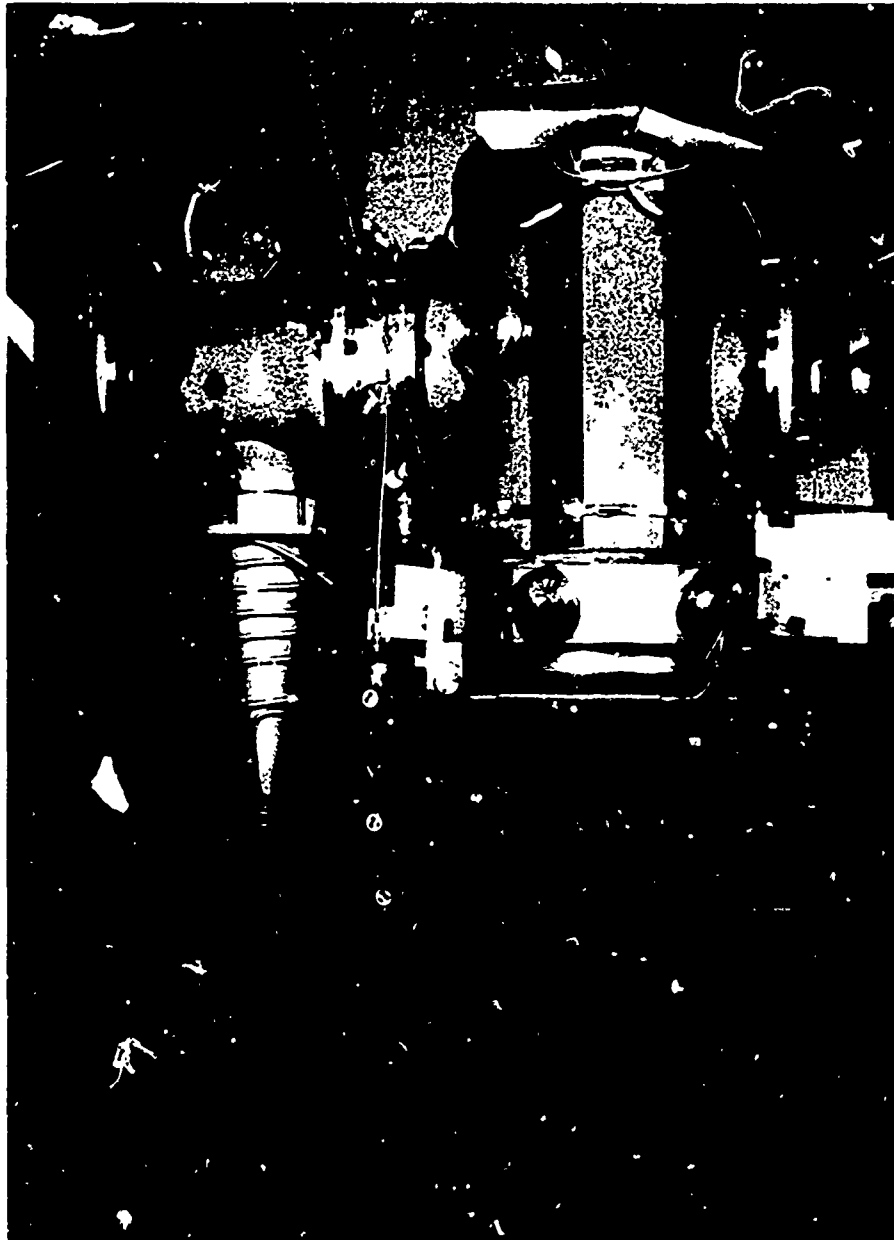


Fig. 7. Vacuum System

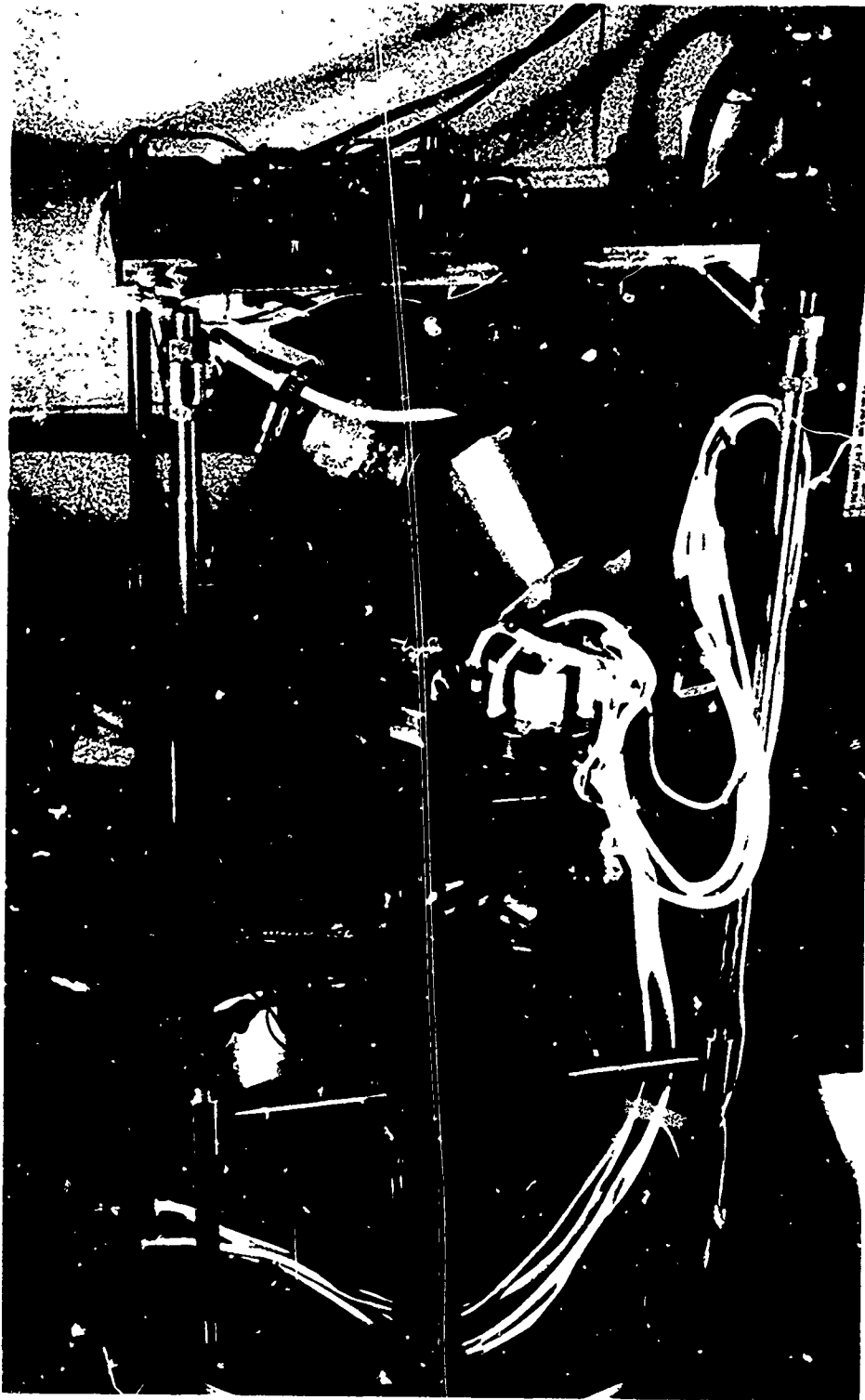


Fig. 8. Interior View of Test Chamber

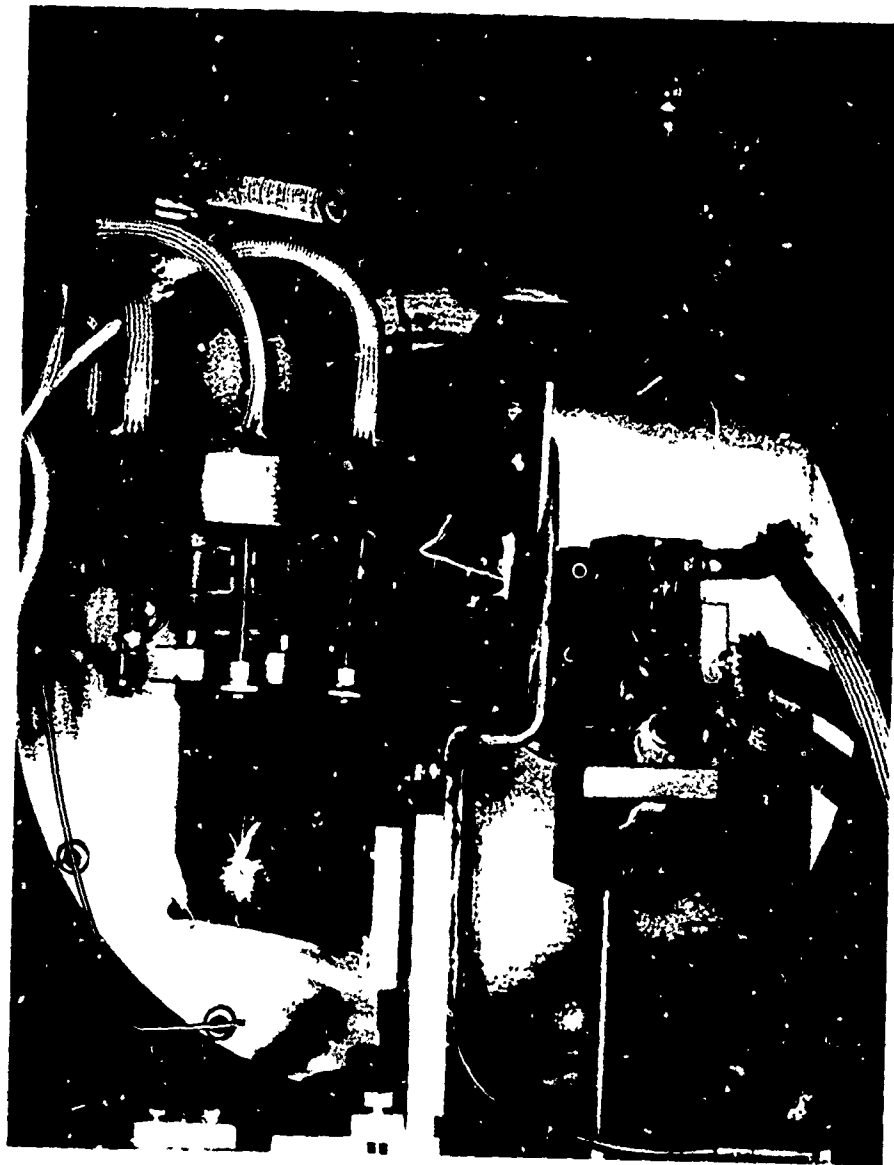
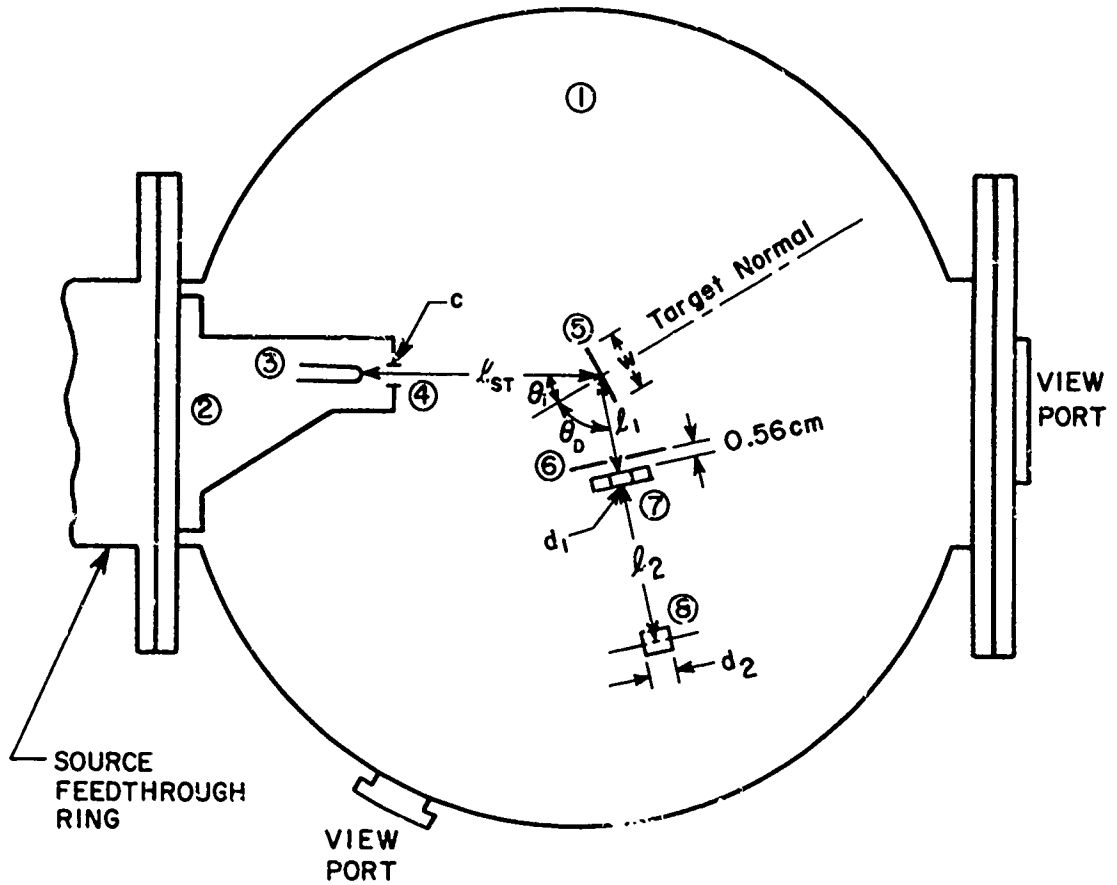


Fig. 9. Source Housing and Target-Detector Assembly



1. 18" I. D. Test Chamber
2. Source Chamber
3. Source
4. Source Collimator
5. Target
6. Chopper Shield-Collimator
7. Chopper (Tuning Fork)
8. Mass Spectrometer Ionizer

c = 0.24 cm dia.

$$d_1 = 0.51 \text{ cm}$$
$$d_2 = 0.98 \text{ cm}$$
$$\ell_1 = 2.72 \text{ cm}$$
$$l_2 = 6.90 \text{ cm}$$
$$w = 1.00 \text{ cm}$$

Fig. 10. Schematic Diagram of the Test Chamber Interior Arrangement: Top View

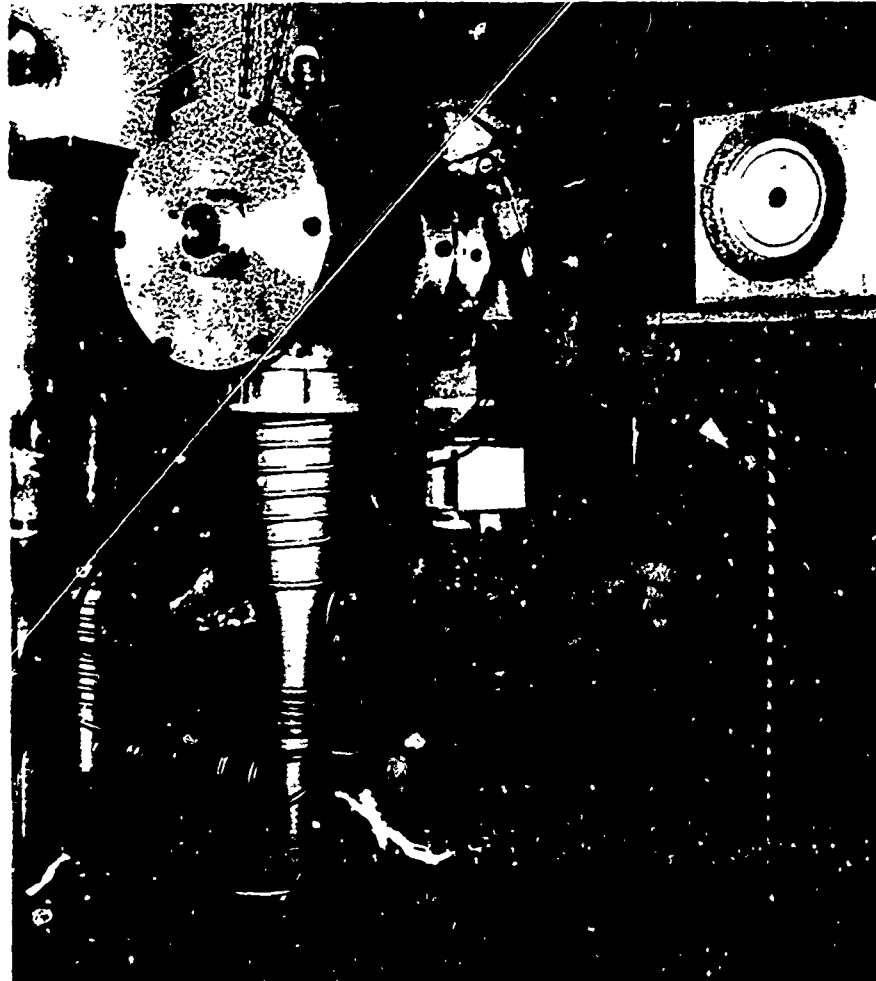


Fig. 11. Source Chamber



Fig. 12. Interior View of Source Chamber



Fig. 13. Target Holder



Fig. 14. Tuning Fork Chopper

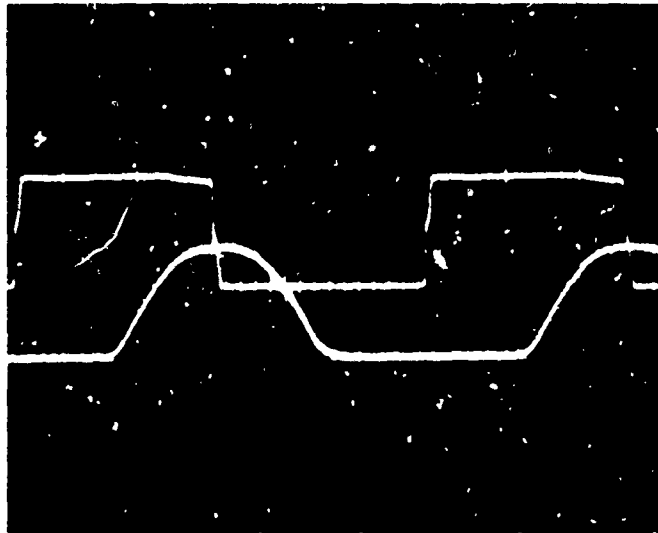


Fig. 15a. Upper Trace: Reference Signal
(Chopper Driver Voltage)

Lower Trace: Measured Shutter
Function

Time Scale: 500 μ sec/cm

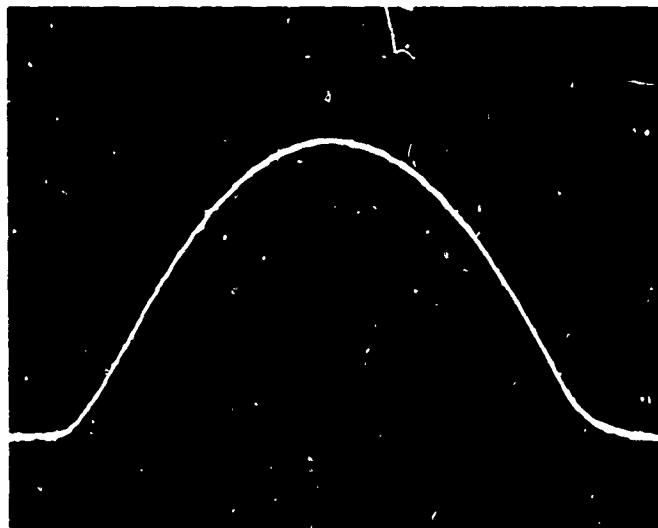


Fig. 15b. Measured Shutter Function
by Light-Photocell Scheme

Time Scale: 200 μ sec/cm

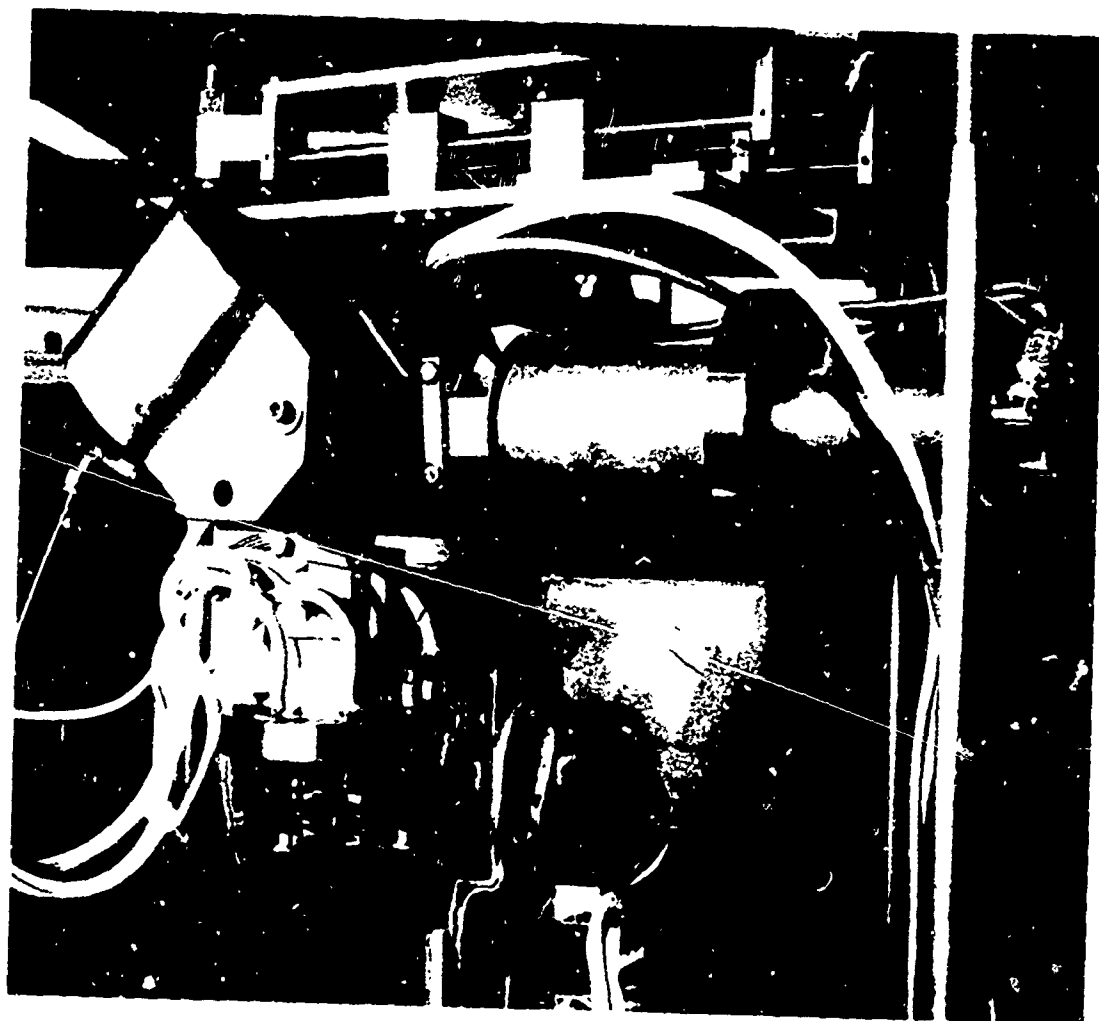


Fig. 16. Mass Spectrometer

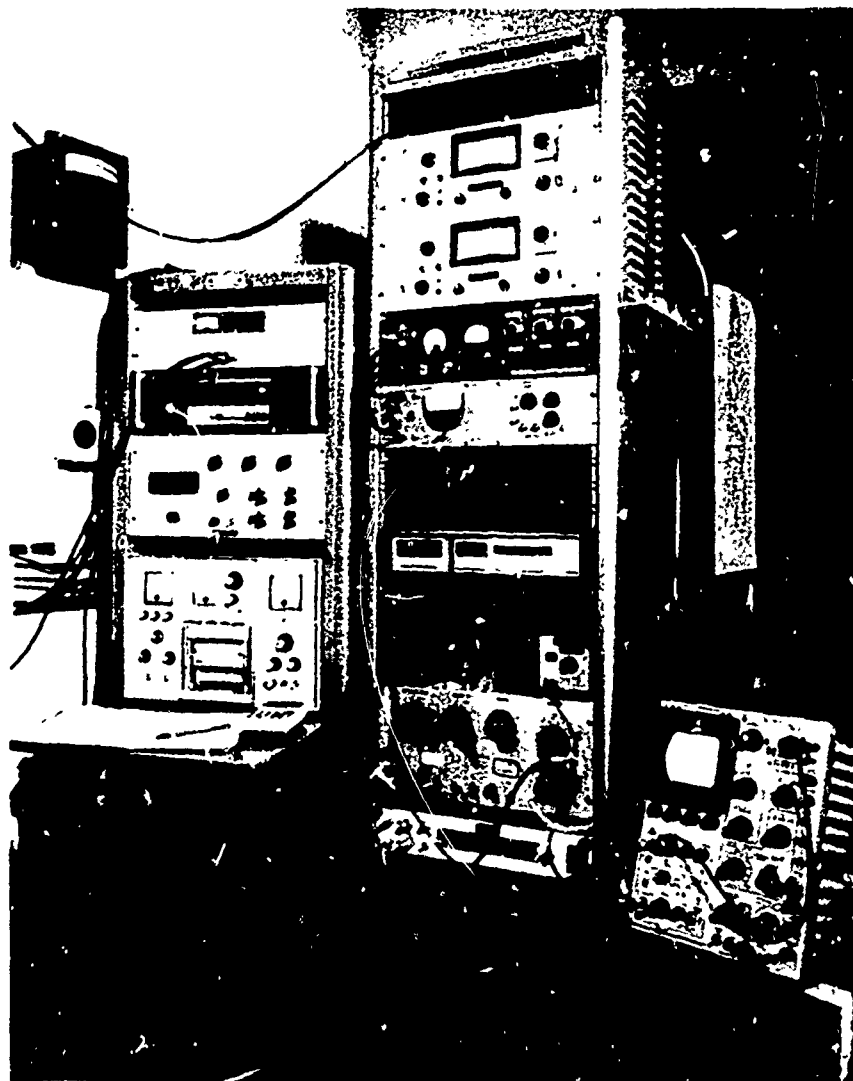


Fig. 17. Instrument Panels

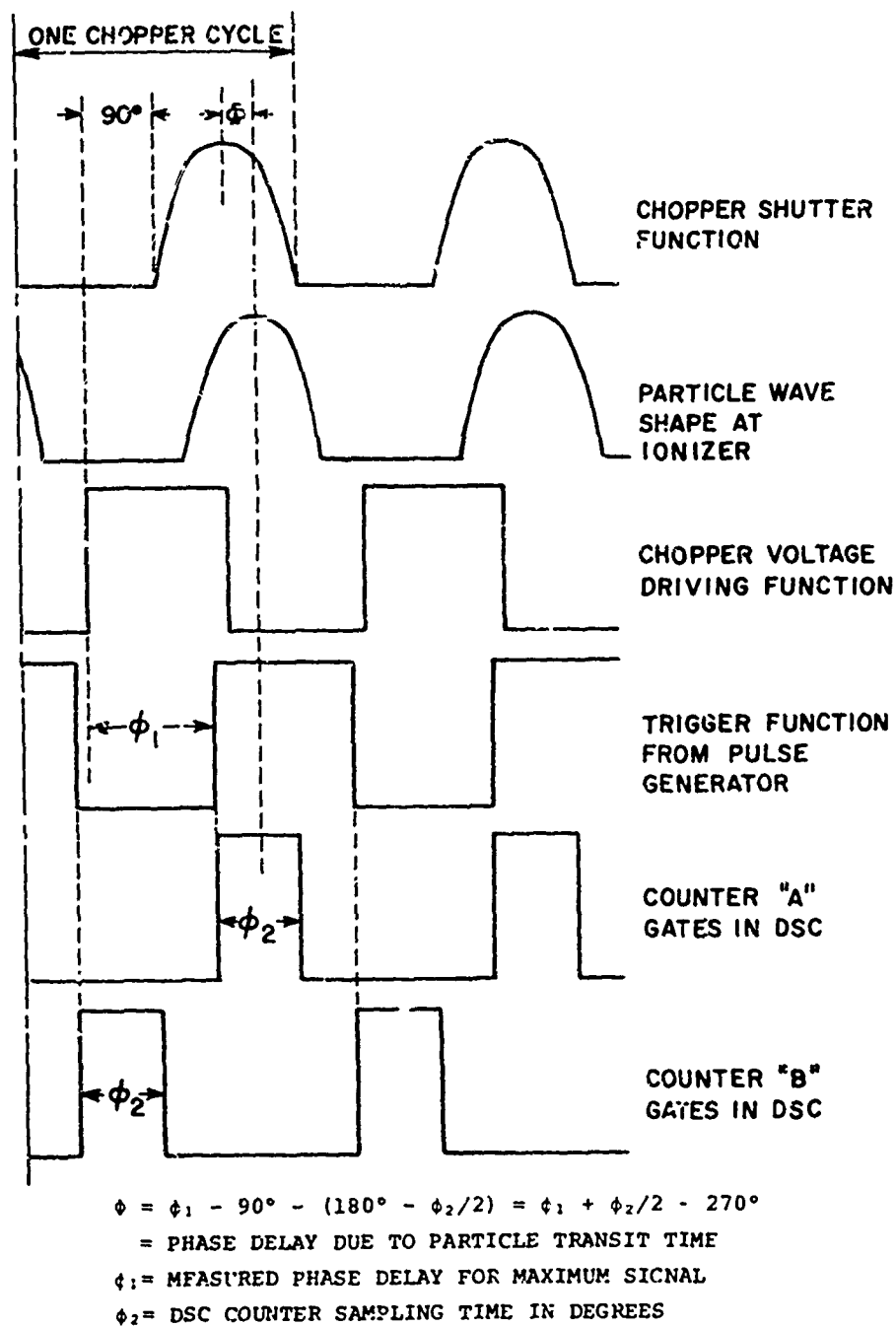


Fig. 18. Timing Diagram for the Phase Adjusting Scheme

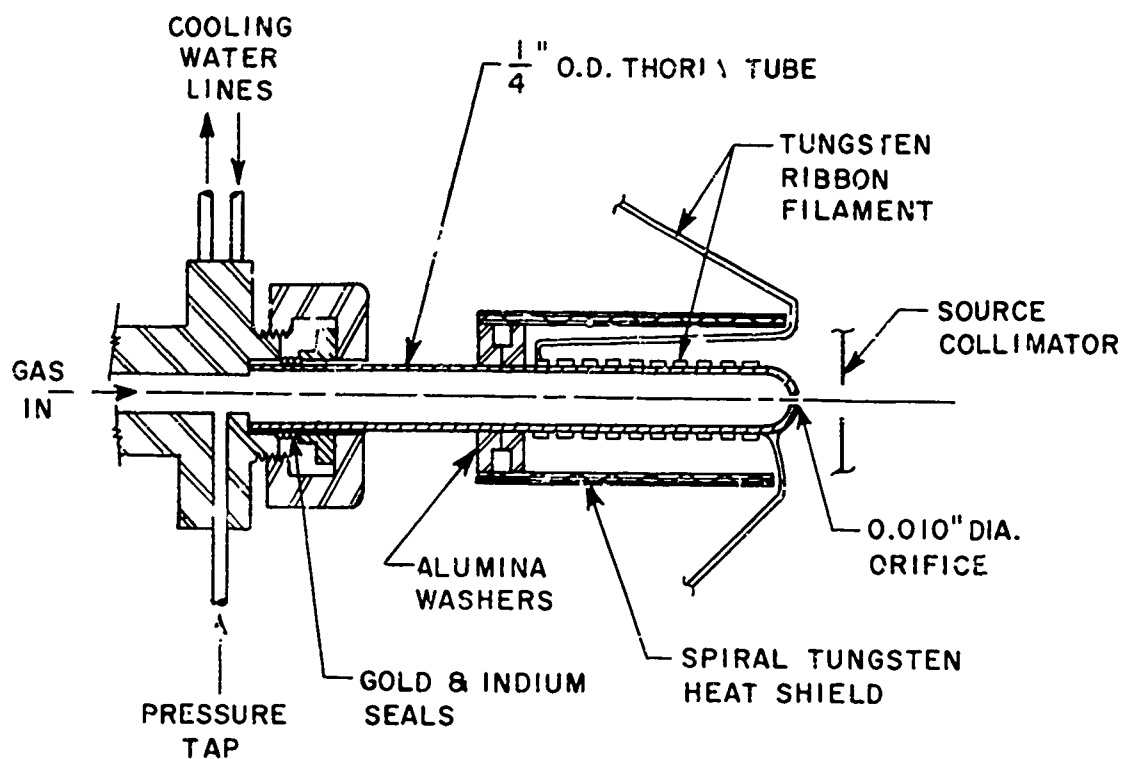


Fig. 19. Cross-Section Diagram of Beam Source

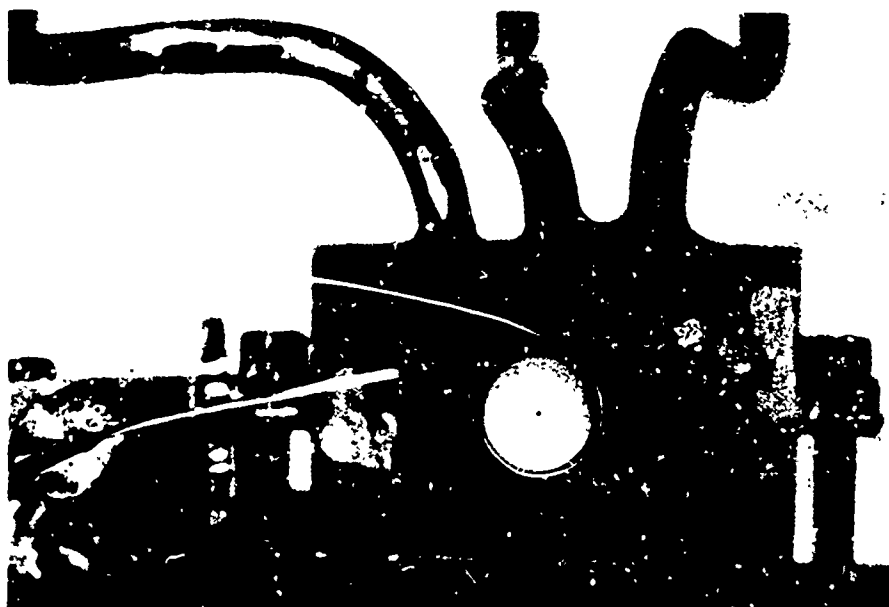


Fig. 20a. Source Orifice and Radiation Shield

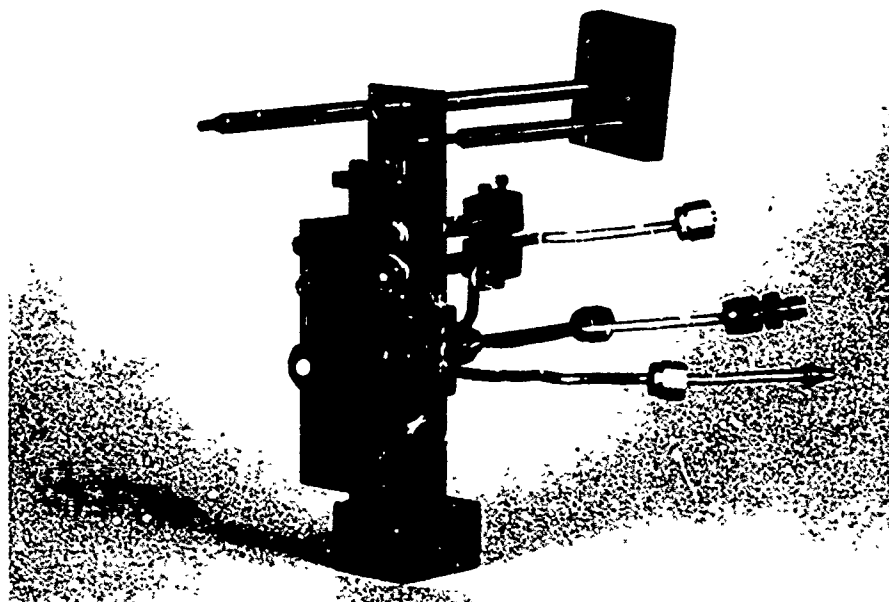


Fig. 20b. Source Support Assembly

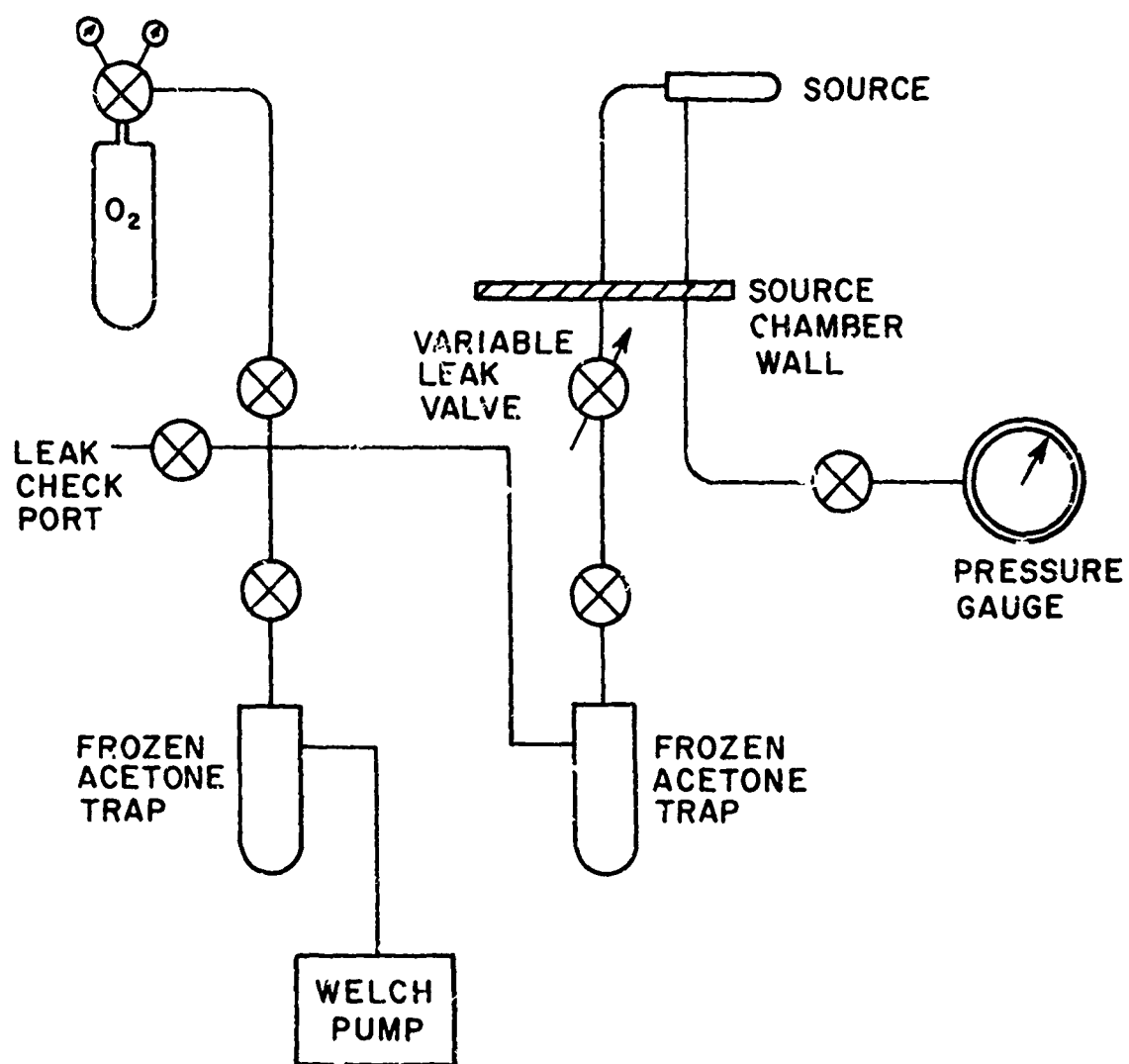


Fig. 21. Schematic Diagram of Gas Inlet System

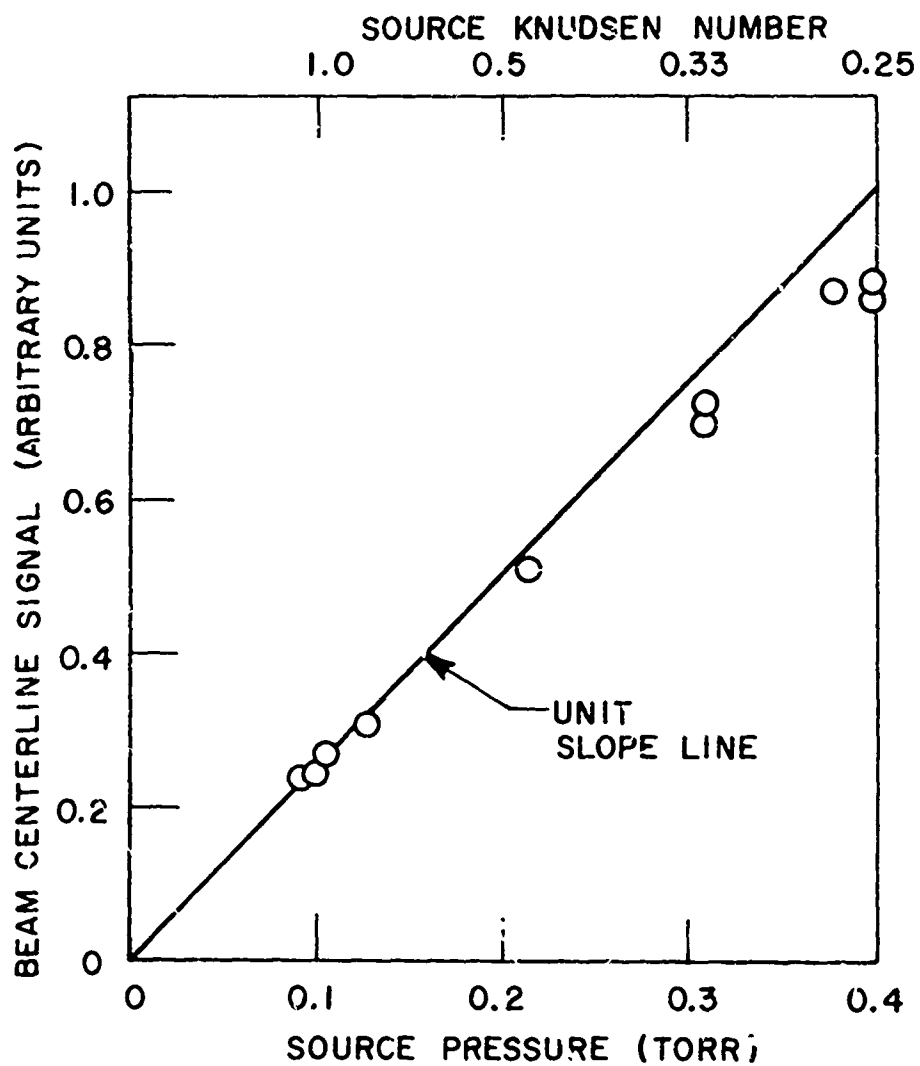


Fig. 22. Room Temperature Beam Centerline Signal Versus Source Pressure

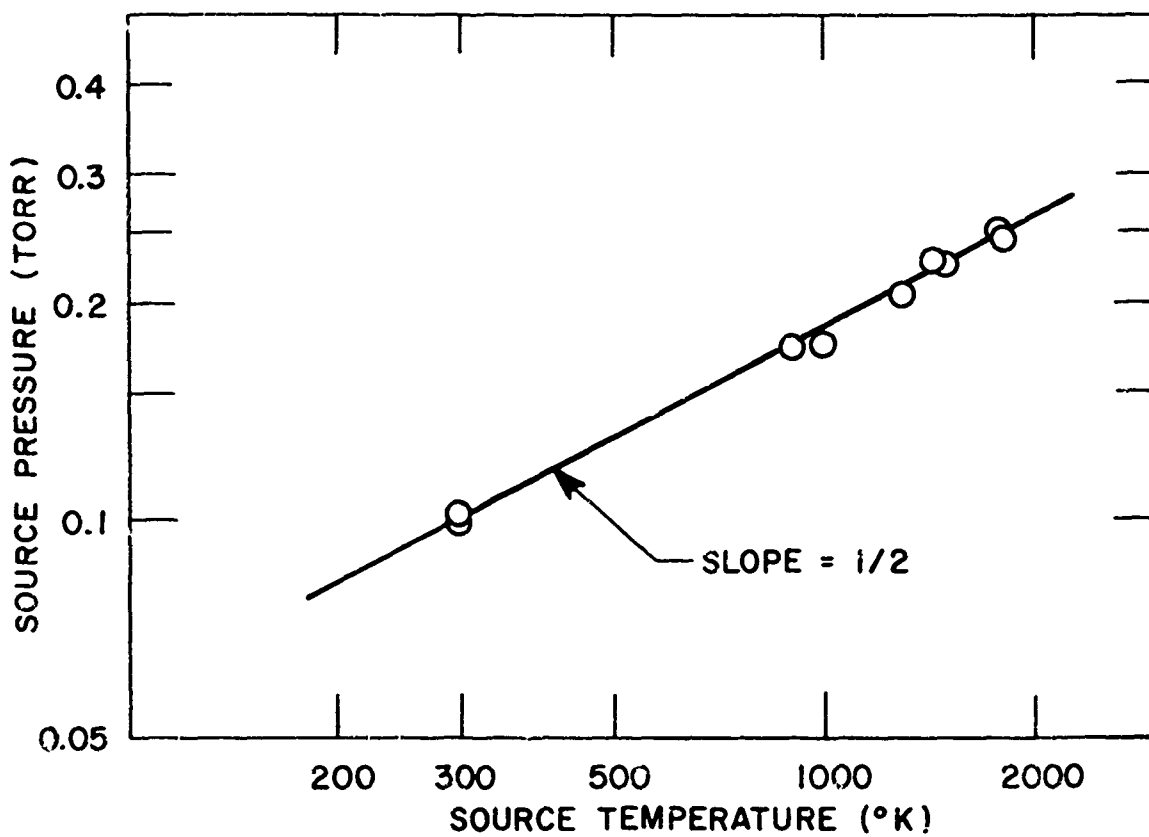


Fig. 23. Source Pressure Versus Source Temperature for Constant Leak Rate

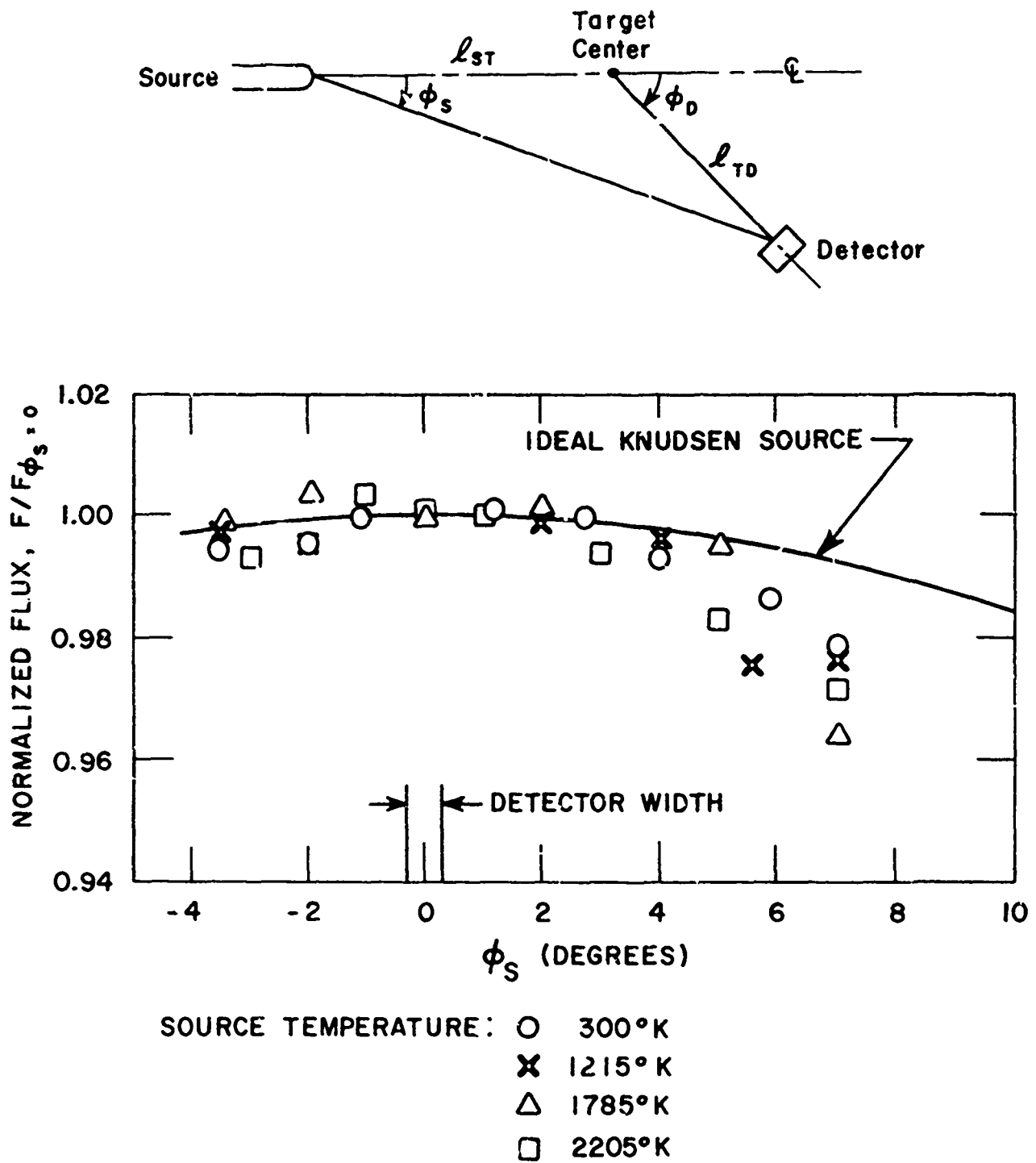


Fig. 24. Source Flux Angular Distribution

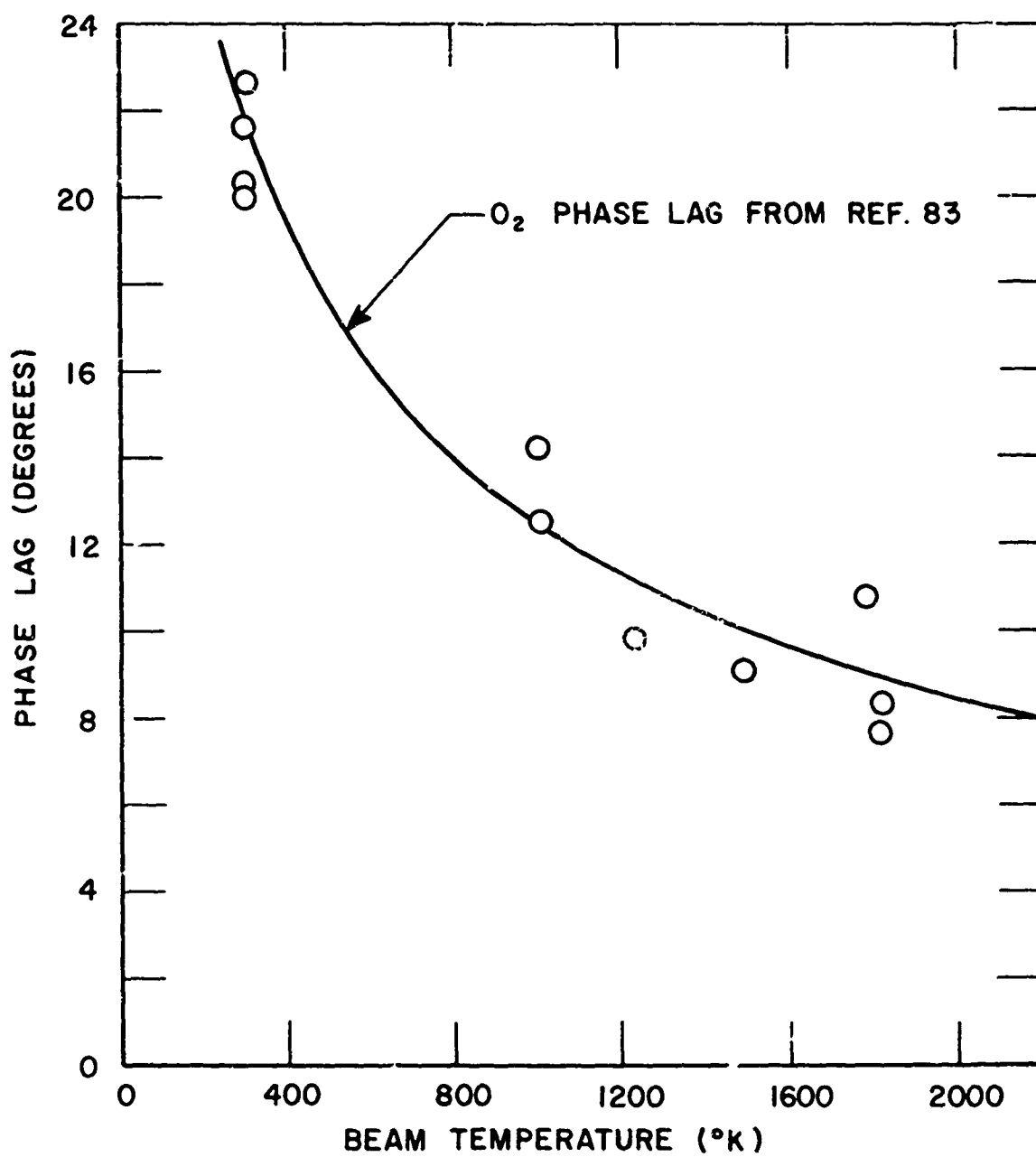
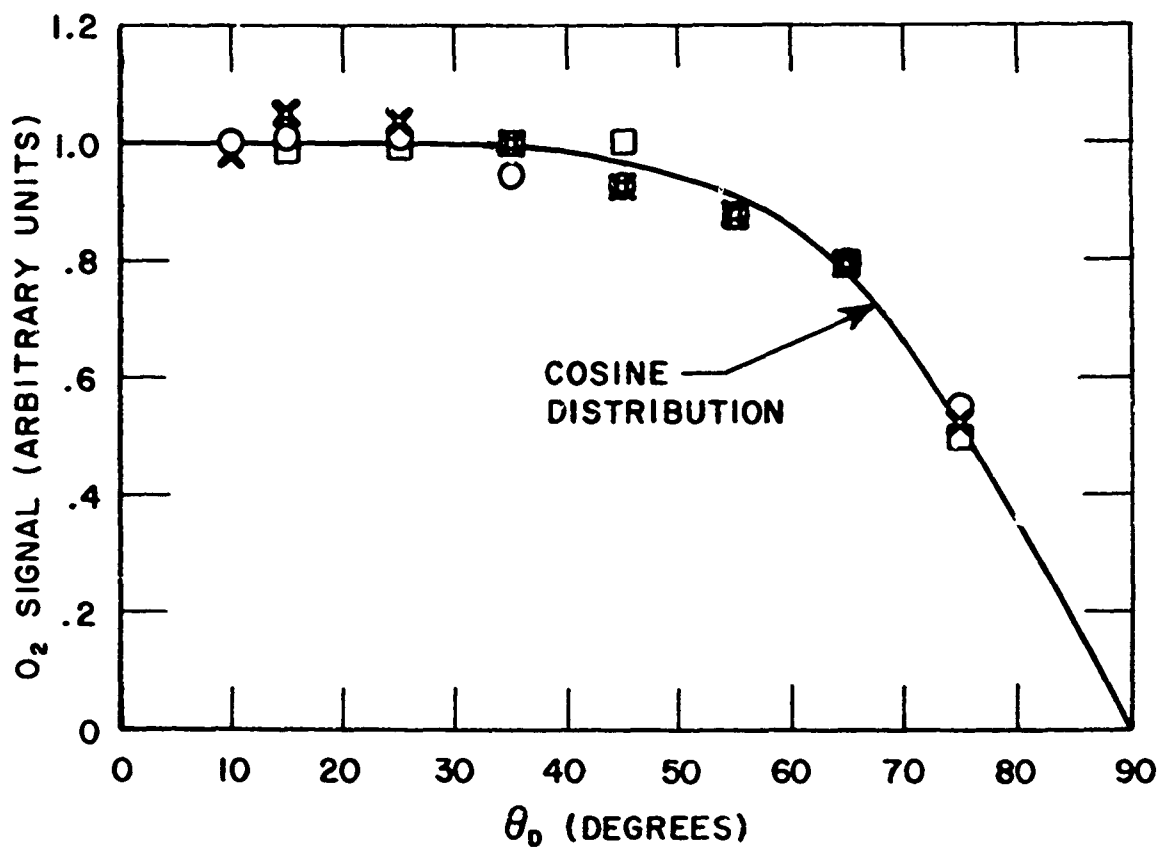
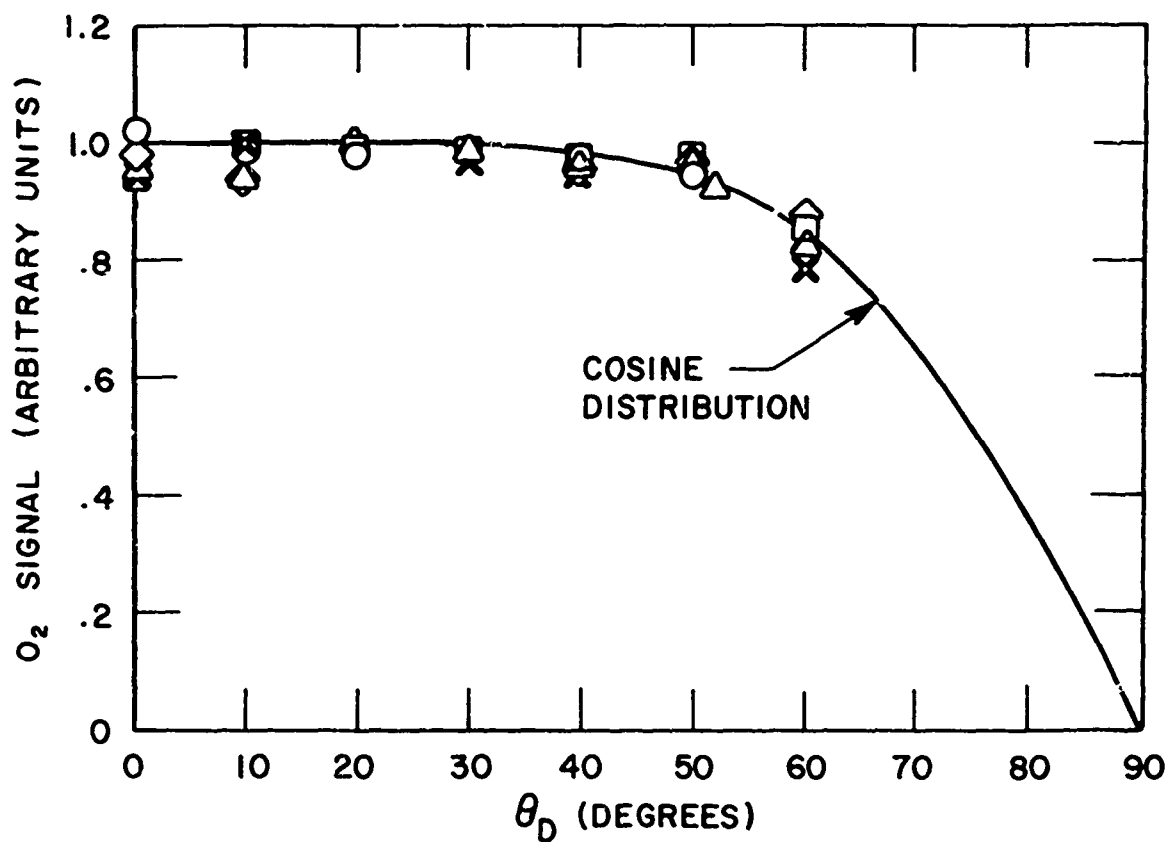


Fig. 25. Incident Beam Phase Lag



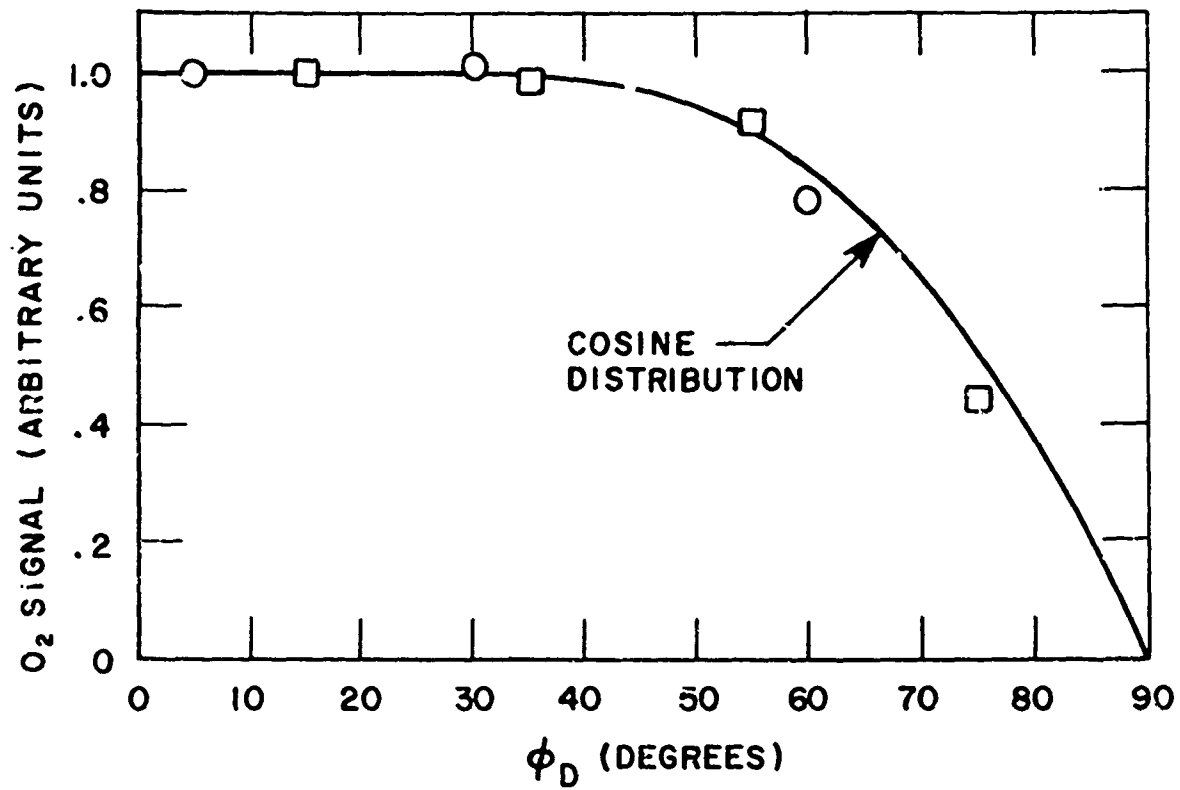
TARGET TEMPERATURE: \square 1375°K
X 1385°K
O 1405°K

Fig. 26. Angular Distribution of Scattered Room Temperature O_2 at $\theta_i = 45^\circ$



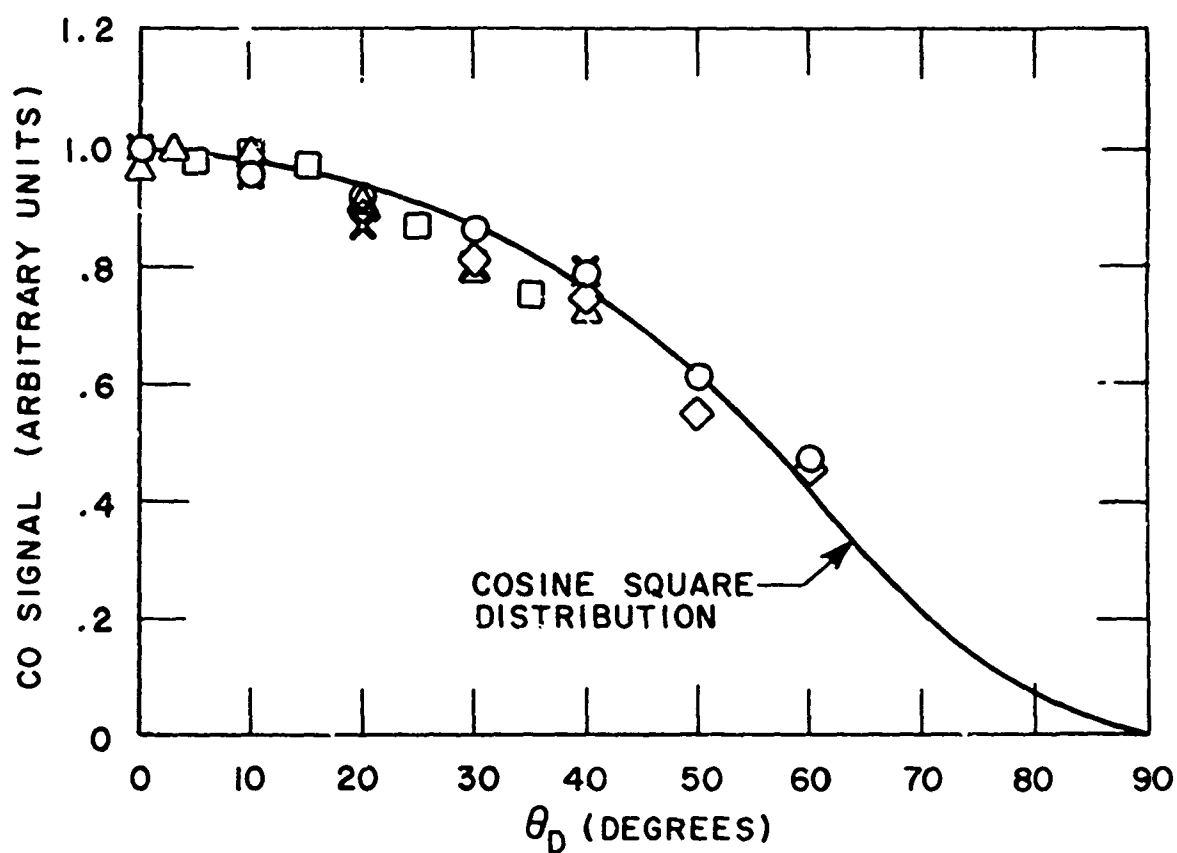
TARGET TEMPERATURE: Δ 1375°K
 \diamond 1400°K
 \square 1400°K
 \times 1405°K
 \circ 1410°K

Fig. 27. Angular Distribution of Scattered Room Temperature O₂ at $\theta_i = 60^\circ$



$T_B = 1370^\circ\text{K}$; $T_T = 1380^\circ\text{K}$; θ_i : \square 45°
 \circ 60°

Fig. 28. Angular Distribution of Scattered High Temperature O₂



$\theta_i = 45^\circ$; T_T : □ 1405°K

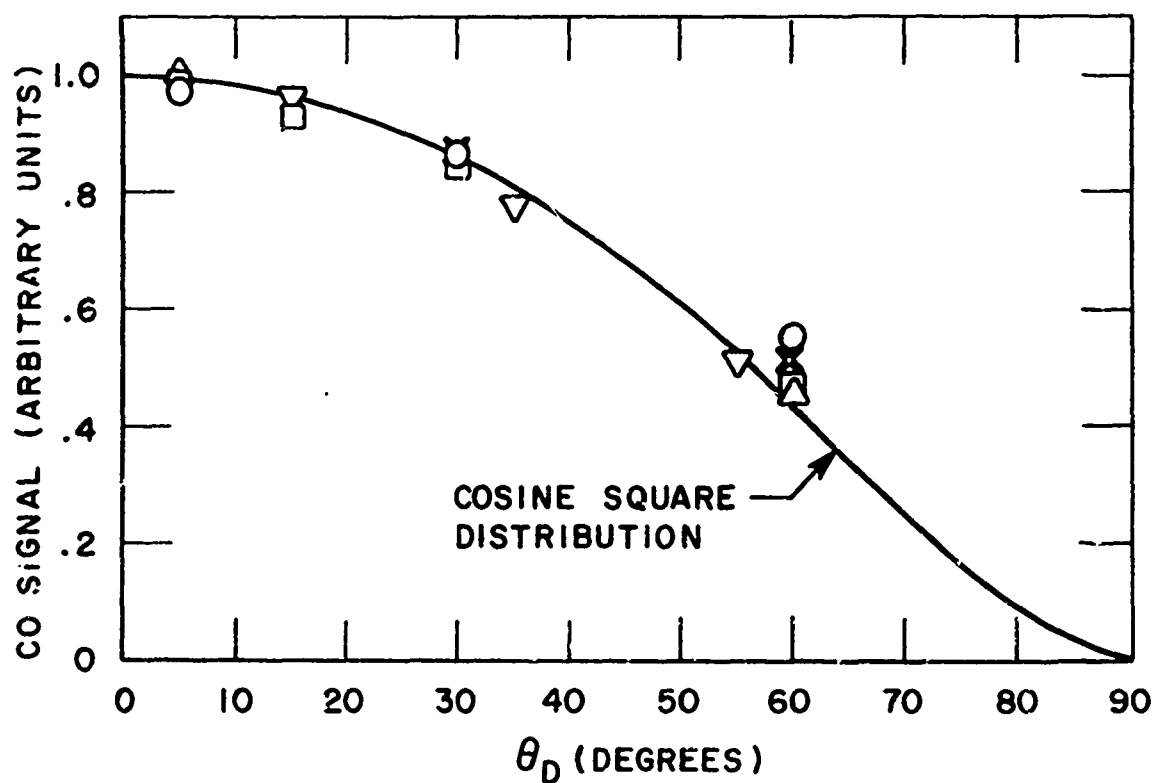
△ 1410°K

$\theta_i = 60^\circ$; T_T : ◇ 1375°K

○ 1380°K

× 1410°K

Fig. 29. Angular Distribution of Desorbed CO
for Room Temperature Incident Beam



$\theta_i = 45^\circ; T_T = 1380^\circ\text{K}; T_B: \nabla - 1370^\circ\text{K}$

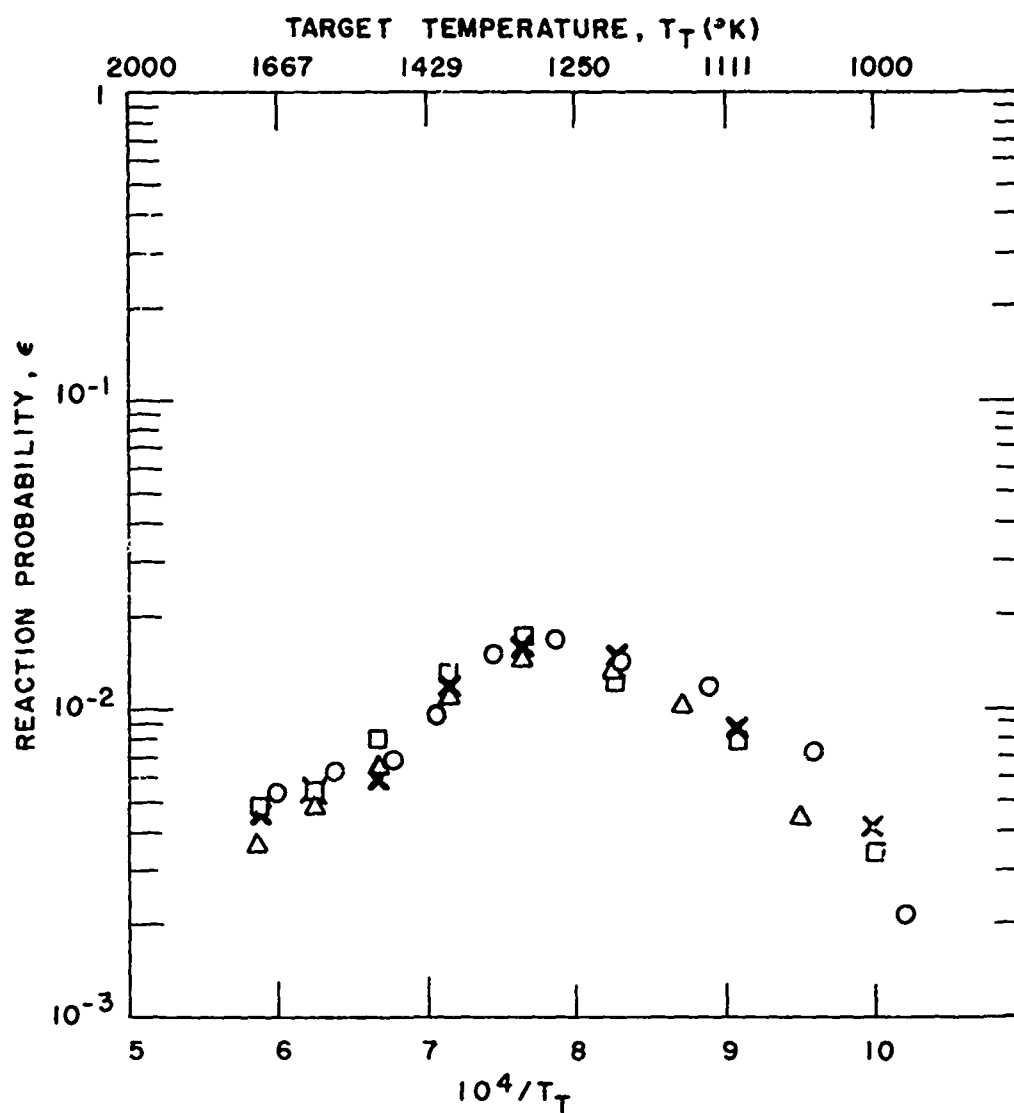
$\theta_i = 60^\circ; T_T = 1380^\circ\text{K}; T_B: \circ - 1370^\circ\text{K}$

$\square - 1725^\circ\text{K}$

$T_T = 1355^\circ\text{K}; T_B: \times - 2220^\circ\text{K}$
 $= 1390^\circ\text{K}; \quad \triangle - 2200^\circ\text{K}$

DISSOCIATED
BEAMS

Fig. 30. Angular Distribution of Desorbed CO for High Temperature Incident Beam



BEAM TEMP. T_B

X 300 °K } PRESENT DATA
 Δ 1475 °K } $I_{O_2} = 1.3 \times 10^{14}$ #/CM² - SEC
 □ 1875 °K }
 ○ 300 °K SHIH²⁹; $I_{O_2} = 8.0 \times 10^{15}$ #/CM² - SEC

Fig. 31. Reaction Probability of O_2 Versus Target Temperature

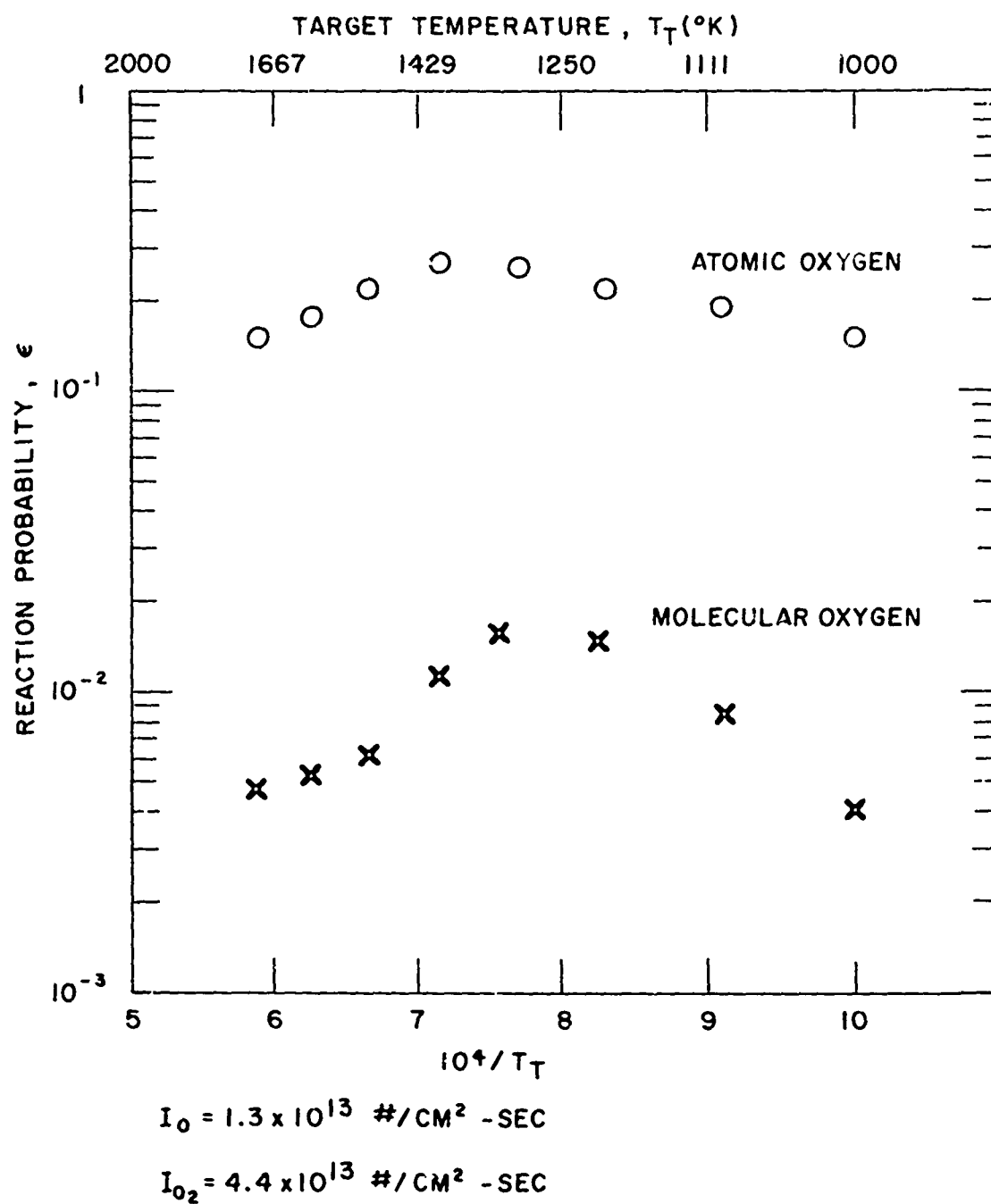


Fig. 32. Reaction Probabilities of O and O₂ Vs. Target Temperature

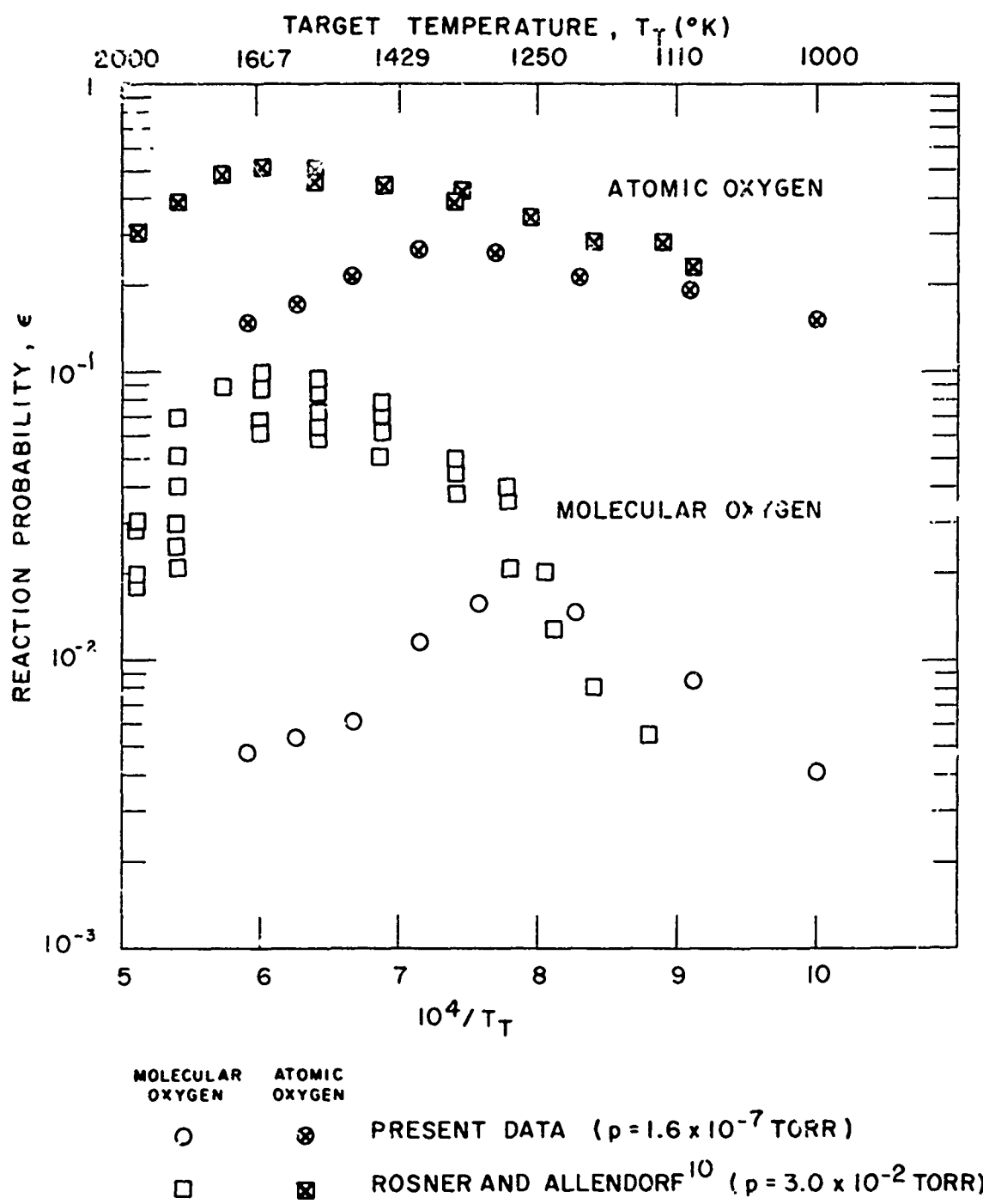
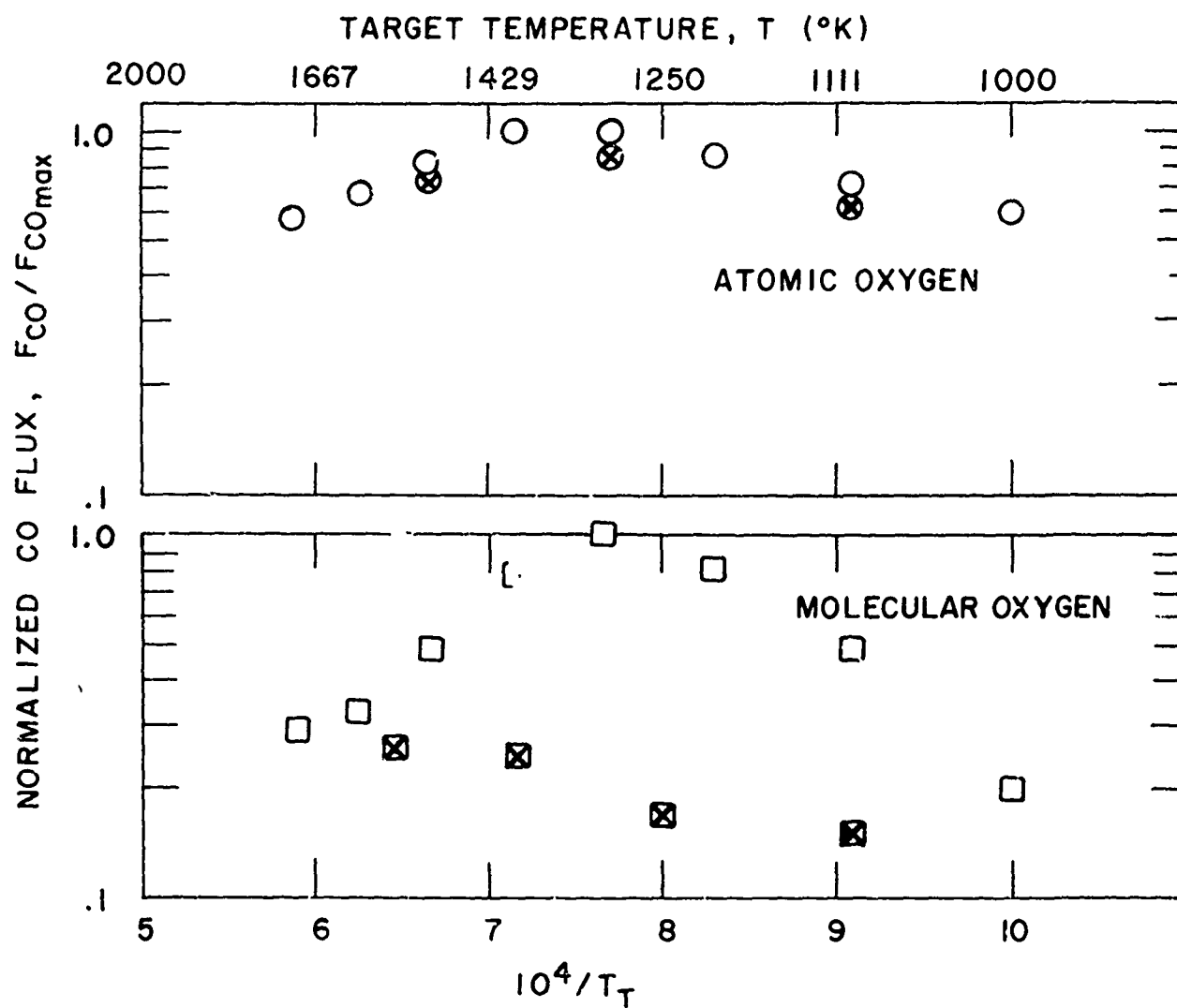


Fig. 33. Reaction Probabilities of O and O₂ Vs. Target Temperature



TEMPERATURE VARIATION SEQUENCE:

○ , □ - 1000°K → 1700°K

⊗ , ⊠ - 1700°K → 1100°K

Fig. 34. Normalized CO Flux for O and O₂ Vs. Target Temperature

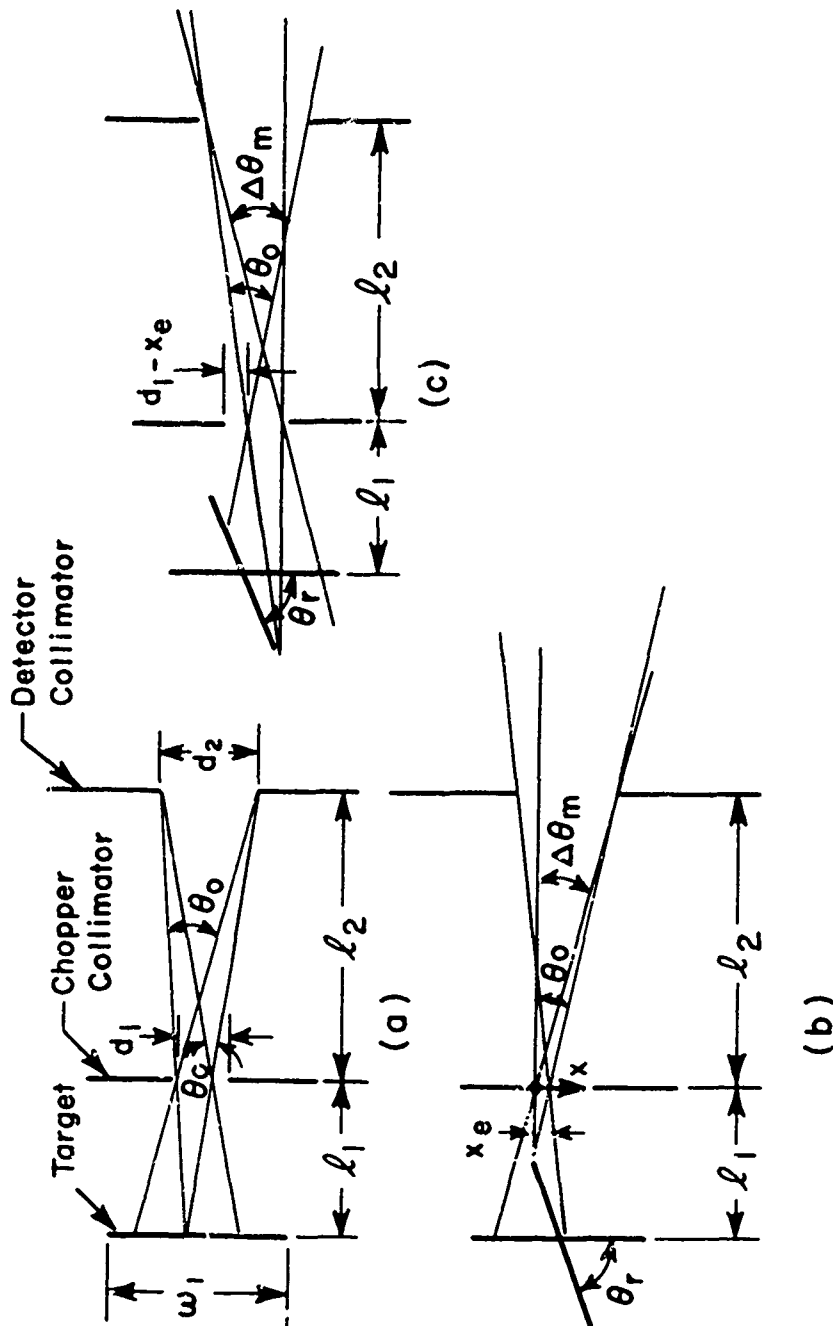


Fig. 35. Schematic Diagram of the Target-Detector Geometry

BIOGRAPHY

George Nung-Keung Liu was born in Shanghai, China and was brought up in Hong Kong, where he attended St. Paul's Co-educational School before coming to the United States in 1963. He received his B.S. degree with Honors in Mechanical Engineering and M.S. degree in Aeronautical Sciences from the University of California, Berkeley in 1967 and 1968 respectively. While at the University of California, Berkeley, he was supported by various scholarships and a Teaching Assistantship. Since coming to M.I.T., he has been holding a Research Assistantship. He is a member of Tau Beta Pi and Sigma Xi.